A NOVEL NONLINEAR MASON MODEL AND NONLINEAR DISTORTION CHARACTERIZATION FOR SURFACE ACOUSTIC WAVE DUPLEXERS

by

LI CHEN
B.S. Nanjing University of Science and Technology, China, 2003
M.S. University of Central Florida, 2006

A dissertation submitted in partial fulfillment of the requirements
for the degree of Doctor of Philosophy
in the Department of Electrical Engineering and Computer Science
in the College of Engineering and Computer Science
at the University of Central Florida
Orlando, Florida

Summer Term
2013

Major Professors: Parveen F. Wahid
Donald C. Malocha

ABSTRACT

Surface acoustic wave (SAW) technology has been in use for well over one century. In the last few decades, due to its low cost and high performance, this technology has been widely adopted in modern wireless communication systems, to build filtering devices at radio frequency (RF). SAW filters and duplexers can be virtually found inside every mobile handset. SAW devices are traditionally recognized as passive devices with high linear signal processing behavior. However, recent deployments of third generation (3G) and fourth generation (4G) mobile networks require the handsets to handle an increasing number of frequency bands with more complex modulation /demodulation schemes and higher data rate for more subscribers. These requirements directly demand more stringent linearity specifications on the front end devices, including the SAW duplexers. In the past, SAW duplexer design was based on empirically obtained design rules to meet the linearity specifications. Lack of predictability and an understanding of the root cause of the nonlinearity have limited the potential applications of SAW duplexers. Therefore, research on the nonlinearity characterization and an accurate modeling of SAW nonlinearity for mobile device applications are very much needed.

The Ph.D. work presented here primarily focuses on developing a general nonlinear model for SAW resonators/duplexers. Their nonlinear characteristics were investigated by measuring the harmonic and intermodulation distortions of resonators. A nonlinear Mason model is developed and the characterization results are integrated into SAW duplexer design flows to help to simulate the nonlinear effects accurately and improve the linearity performance of the products.

In this dissertation, first, a novel nonlinear Mason equivalent circuit model including a third order nonlinear coefficient in the wave propagation is presented. Next, the nonlinear distortions of SAW resonators are analyzed by measuring large-signal harmonic and intermodulation spurious emission on resonators using a wafer probe station. The influence of the setups on the measurement reliability and reproducibility is discussed. Further, the nonlinear Mason model is validated by comparing its simulation results with harmonic and intermodulation measurements on SAW resonators and a WCDMA Band 5 duplexer.

The Mason model developed and presented here is the first and only nonlinear physical model for SAW devices based on the equivalent circuit approach. By using this new model, good simulation measurement agreements are obtained on both harmonic and intermodulation distortions for SAW resonators and duplexers. These outcomes demonstrate the validity of the research on both the characterization and modeling of SAW devices. The result obtained confirms that the assumption of the representation of the 3^{rd} order nonlinearity in the propagation by a single coefficient is valid.

To my son, Lucas, my wife, Qing and my parents

ACKNOWLEDGMENTS

Foremost, I would like to express my sincerest gratitude to my advisor, Dr. Parveen Wahid and co-advisor, Dr. Donald Malocha. I have greatly benefited from Dr. Wahid for her advice, support and friendship for the last ten years, for which I am extremely grateful; I am very honored for the opportunity to work with Dr. Malocha. Discussions with him have been insightful and he provided me many technique suggestions to help me solve the problems. Without the guidance and encouragement from both advisors, I would not have been possible to finish this doctoral thesis. Besides my advisors, I want to thank the rest of my dissertation committee, Dr. Samuel Richie and Dr. Jean Briot for their time and support.

The Ph.D. research is a collaborative project between University of Central Florida and TriQuint Semiconductor. I would like to thank my employer, TriQuint Semiconductor, for providing me the opportunity and supporting this Ph.D. study. Also, I feel grateful to many of my colleagues for their helps on this research: I would like to thank Marc Solal, and Jean Briot for having frequent technical discussions with me and providing tremendous contributions to this research; I would like to thank Robert Aigner, Gernot Fattinger for their constructive comments; I also want to thank Shawn Hester and Paul Shaffer for their help on nonlinearity measurements. My sincere thank also goes to my former colleagues, Pierre Girard and Kamran Cheema, for their supports.

Finally, I owe my deepest gratitude to my family. I would like to thank my wife, Qing, for her endless love and great patience. I would like to thank my parents, Sher Chen and Chengyi

Jiang, for everything they have done for me. Their unwavering support of everything I do has helped make me who I am today.

TABLE OF CONTENTS

LIST OF FIGURES

LIST OF TABLES

LIST OF ACRONYMS/ABBREVIATIONS

1D	One Dimensional
3D	Three Dimensional
3G	Third Generation
3GPP	Third Generation Mobile System
4G	Fourth Generation
ACLR	Adjacent Channel Leakage Ratio
ADS	Advanced Design System
ANT	Antenna
ATT	Attenuator
BAW	Bulk Acoustic Wave
BEM	Boundary Element Model
BPF	Band Pass Filter
BVD	Butterworth-van-Dyke
BW	Band Width
C	Capacitor
COM	Coupling of Modes
CRF	Coupled Resonator Filter

CW	Continuous Wave
DF	Duty Factor
DUT	Device under Test
EVM	Error Vector Magnitude
FBAR	Film Bulk Acoustic Wave Resonator
FDD	Frequency Division Duplex
FDD-LTE	Frequency Division Duplex-Long Term Evolution
FEM	Finite Element Method
fp	Parallel Resonant Frequency
fs	Resonant Frequency
H1	First Harmonic
H2	Second Harmonic
H3	Third Harmonic
HB	Harmonic Balance
HPF	High Pass Filter
IC	Integrated Circuits
IDT	Interdigital Transducer
IMD2	Second Order Intermodulation Distortion

IMD3	Third Order Intermodulation Distortion
IP2	Second Order Interception Point
IP3	Third Order Interception Point
KCL	Kirchhoff's Current Law
L	Inductor
LiNbO3	Lithium Niobate
LiTaO3	Lithium Tantalite
LNA	Low Noise Amplifier
LPF	Low Pass Filter
LTE	Long Term Evolution
PA	Power Amplifier
PCB	Print Circuit Board
PML	Perfectly Matched Layer
R	Resistor
RF	Radio Frequency
RMS	Root Mean Square
Rx	Receive
SAW	Surface Acoustic Wave

SG	Signal Generator
SMA	Sub-Miniature version A
SMR	Solidly Mounted Resonator
Tx	Transmit
UMTS	Universal Mobile Telecommunications System

CHAPTER 1:INTRODUCTION

1.1 Motivation

In radio communications, a duplexer is defined as a device that allows simultaneous bi-directional (full duplex) communication of two signals which share a common antenna. The implementation of duplex function is achieved by combining two band-pass filters, a transmit (Tx) filter and a receive (Rx) filter, together with a matching network at the antenna (Fig. 1-1). Such a signal configuration has been widely adapted in Frequency Division Duplex (FDD) based Third Generation Mobile System (3GPP) applications, such as Universal Mobile Telecommunications System (UMTS) and Frequency Division Duplex-Long Term Evolution (FDD-LTE) system, where duplexers work as key hardware components to simultaneously separate the Tx and Rx signals at different frequencies and suppress the unwanted signals outside operation bands.

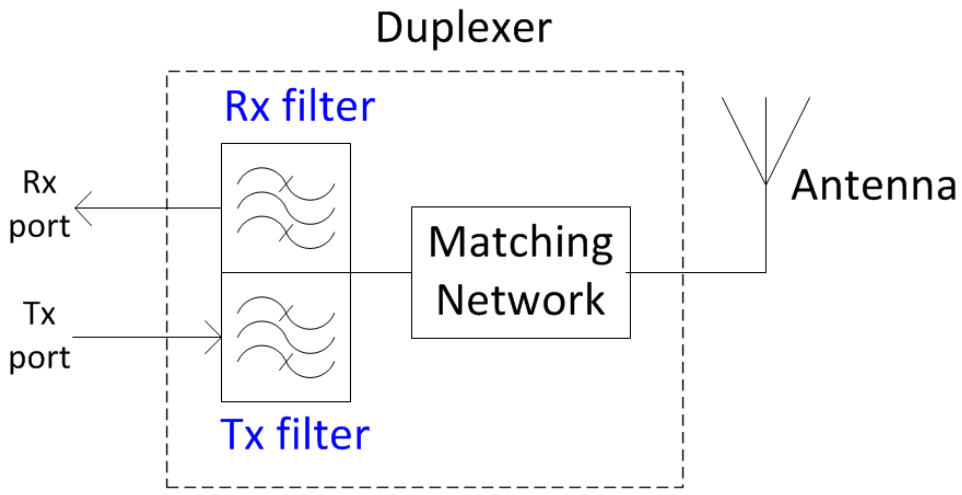

Figure 1-1 Schematic diagram of a duplexer

As one type of RF filtering devices, common design characteristics of duplexers include low pass band insertion loss, high rejection level at stop bands and high signal isolation between Tx and Rx signals. However, over the last decade, the complexity in the RF circuits in the mobile handset has increased dramatically. Integration of multiple band operations has forced the developers to shrink the component sizes and still meet the high linearity requirements. In particular, nonlinearity requirements of FDD systems become extremely important due to the fact that Tx and Rx signals operate simultaneously at separate frequencies and the co-existence of both Tx and Rx signals could cause problems. An example is the Tx leakage into the receiver which can modulate with other signals from the air and generate at the frequency of the receive signal an interferer strong enough to degrade the signal quality at the receiver, causing "jamming" or de-sensitization. Also, due to the nonlinearity of the power amplifiers, spurious emission can be generated outside of the operating frequencies. Therefore, duplexers play the important role of suppressing these off-band spurious signals. Overall, duplexers, as the key components to process the Tx and Rx signals between the antenna and transceiver, are required to be highly linear in order to maintain and improve the overall system signal quality. However, from the perspective of duplexer designs, due to the market trend of size reduction for low cost, it becomes more difficult to design duplexers with small sizes and excellent linear performance. Thus, design challenges of duplexers today include not only providing better small signal performance, but also meeting stringent linearity requirements for large signals to provide enough harmonic suppression and superior intermodulation distortion rejection at the Rx frequency band. To meet these design goals, an accurate nonlinear modeling tool is needed to simulate duplexer nonlinear behaviors and thus better understand nonlinear effects inside duplexers.

1.2 SAW Technology

In this section, the background of SAW technology in presented. For comparison, bulk acoustic wave (BAW) technology is introduced in Section 1.3. Both technologies are widely used for RF duplexer products in mobile applications due to their performance, size and cost advantages over other solutions.

SAW is described as an acoustic wave propagating along the surface of a piezoelectric substrate. Piezoelectric substrates are materials such as quartz, lithium niobate ($LiNbO_3$) and lithium tantalite ($LiTaO_3$). In a SAW device, mechanical energy in the form of surface acoustic wave can be transformed into electric energy. Reciprocally, due to the inverse piezoelectric effect, an electrical signal on the electrodes can excite a surface acoustic wave. Electronic signal processing of SAW on piezoelectric substrates was first suggested by White [1] with the invention of the thin-film interdigital transducer (IDT) structure; since then, it has been commonly used for signal processing, in filters, oscillators and transformers. Fig. 1-2 shows a schematic picture of a simplified SAW IDT. As shown, each period of the IDT consists of multiple metallic strips at the surface of the substrate. These strips are aligned and connected alternatively to the two bus bars. By applying a RF voltage between the bus bars, the electrical field generates a periodic strain on the substrate and excites a SAW propagating along the surface of the substrate. The directions of acoustic wave propagation are also shown on the same figure. On this structure, the resonance condition happens when periodicity of the structure (defined by two fingers with the two spaces) equals an acoustic wave wavelength. Passband transferred functions can be obtained by properly designing the geometry of IDT, such as width of the transducer, stripe length, and metallization ratio of the electrode and adjacent gap.

The SAW resonator has been investigated since the early 1970s, initially with particular regard to the applications for electronic oscillators. In the 1980s, researchers realized that SAW based resonators could be utilized in band pass filters thanks to their high Q and low loss. The typical layout of a 1-pole SAW resonator includes the IDT in the middle and two reflectors (gratings) at each side (Fig. 1-3). A resonator cavity is formed between the two reflectors; in the cavity, the energy is delivered to and extracted from the acoustic resonator by the SAW transducer. By using this type of structure with electrical excitation on the bus bars, an electronic resonator can be achieved with a resonance and anti-resonance frequency response. The resonant frequency (fs) is the frequency at which the impedance of the resonant element goes to zero. The anti-resonant frequency (fp) is the frequency at which the admittance of the resonant element goes to zero. Both fs and fp can be tuned by controlling the period of the fingers and the metal thickness on the substrate. Fig 1-4 shows the admittance response of a fabricated resonator at 800 MHz.

SAW RF filters are normally designed with two types of resonators: the one with a ladder topology with multiple 1-pole resonator elements placed in series and shunt connections; the second being a coupled resonator filter (CRF) with multiple IDTs forming a resonant cavity.

Ladder filters are constructed by cascading a sequence of series and shunt 1-pole resonators. Fig. 1-5 shows the typical topology of a ladder filter. S1, S2 and S3 are series resonators and P1 and P2 are shunt resonators connected to ground. To improve the filter performance such as impedance matching in the pass band and stopband rejection, each resonator is designed with different sizes and frequencies.

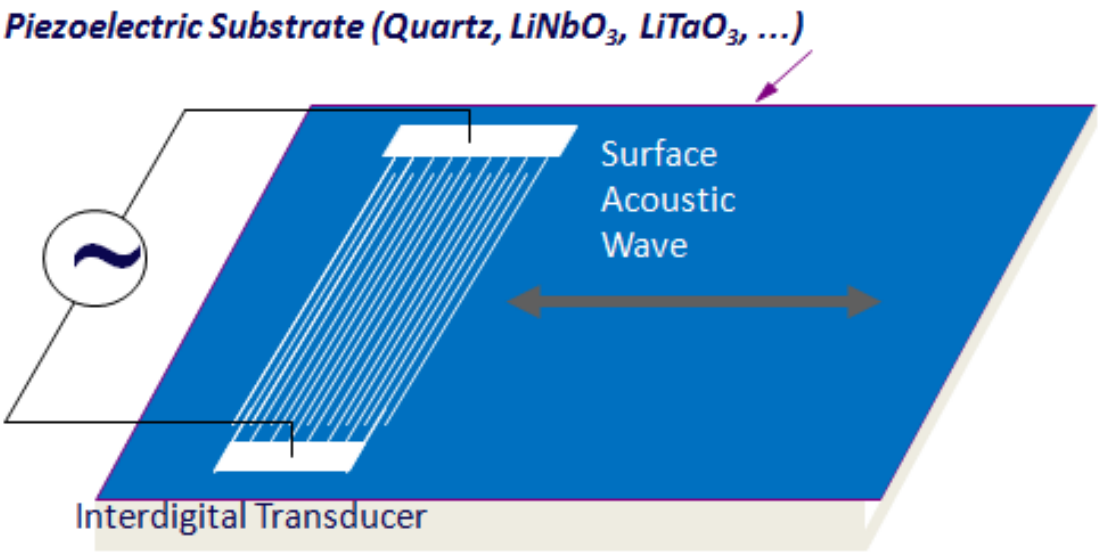

Figure 1-2 Schematic picture of a SAW IDT stucture

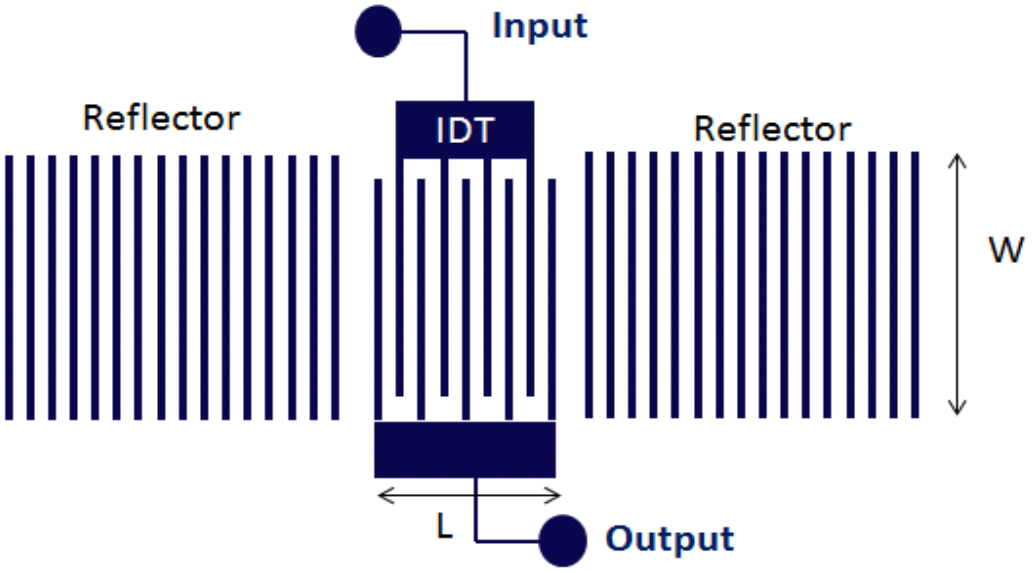

Figure 1-3 Schematic picture of a 1-pole SAW resonator with reflectors at both sides

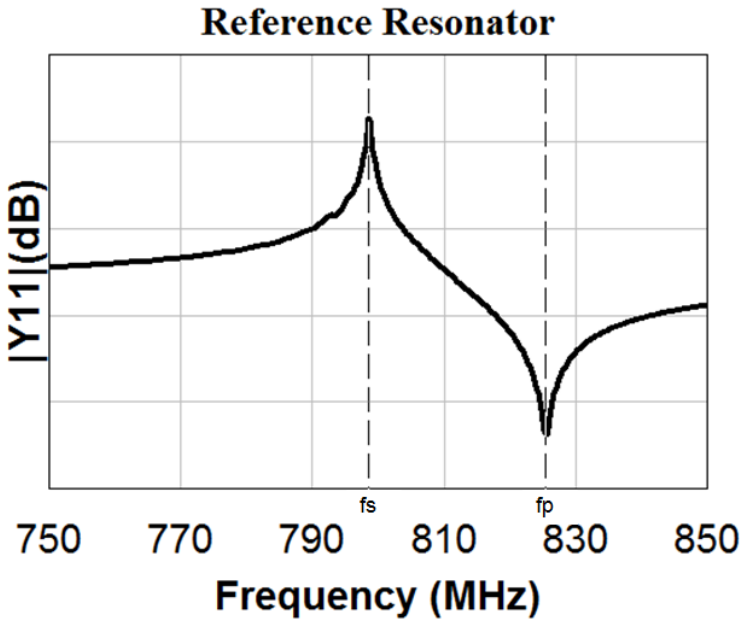

Figure 1-4 Admittance reponse of a resonator at 800MHz

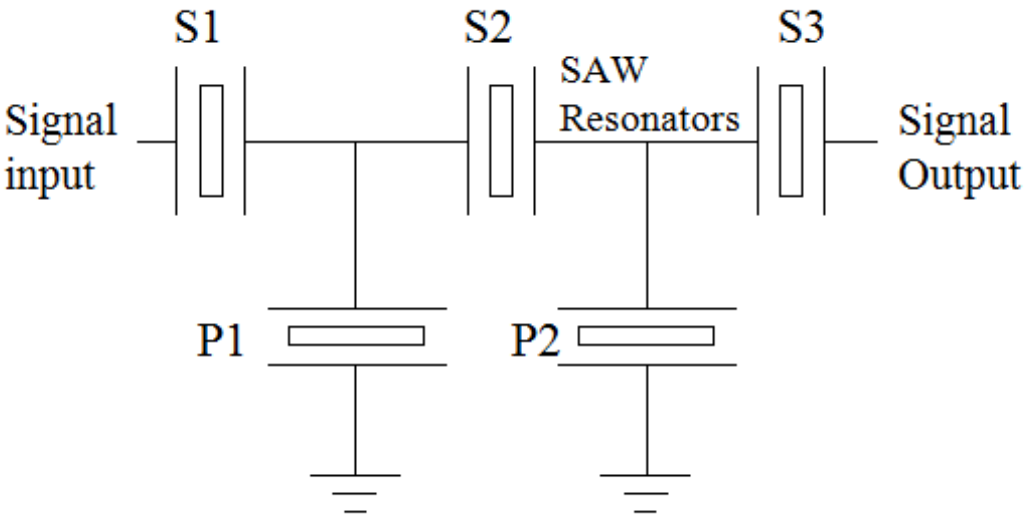

Figure 1-5 A ladder filter with 1-pole resonators placed in series and shunt configurations

Compared to ladder filters which use single-pole resonators, coupled resonator filters are formed using multiple IDTs; these filters are known to provide high stop band rejection, low loss, wide bandwidth, small size and a balun function converting single-ended signals to balanced signals, which is critical to receive filter design. SAW coupled resonator filter theory and design was initially developed in the 1970's and 1990's [2-5].

The principle of a coupled resonator filter are introduced: consider a simple 2-IDT based coupled resonator filter structure with 2 reflectors, input and output IDTs and gaps (spaces), as shown in Fig. 1-6 [6]. Within the cavity, IDT1 and IDT2 are acoustically interconnected and the first and the second order acoustic wave could be coupled efficiently to transmit an electrical signal from input to output. Using more IDTs in the resonator, higher orders of modes can be efficiently coupled. At the both sides of IDTs, the reflectors are used to reflect the acoustic waves around their center frequency

$$f = \frac{v}{2p} \tag{1.1}$$

In the above equation, v is acoustic velocity and p is period of reflector grating. Reflectors effectively trap the acoustic energy within the IDT cavity areas. Meanwhile, gaps between IDTs and reflectors serve to control the phase shift of SAW to improve the coupling between the resonators. Within the coupled resonator filter, fs, fp, bandwidth (BW) and off-band attenuation level are determined by wafer substrate types and geometries of the IDTs, such as period of the reflectors, length, width, metallization ratio and metal thickness. In actual designs, low loss, high piezoelectric coupling substrates are used to achieve wide bandwidth; In addition, a single-ended to balanced signal conversion can be created with an acoustic balun function inside the coupled resonator filter by using the IDTs with different electrical

polarities. Combinations of ladder type and coupled resonator filter are also very commonly used.

A more complicated 3-IDT coupled resonator filter with two input IDTs and one output IDT is shown in Fig. 1-7. The frequency response (S21) of a 3-IDT coupled resonator filter at 800MHz is plotted in Fig. 1-8.

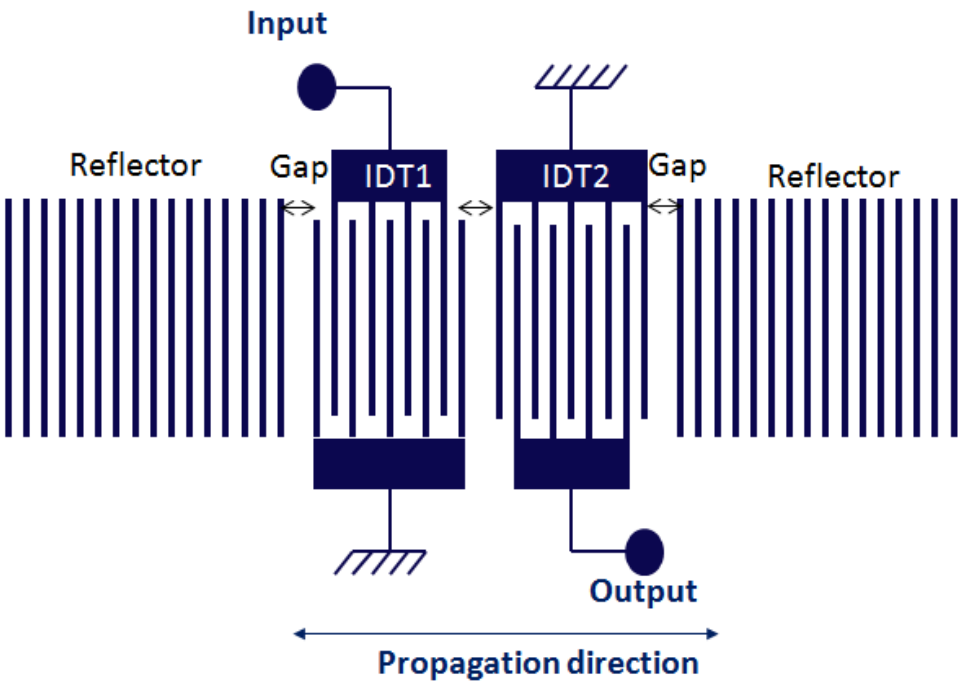

Figure 1-6 A simplified 2-IDT coupled resonator filter stucture with reflectors

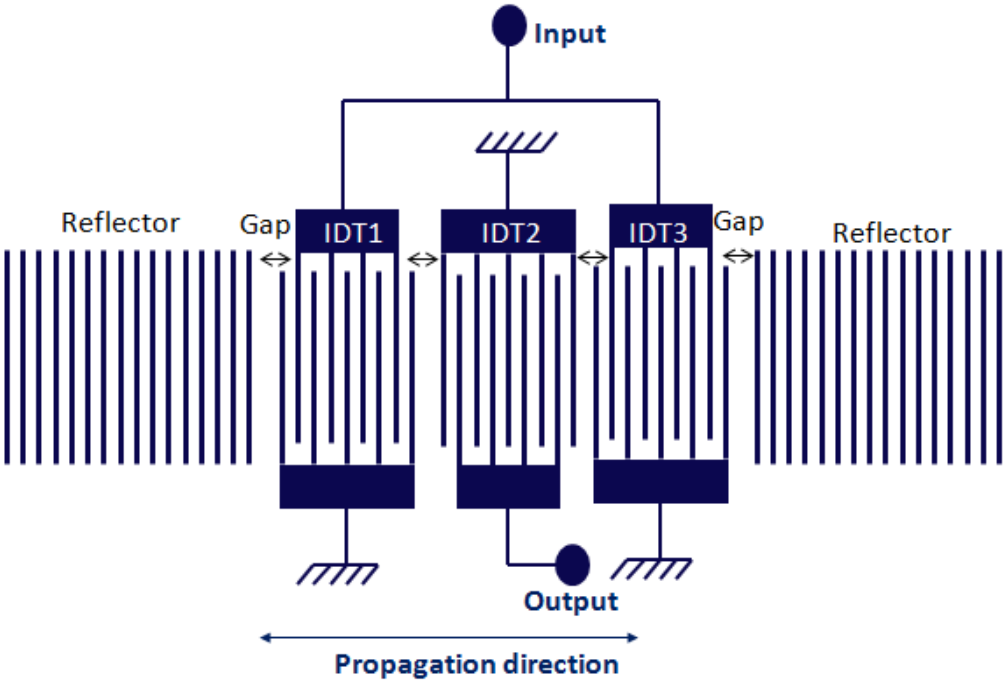

Figure 1-7 A 3-IDT coupled resonator filter stucture with reflectors

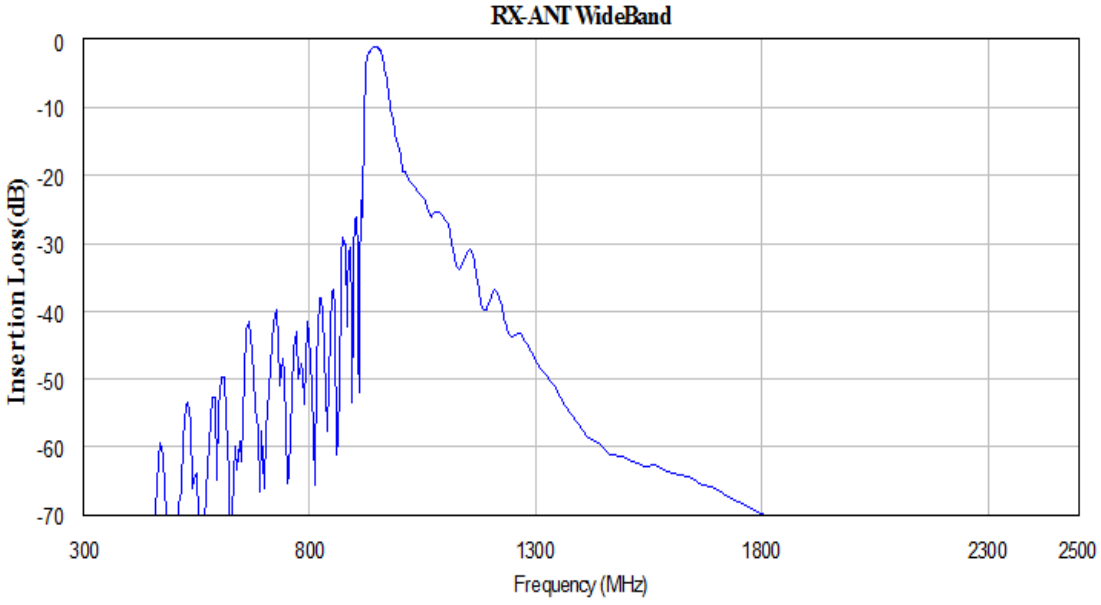

Figure 1-8 Insertion loss response (S21(dB)) of a typical 3IDT coupled resonator filter at 800MHz

1.3 BAW and Comparison to SAW

Compared to SAW, RF bulk acoustic wave (BAW) technology is a relatively new addition to the ultrasonics technology. Instead of having acoustic waves propagating near the surface, BAW is the type of acoustic wave which propagates in the bulk of the substrate. The first commercial BAW filter was first introduced in 2001 [7]. A background of the technology can be found in Prof. Ken-ya Hashimoto's book [8].

In general, differences between SAW and BAW technologies can be summarized based on the following aspects:

1) Substrate material and mechanism: As stated, the two waves can be distinguished by the fact that wave either propagates inside the elastic medium (in the case of BAW) or is localized near the surface of the material (in the case of SAW). Wave properties are determined by the piezoelectric materials used. SAW is normally on mono-crystal piezo-materials such as quartz, $LiNbO_3$, $LiTaO_3$, while BAW devices are usually manufactured on silicon wafers and use thin films of piezoelectric material [9].

2) Process: SAW process involves deposition and patterning of IDTs on the substrate. In order to deposit metal with patterns, either etching or lift-off process can be used. Since typically only one or two patterned metal layers are required to build IDTs, SAW fabrication process is relatively easy. As for BAW devices, there are two different structures available to make the resonators: the first one is called film bulk acoustic wave resonator (FBAR) and the second one is named solidly mounted BAW resonator (SMR). More details of both technologies can be found in [8]. Both technologies require multiple metal mask layers to form the filter function thus process complexity and cost are much higher than SAW processing. Also, due to process limitation and lack of piezoelectric coupling, BAW CRF is

extremely difficult to be designed and fabricated thus only single-pole resonator/ladder type BAW filters are available for commercial products, as of today.

3) Wireless applications: SAW technology approaches are known to be limited for any application beyond 2.5 GHz due to the requirements for line width and gap dimensions of the IDTs. Devices at frequency of 2.5 GHz and above call for electrode widths smaller than 0.3um lithography limit of an i-line stepper. Also, for high frequencies, the filter insertion loss is limited by resistivity of the electrodes. BAW technology instead is capable of addressing application up to 6 GHz without reaching manufacturing limits. However, SAW products are dominant for applications around 1 GHz due to their size and cost advantages over BAW counterparts. The distribution of filter technology application versus frequency and performance are summarized by Aigner [9].

4) Nonlinearity: Even though both SAW and BAW filters are passive devices, they both show inherent nonlinear behaviors, especially under high electrical field excitation. However, due to the different wave types, excitation, propagation and geometry on the piezoelectric substrates, nonlinear phenomena of SAW devices behave differently to its counterpart of BAW [10]. Due to the presence of two electrodes per acoustic wavelength, SAW resonators offer inherently better 2^{nd} order nonlinearity than BAW devices. However, they are worst in term of 3^{rd} order nonlinearity. Therefore, for this SAW nonlinearity researches, 3^{rd} order nonlinearity gets more attention due to its distortion severity at the system level

5) Single-ended to balanced conversion: As stated, one of the strength SAW has is that coupled resonator filter can include a balun function inside the IDTs to generate balanced signal at output. Due to the complexity of BAW process, coupled resonator topology is difficult to be fabricated.

1.4 Nonlinearity Specifications inside a RF Front-end System

Before further investigation of the nonlinear properties of SAW devices, it is important to depict the nonlinearity environment inside a mobile handset in a 3GPP based system. Fig. 1-9 shows a simplified RF front end system of a handset with types of distortions indicated. In FDD mode, the Tx and Rx signals continuously work at the same time and are present in two different frequency bands. In the Tx signal chain, the output signal from the transceiver is amplified by a power amplifier, and then is filtered by duplexer's Tx filter. The filtered signal is connected to the antenna (ANT) through the switch and then propagates into the air. In the meantime, an incoming signal from the air is received by the ANT at the Rx frequency band; this Rx signal is filtered by the Rx filter and then amplified by the LNA; finally, the Rx signal is demodulated by the transceiver. The linearity requirements are defined in order for the receiver to meet the performance requirements for all operation modes. Due to the limited Tx to Rx isolation of the duplexers, the Tx signal leaks into the receiver and it is possibly the strongest interference for the receiver in the handset; the deterioration is the worst when the power amplifier operates at high power model.

Linearity requirements and nonlinear distortion impacts on the mobile system have been discussed in [11],[12],[13] and [14]. In summary, major nonlinear distortions in the front end can be categorized by their impact:

1) Signal quality degradation: Signal quality is characterized mainly by the specification of the Error Vector Magnitude (EVM), which is a measure of how far the constellation points of the real signal are off from their ideal locations. (An ideal location is referred to the location of constellation point by a signal sent by an ideal transmitter or received by an ideal receiver). Normally, this is the problem for Tx signal mainly since the operation power in Tx chain is

much higher. PA and duplexers are the main causes for EVM degradation. Also, EVM requirements vary by the complexity level of different modulations. Communication standards define EVM specification to make sure the transmit signal to the base station could be demodulated.

2) New spectrum generation: Usually, the term new spectrum generation refers to the spurious signals produced at any RF frequencies other than the operation frequency due to nonlinearity of the devices. Spurious emissions can be detected on the frequency spectrum. Harmonics, second order intermodulation distortion (IMD2), third order intermodulation distortion (IMD3) and adjacent channel leakage ratio (ACLR) are among the most common specifications used to evaluate the severity of spectrum growth. When the main signal is excited at the fundamental frequency f_0, harmonics are defined as the spurious powers at frequencies which are integer multiples of the fundamental frequency. Intermodulation occurs when a mix of two of more signals with different frequencies creates unwanted spurious emissions at the frequencies not deliberately created. In the mobile front end systems, intermodulation products could be harmful if they drop into the Rx frequency. ACLR is used to define the ratio between the total power of adjacent channel to the main Tx channel's power and is used to judge the interfere level relative to other operating signal channels.

3) Desensitization: Desensitization is defined as the degradation of receiver sensitivity due to the presence of the Tx signal. The cause of Rx desensitization could be: a) Rx band noise generated by the power amplifier; b) Tx leakage into receiver due to limited Tx to Rx isolation, producing DC and RF frequency components which fall into the receive band of the direct conversion receiver; c) IMD2 and IMD3 products inside duplexers in which fall in the

Rx band degrading the signal noise ratio of the receiver. These IMD products are due to the intermodulation between the Tx signal and external jammers.

Overall, duplexers play a very important role in the harmonics and intermodulation performances of the front end system. Therefore, this research will focus on harmonic and intermodulation measurements and models of the SAW filters for mobile communication systems.

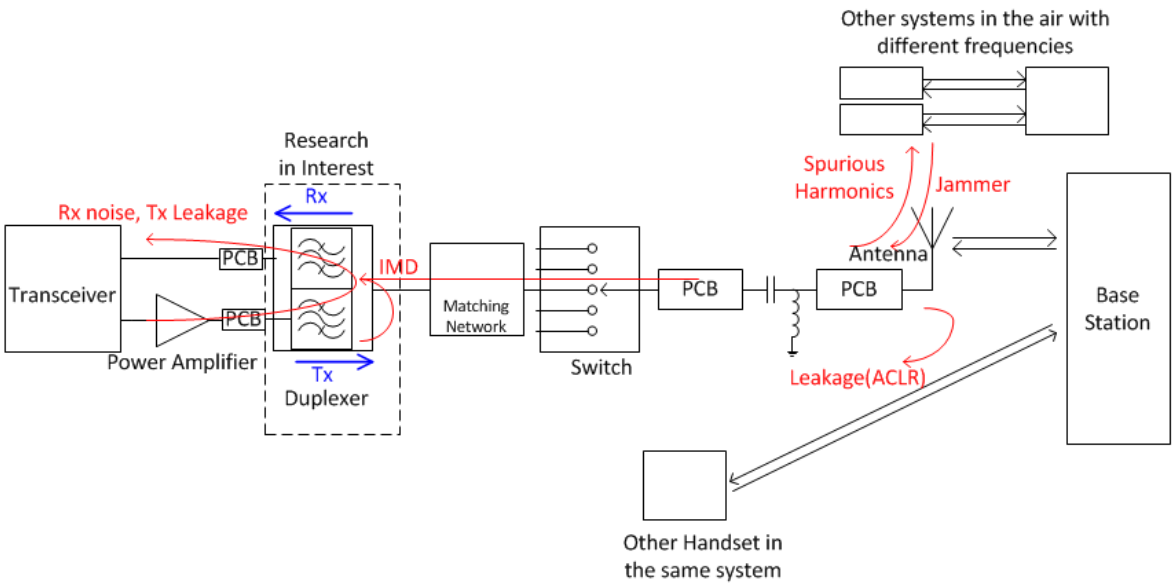

Figure 1-9 Schematic diagram of a smplified RF front end system of a mobile handset with distortion

1.5 Organization of the Thesis

This dissertation contains six chapters: Chapter 1 introduces the background of SAW devices and common nonlinearity distortions inside the RF front end of a mobile device. Chapter 2 gives a literature review of the available linear and nonlinear modeling technologies for SAW devices. The uniqueness and advantage of the nonlinear Mason model are discussed. Chapter 3 explains the nonlinear Mason model theory. Starting from a review of the piezoelectric wave equations and an examination of the original linear Mason model, a novel nonlinear Mason model is derived. Chapter 4 discusses the nonlinear effects of the SAW devices, including SAW resonators and duplexers. Large signal harmonic and intermodulation measurement setups are discussed and results of both resonators and duplexers are shown. The characterization of SAW nonlinear behavior is done by comparing the harmonics results of different resonators. Chapter 5 presents the validation of the nonlinear Mason model by simulating the harmonic and IMD spurious responses of the SAW resonators and duplexers in Advanced Design System (ADS). Simulation flow and setup are documented and the simulation results are compared with measurements. Future work using this nonlinear Mason model is discussed. Chapter 6 presents the conclusion of the research.

In this dissertation, the characterization and modeling effort has been focused on UMTS Band 5 at 800MHz frequency range. All the test resonators and duplexers have been fabricated on $LiTaO_3$ YXl42 °(LT42) and $LiTaO_3$ YXl48 °(LT48) wafers.

CHAPTER 2: SAW DEVICE MODELING

2.1 Introduction of SAW Device Modeling Technologies

Although surface acoustic waves have been known for more than a century, the SAW based technology did not gain much attention until mass-production of SAW devices became possible by using photolithography technology. SAW devices can now be fabricated with high accuracy and are important components in many communication systems. The proper design of SAW devices with accurate predictability is required to ensure design success. In order to accurately predict the electrical performance of SAW devices, several SAW modeling technologies were proposed in the last 40 years. Modeling efforts before 21st century were mainly focused on building linear models to simulate SAW IDT structures for transducers, resonators and filters. Most of the existing modeling technologies have been discussed in the several books including the books by Campbell [15], Hashimoto [16] and Royer [17]. In the recent years, due to high linearity requirements in 3GPP, more and more attention has been paid to finding solutions to model the nonlinear behavior of both surface and bulk acoustic wave devices.

In this chapter, an overview of some of the most common modeling methods done by previous researches is presented. Section 2.1 introduces first-order linear models for SAW and Section 2.2 discusses higher-order nonlinear models for both SAW and BAW. Section 2.3 describes the uniqueness and advantage of the nonlinear Mason model developed in this Ph.D. study.

2.1.1 Delta-Function Model for SAW Transducers

The delta-function model for SAW transducers was first proposed by Tancrell et al [18] in 1971 and it is the simplest one dimensional (1D) model to simulate the transfer frequency response between the input and output transducers. It is based on the assumption that the IDT can be regarded as a superposition of periodic wave sources. The method simulates a relative transfer insertion loss as a function of frequency when input and output voltages are applied respectively at the input and output IDTs. It assumes that opposite voltage polarity is applied at each adjacent electrode pair and opposite electrical charges are accumulated at the edges of the electrodes, as shown in Fig. 2-1. The resultant charge distribution can then be modeled as delta function sources of electric field intensity. The superposition of these delta function sources can be used to simulate the overall electric field intensity and yield the frequency response of $H(f)$:

$$H(f) = \frac{V_o(f)}{V_i(f)} = \sum_{m=1}^{M} \sum_{n=1}^{N} I_n I_m \exp[i(x_n - y_m)\frac{2\pi f}{v}] \qquad (2.1)$$

where M is the total number of fingers in output transducer; N is the total number of fingers in input transducer. $V_o(f)$ is the output voltage and $V_i(f)$ is the input voltage. $H(f)$ is the transfer function. I_n and I_m are the coefficients which have magnitude and phase proportional to electric field intensity. f is the frequency and v is the surface wave velocity.

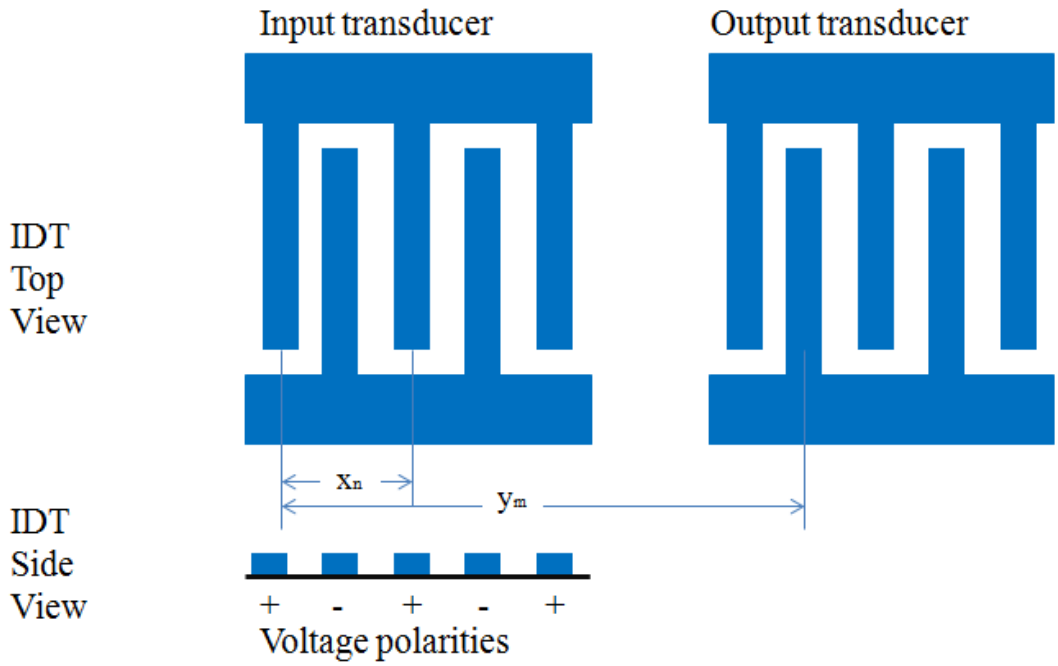

Figure 2-1 Input and output IDTs with delta function sources demonstrated

2.1.2 Equivalent Circuit Model for SAW Resonators

Although the Delta-Function model is capable of predicting the frequency response of an IDT, it does not include the effects of internal reflection within the IDT [16]. Therefore, in the cases of simulating SAW resonators where internal reflection is essential to predict the high Q and low loss, the Delta-Function model is not capable of offering accurate results. Alternatively, equivalent circuit models have been widely used to simulate impedance and operation of SAW resonators effectively by using lumped inductor (L), capacitor (C) and resistor (R) circuits.

Overall, there are two main equivalent circuit models used for simulations: the first one is a behavior equivalent circuit model and is called Butterworth-van-Dyke (BVD) model (Fig. 2-

2). Inside the regular BVD model, R_a is the series resistor to represent the loss; L_a is the motional inductance and C_a is the motional capacitance. The lower branch is called static branch, in which $C_0$is the static capacitance of the IDT .The BVD model can accurately represent the resonator impedance around fs and fp, the Q factor and the static capacitance of resonators. The regular BVD model can be also extended to include other losses and spurious resonances[19]. The value of the lumped elements in the BVD model is dependent on the geometry parameters of the transducers and the substrate parameters and can be calculated; however, the model itself is not capable of analyzing the surface acoustic wave generation and propagation. Overall, the BVD lumped element equivalent circuit model gives an accurate representation of the resonator frequency behavior and the model can be implemented directly in circuit analysis programs. The BVD model is also mostly used for one port resonators.

The other popular model is a physical model and it is called Mason equivalent circuit model. The SAW Mason model was first demonstrated in [20, 21] stating that an electrode section of IDT (Fig. 2-3) could be represented by an equivalent electromechanical circuit with lumped elements. The lumped elements in the Mason model could also be replaced by the transmission lines [22]. The transmission line version of the Mason model is called the Redwood version of the Mason model. Fig. 2-4 shows the Redwood version of the linear Mason circuit to represent one electrode section of an IDT. In the circuit, the Mason circuit has three ports. Ports 1 and 2 are the acoustic ports, (F_1, v_1) and (F_2, v_2) are the mechanical forces and velocities at the left and right edges. Port 3 is the electrical port with an excitation voltage U_3 and current i_3. Additionally, the turns ratio of the transformer ϕ represents the piezoelectric coupling; C_0 is the static capacitance. The 3-port network contains the electrical-mechanical relationship of the IDT. A full transducer/resonator simulation can be done by

cascading N (number of electrodes) unit Mason circuits (of one electrode section) at their ports 1 and ports 2 and connecting their electrical ports 3 in parallel. Adjacent electrodes are assigned with opposite electrical polarities (Fig. 2-5). The Mason model is a general model operating with a parameter set which only depends on the substrate crystal type but not on the specific geometry of the transducers. At the difference of the BVD model which is an equivalent circuit of the resonator, the Mason model represents the acoustic propagation and the transduction for all the electrodes of a device. It is more general and it can be used to simulate devices more complex than a one port resonator. A detailed review of the Mason model is presented in the Chapter 3.

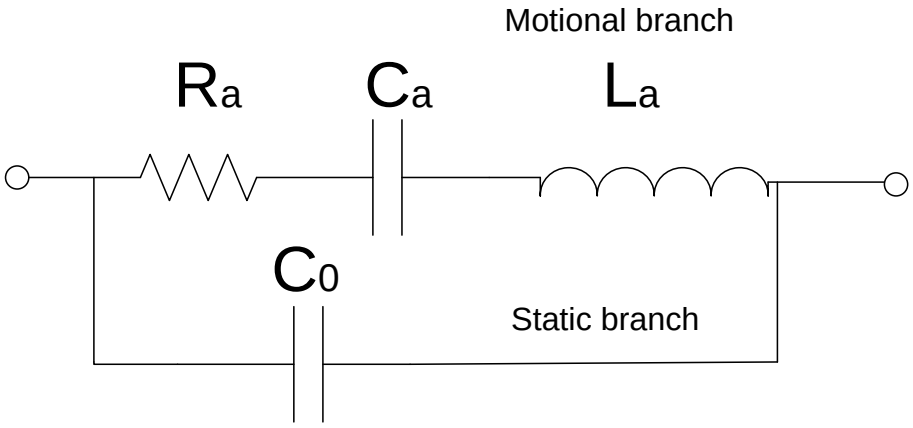

Figure 2-2 Schematic of the 2-port Butterworth-van-Dyke (BVD) equivalent circuit model

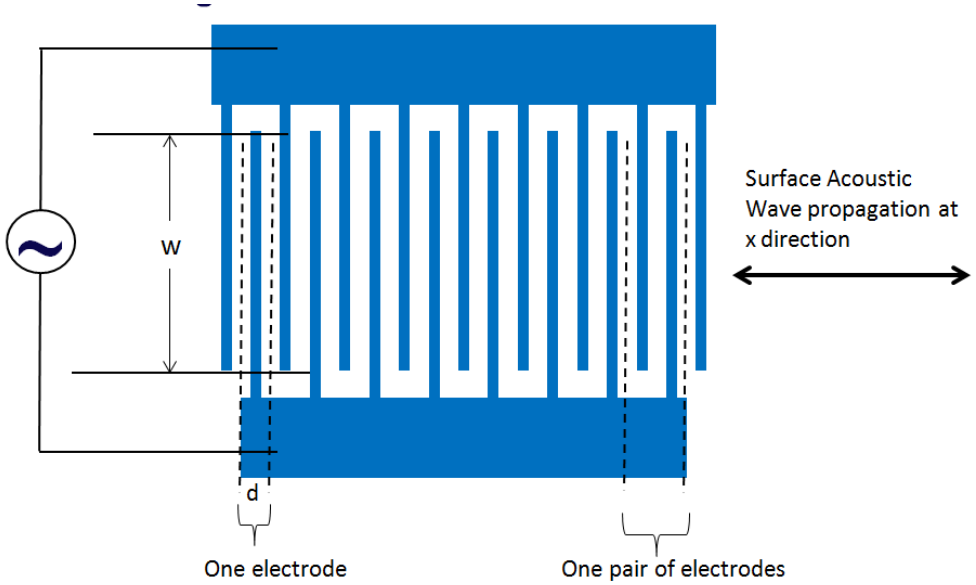

Figure 2-3 Layout of a SAW interdigital transducer

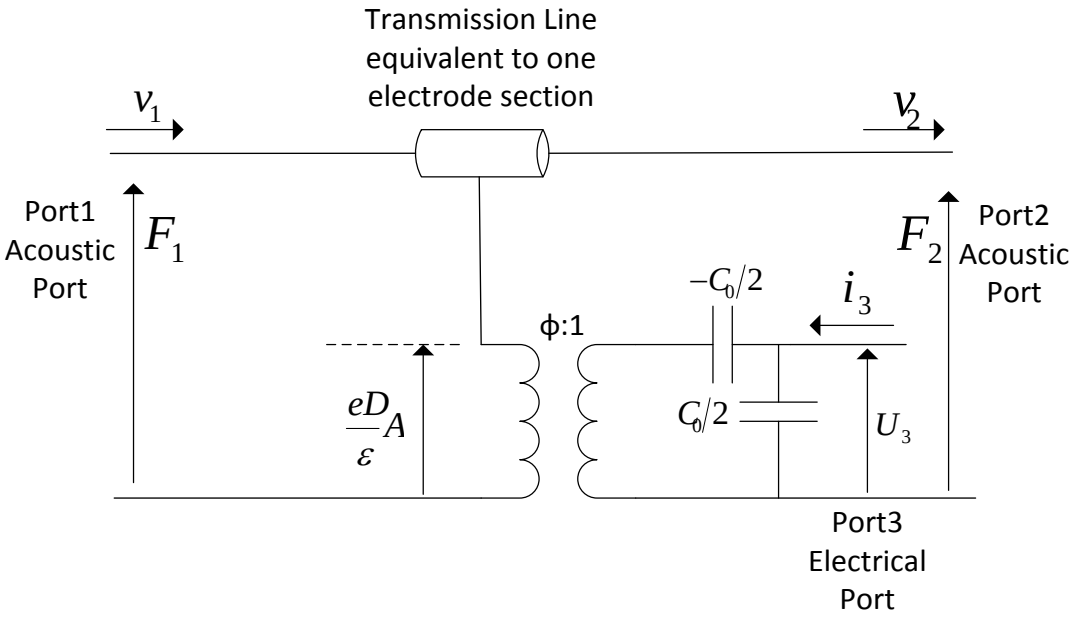

Figure 2-4 The Redwood version of the linear Mason model for one electrode section of a SAW transducer

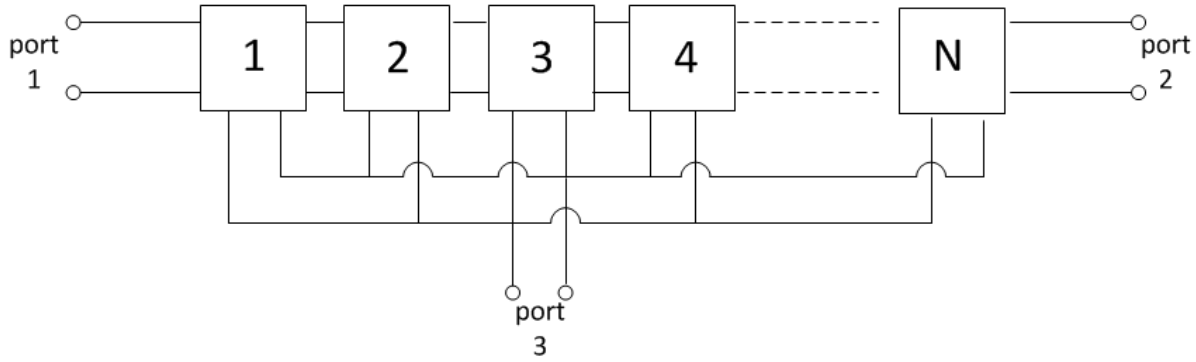

Figure 2-5 Equivalent circuit of a whole transducer, made up of N sections of Mason unit circuits

2.1.3 Other Models

Besides the equivalent circuit approach, a few other models have been developed to precisely characterize the SAW resonator propagation characteristics taking into consideration the transduction and diffraction mechanism. By using these physical models, each section of the resonator (grating and transducers) is individually analyzed and then combined using network analysis to obtain the overall resonator's frequency response. The review in this section includes three of the most popular techniques to simulate the SAW filters: they are the p-matrix method, the coupling-of-modes (COM) method and the finite-element method/Boundary Element Model (FEM/BEM).

The term "p-matrix" was introduced by Tobolka [23] as a description of a mixed matrix presentation of a SAW transducer. In 2001, Ventura, Hode, Desbois and Solal published a

comprehensive method to describe the pseudo-SAW response of an individual electrode [24], a side view of which is shown in Fig. 2-6. In the plot, u and i are the electrical voltage and current excited on the electrode; a_1 and b_1 are the incident and reflected waves at the left side of the elementary cell and a_2 and b_2 are the incident and reflected waves at the right side of the cell. Overall, a 3-by-3 p-matrix of an elementary cell can be presented as:

$$\begin{pmatrix} b_1 \\ b_2 \\ I \end{pmatrix} = \begin{pmatrix} p_{11} & p_{12} & p_{13} \\ p_{12} & p_{22} & p_{23} \\ -4p_{13} & -4p_{23} & p_{33} \end{pmatrix} \begin{pmatrix} a_1 \\ a_2 \\ V \end{pmatrix} \tag{2.2}$$

in which $p_{11}$and $p_{22}$are the acoustic reflection coefficients; p_{12}corresponds to the acoustic transmission coefficient; p_{13} and p_{23} are called excitation efficiency, which are related to piezoelectricity; p_{33} is the admittance of the unit. As indicated, the amplitudes of the incident and reflected waves at the acoustic ports and the voltage and current at the electrical port are chosen as variables.

The whole SAW IDT section is then simulated by cascading multiple individual elementary cells by their ports 1 (a_1, b_1) and ports 2 (a_2, b_2). Then the SAW resonator's electrical admittance is obtained by cascading the scattering parameters of the gratings on each end of the transducer (Fig. 2-7). The p-matrix can be solved by using numerical methods such as perturbation method. A detailed introduction of the p-matrix theory is covered in Chapter 12 in [25]. A similar approach called 'Reflective Array Model' was published by Morgan [26].

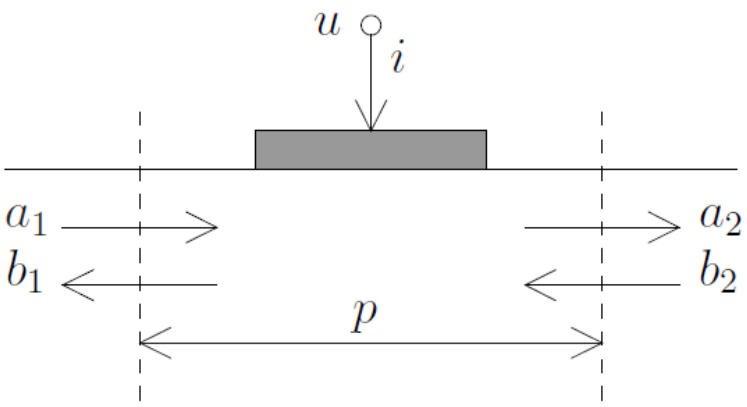

Figure 2-6 An elementary cell of p-matrix model

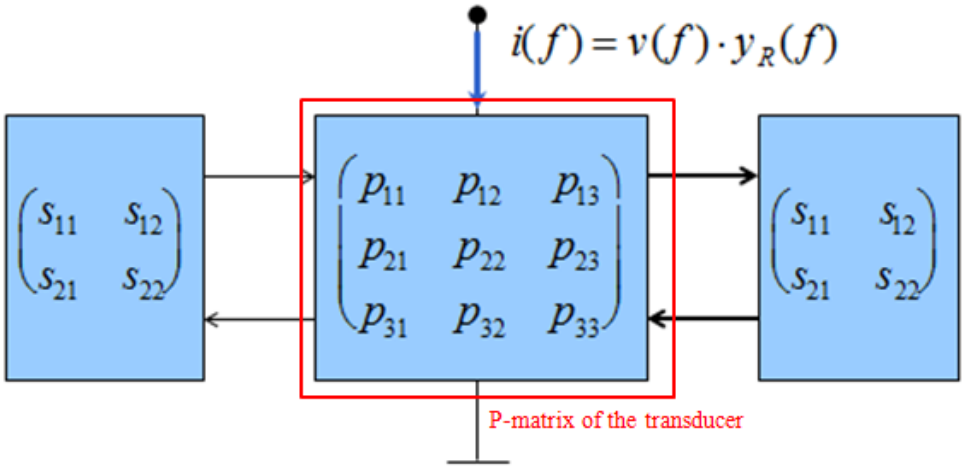

Figure 2-7 P-Matrix block diagram of a SAW resonator

The second model for the SAW resonator is the coupling-of-modes (COM) method. Unlike the p-matrix model, the COM model treats the IDT's currents and voltages as continuously varying functions of position. This method was first developed by Pierce [27] in 1954 and was then introduced to SAW simulation in 1970s by Suzuki et al. [28] and Haus [29]. In the COM model, the unit section shown in Fig. 2-5 is regarded as two waves $a(x)$ and $b(x)$

propagating in forward and backward direction along x axis, respectively. These two waves can be characterized by two simultaneous linear equations:

$$\begin{cases} a(x) = R(x)\exp(-j\dfrac{k_g}{2}x) \\ b(x) = S(x)\exp(+j\dfrac{k_g}{2}x) \end{cases} \tag{2.3}$$

where R and S are the wave amplitudes; $k_g = 2\pi/p$ is the wave number and p is the period of acoustic wave.

The equations describing the acoustic behavior of an array of electrodes with a harmonic voltage applied to the array were published in [30] and [31]. Using the COM equations, the matrix of a uniform IDT can be written as:

$$\begin{pmatrix} \dfrac{dR}{dx} \\ \dfrac{dS}{dx} \\ \dfrac{dI}{dx} \end{pmatrix} = \begin{pmatrix} -j\delta & j\kappa & j\varsigma \\ -j\kappa^* & j\delta & -j2\varsigma \\ -j2\varsigma^* & j2\varsigma & j\omega C_s \end{pmatrix} \begin{pmatrix} R \\ S \\ U \end{pmatrix} \tag{2.4}$$

where δ is the detuning parameter, κ is the coupling parameter of reflection, $\varsigma$is the excitation coefficient and C_s is the static capacitance. The full transducer simulation can be integrated mathematically from the above matrix. The determination of the COM parameters can be done using the perturbation method. A detailed introduction to the COM theory can be found at Chapter 7 in [16]. While the COM method has a significant conceptual difference compared to the p-matrix model, the two approaches produce very similar results.

The third method to model SAW devices is the finite-element method/Boundary Element Model (FEM/BEM) [32, 33], and is a numerical approach. The principle idea is to define a

planar substrate surface and to model one side of this surface using Green's functions and a finite element approach for the other side of the surface. There are several advantages to use the FEM and BEM combined approach to analyze SAW transducers; first and foremost, FEM is an analysis tool that can account for wave polarization and handle three dimensional (3D) simulation of transverse effects like radiation in bus bars; Secondly, by using BEM to model semi-infinite substrates, the analysis can be carried out directly without the need to define boundary conditions or use Perfectly Matched Layer (PML) which are required when using FEM. Additionally, by combining FEM and BEM, the region of mesh is smaller, less nodes and degrees of freedom are required.

To demonstrate this, a 3D FEM meshed SAW transducer [33] is shown in Fig. 2-8 with two periods. Two electrodes (dark gray and clear) and the bus bars are meshed and they are forced to opposite electrode potentials. BEM is used at $x_2 > 0$ to model the semi-infinite substrate under the meshed electrodes. FEM is used for the electrodes at $x_2 < 0$ to model the IDT structure. Periodic boundary conditions are applied for the propagation and transverse directions x_1 and x_3. A semi-infinite substrate or a layered substrate, below the transducer, is analyzed using its Green's function. The presentation of the model and its solution are explained in [33].

Compared to the p-matrix and the COM theory, the FEM/BEM model takes into account more of the physical effects of SAW devices through 2D or 3D simulation. However, the FEM based modeling technique is more difficult and the computation time is much longer. Also, a difficulty of the FEM/BEM approach is the need to know accurately the geometry of the device and the material parameters.

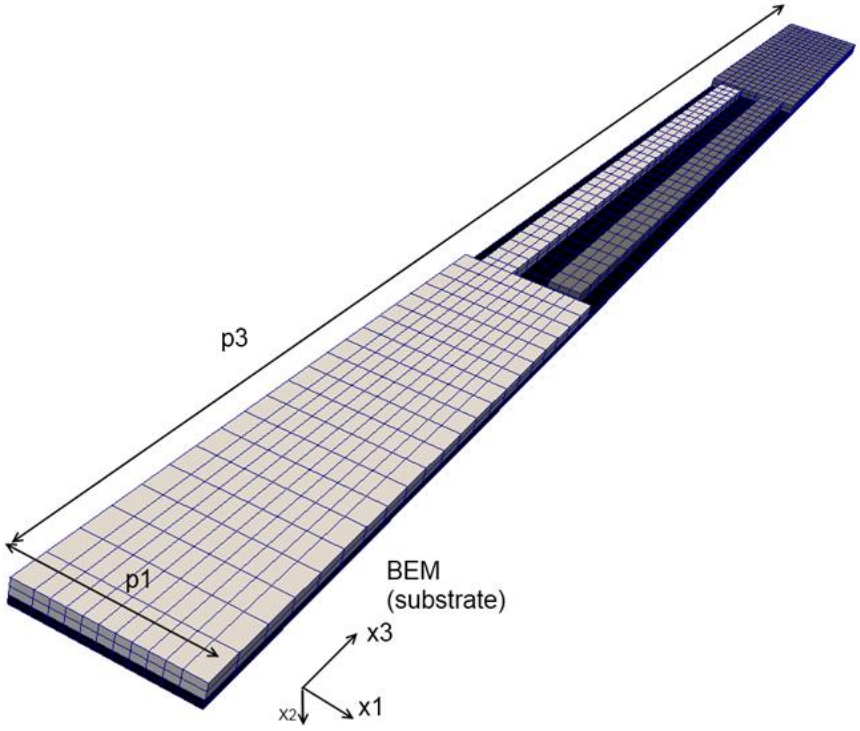

Figure 2-8 Example of a FEM meshed SAW transducer (two periods); BEM is used to model a semi-infinite substrate placed under meshed electrodes (x_2>0); FEM is used to model the electrodes of the IDT (x_2<0)

2.2 Nonlinear Modeling Technologies

2.2.1 Introduction

Passive SAW devices are often recognized as linear devices. Therefore, their designs usually rely on linear models such as p-matrix or COM model. However, due to the nonlinearity requirements by 3GPP, the SAW duplexer design approach is forced to be changed to include nonlinearity simulations.

Nonlinear effects in SAW devices were studied in the 1970s and 1980s. The research topics were mainly on generation of harmonics during the SAW propagation or the mixing of counter propagation waves for convolver applications [34, 35]. In recent years, a few nonlinear models were developed to predict the nonlinear effects of BAW and SAW duplexers. Among them, most studies used equivalent circuit model methods and demonstrated sufficient accuracy to model the nonlinearity of BAW duplexers. For example, Feld [36], Shim [37] demonstrated the nonlinear Mason model for FBAR devices. Collado et al. [38] developed a nonlinear Krimtholz, Leedom and Matthaei (KLM) model and Ueda et al. [10] proposed a circuit model based on strain and electric field dependence. Besides these, Aigner et al. [39], Nitescu et al. [40] and Rocas et al. [41] have published several papers on extending the BVD model to include nonlinear terms to simulate BAW resonators. Due to the complexity of SAW structures and their longer propagation distance, SAW nonlinearity modeling is inherently more difficult and there is considerably less published literature on this topic.

In terms of the origin of nonlinear effect, it is widely agreed upon that the dominant nonlinearities in BAW and SAW resonators stem from nonlinear behavior in the resonator's piezoelectric material. However, the nonlinear constants of piezoelectric materials are very difficult to measure. No measurement of the constant for lithium tantalate was found in the literature. For BAW, thin films are used so it is even more difficult to make the measurement. The researchers cannot rely on the physical constants of the material to estimate the dominant nonlinear mechanisms. They need to use assumption based on the measurement of actual devices. Due to the differences in wave types, excitation, propagation and geometry on the piezoelectric substrates, nonlinear phenomena in SAW devices are very different from BAW devices. For example, it is empirically known that SAW resonators offer better 2^{nd} order

nonlinearity but worse 3rd order nonlinearity than BAW resonators. Thus, the origin of the dominant nonlinear effects in SAW and BAW devices is expected to be from different material parameters. So, even through SAW and BAW devices might share similar forms of linear equivalent circuit models, approaches to develop the SAW nonlinearity models are quite independent.

Regarding the available models to simulate nonlinearities in SAW devices, a few approaches have been developed along with the nonlinear Mason model. Among them, the nonlinear BVD mode [42] is a relatively simple approach consisting of a nonlinear component in the standard BVD representation of the resonator. The nonlinear p-matrix model [43] extends 3rd order elasticity to the p-matrix presentation of the transducers. Also, S. Inoue et al [44] showed a nonlinear elastic model to simulate the triple beat product in a SAW duplexer by considering a nonlinear wave proportional to the product of the wave amplitudes for the three tones and the corresponding current source. The approach is close to the nonlinear p-matrix model but the reflection of the nonlinearly generated wave is not taken account. Overall, all these models are able to simulate the nonlinear spurious responses of the SAW resonators/duplexers with reasonable accuracy. The following sections overview both the nonlinear BVD model and nonlinear p-matrix model.

2.2.2 Nonlinear BVD Model

The nonlinear BVD model was developed by the author of this thesis in 2010 to simulate 3rd order nonlinear effects of SAW resonators and duplexers. Starting from the linear BVD model (as shown in Fig 2-2), the nonlinear simulation of a SAW resonator is done by

assuming a quadratic dependence of the motional inductance (L_a) on the root mean square (RMS) value of the current I. Thus, the current dependant L_a is given by:

$$L_a(I) = L_a \times (1 + L_{a3} \cdot I^2) \tag{2.5}$$

in which L_{a3} is the 3rd order coefficient of the inductor. The nonlinear BVD model is shown in Fig. 2-9.

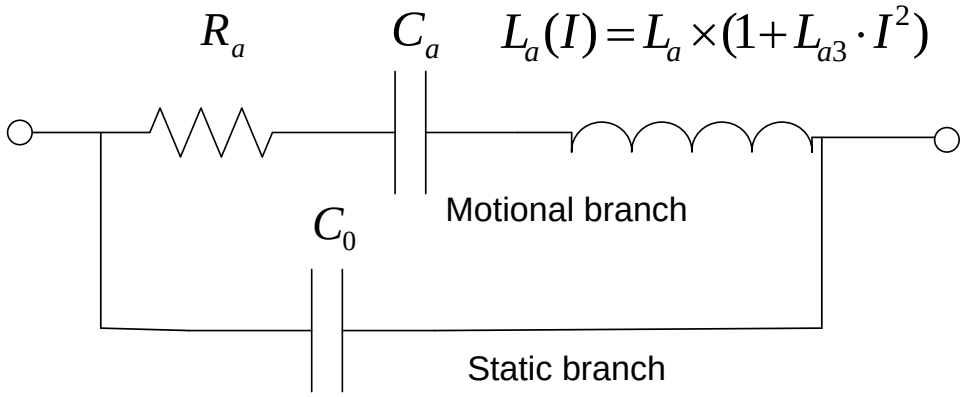

Figure 2-9 The nonlinear BVD equivalent circuit model

The nonlinear BVD model can be simulated directly in the circuit simulators such as Agilent's Advanced Design System [45] or AWR's Microwave Office[46]. In the simulation, the harmonic balance (HB) simulator is used to simulate the nonlinear response from the BVD circuit. The steps of the simulation include the following: first, all the parameters in the BVD model except L_{a3} are directly extracted from the small signal measurements of the resonator, then, nonlinear coefficients of L_{a3} in the BVD model are determined by fitting harmonic simulation results to the measurements. L_{a3} is dependent on both the resonator size and metallization ratio of the IDTs. The model is then tested by simulating both 3rd harmonic and IMD3 of both resonators and duplexers with accuracy.

2.2.3 Nonlinear P-matrix Model

Even though the SAW nonlinear BVD model is easy to integrate into circuit simulators and capable of reaching good agreements between simulations and measurements, the BVD model is only considered as a phenomenological approach. In the BVD circuit, the values of nonlinear coefficients are jointly dependent on both substrate materials and resonator geometric parameters, such as resonator sizes and metallization ratio of the electrodes. Hence nonlinear coefficients have to be manually extracted for different resonator geometries and substrates based on measurements and stored in a database for future simulations. The dependence of nonlinear coefficients to the design parameters puts a limitation on the nonlinear BVD model to be used for simulating broader ranges of resonators. Therefore, more general nonlinear models with nonlinear coefficient assigned to piezoelectric material properties were developed so that the nonlinearity coefficients are independent of the IDT geometries.

The nonlinear p-matrix is recognized as a nonlinear wave model. It was developed in 2010 to 2012 by Solal and the author of this thesis. From publications of [34, 35], the nonlinear p-matrix is built by assuming that the propagation of the surface acoustic wave on a substrate can be described by the equation:

$$\frac{\partial^2 s}{\partial t^2} = v^2 \frac{\partial^2}{\partial x^2}(s + \beta s^2 + r s^3) \tag{2.6}$$

In (2.6), it is assumed that the acoustic wave can be represented by scalar s, where s is the mechanical strain. v is the wave velocity. β and γ are respectively the 2nd order and the 3rd order nonlinearity coefficients. Their origins are in the nonlinear part of the elastic coefficients. In this case, the 3rd harmonics terms are obtained primarily from the mixing of

the 2nd harmonic and the fundamental. The nonlinear part of strain then is added to the regular p-matrix. To solve the nonlinear p-matrix, the perturbation approach is used. First, the device is analyzed for frequencies of the fundamental tones using the standard linear p-matrix model. The results of this analysis are the device admittances and the wave amplitudes along the device at these frequencies. The next step is to do the analysis for the 2nd and 3rd order nonlinearity direct mixing products. At these stages, source terms are added to the p-matrix to represent the generation of mixing products along the propagation. These source terms depend on the wave amplitudes at the fundamental frequencies. The regular propagation reflection and transduction terms at the frequency of the mixing products are also included. The implementation of this model is done by first converting the nonlinear p-matrix into a polynomial relation of harmonic currents and harmonic voltages. Then this relationship is fit into the format of the Frequency Domain Devices so that the harmonic balance simulator inside the commercial circuit software can recognize the format and run the circuit based simulations for the resonators and duplexers. The full details of the nonlinear p-matrix model derivation is written in [43]. The results of the simulations compared to the measurements are shown in Fig. 2-10 and Fig. 2-11. Fig. 2-10 shows the 3^{rd} harmonic measurements and simulations for two different resonators. Fig. 2-11 shows measurement and simulation of IMD3 for a Band 5 single balanced duplexer.

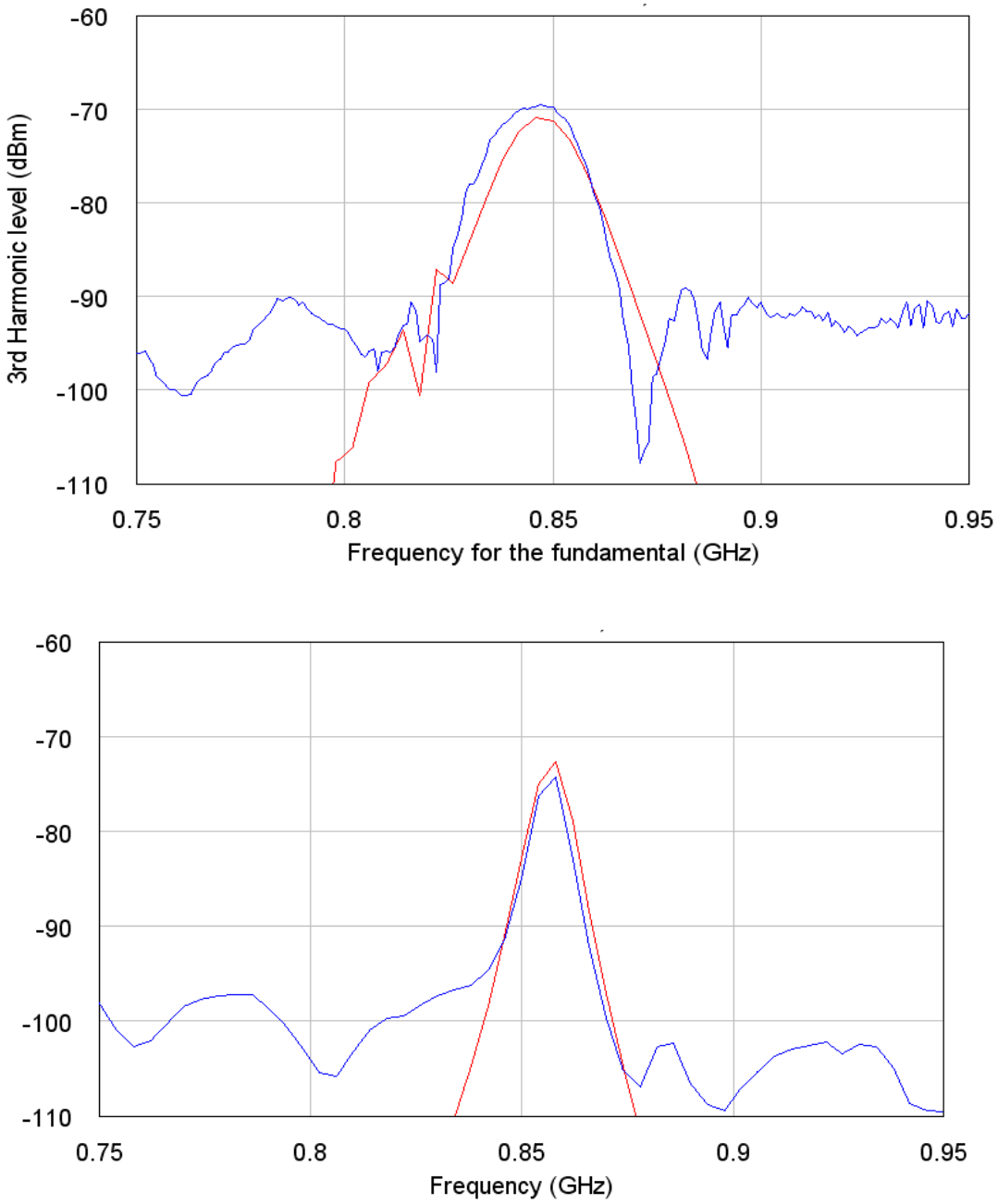

Figure 2-10 3rd harmonic measurements(blue) and simulations(red) for two different resonators. For the first resonator (top), the aperture is 20 wavelengths and the transducer has 100 electrodes. For the first resonator (bottom), the aperture is 40 wavelengths and the transducer has 200 electrodes.

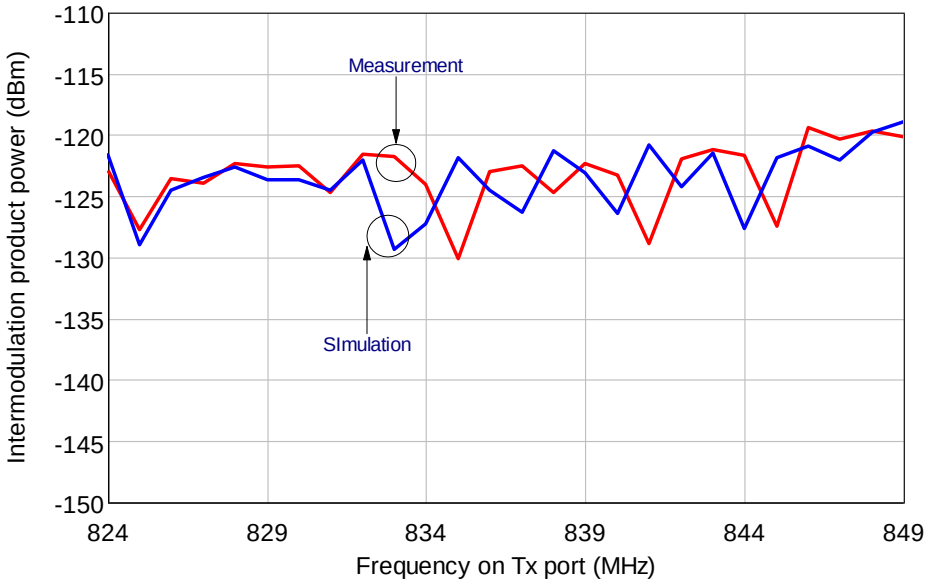

Figure 2-11 Measurement (red) and simulation (blue) of the third order intermodulation product for a band 5 single balanced duplexer

2.3 Uniqueness of Nonlinear Mason Model

Other than the nonlinear BVD model and the nonlinear p-matrix model, the nonlinear Mason model is the new technique to simulate harmonic and intermodulation spurious emissions in SAW devices. Starting from the 1-dimensional wave equations and including a third order nonlinear coefficient in the propagation, the nonlinear Mason model provides better accuracy and convenience as compared to the BVD model and the p-matrix model.

The uniqueness of the nonlinear Mason model can be highlighted as follows:

This is the first physical nonlinear model derived from the physics of acoustic wave propagation and using an equivalent circuit approach to simulate the nonlinear effects of both SAW resonators and duplexers with flexibility and an easy-setup. Due to the equivalent circuit approach, the model can be directly implemented into the commercial circuit

simulators without any need of mathematical conversion. Both the S-parameter and voltage-current based higher order nonlinear spurious responses can be simulated simultaneously with the same circuit. At present, this is also the only equivalent circuit model for SAW nonlinearity simulations which can be directly implemented in commercial circuit simulator while providing the same accuracy as other physical nonlinear models.

Also, the advantage of its equivalent circuit format is that it brings a compatible interface to use the harmonic balance simulator for co-simulating with other front-end components, such as PA and RF switches. Additionally, the S-parameter of the duplexers gives the convenience for checking the duplexers' insertion loss and impedance mismatch between the components.

In addition, the nonlinear Mason could be considered as the simplest approach among the physical models; the unit section of the Mason model is one electrode and it only includes less than ten elements and a constant nonlinear coefficient. The setup of this model inside ADS is easy. The simulation time for a full duplexer normally takes around 5 minutes hence it requires much less time and effort compared to the simulation using other nonlinear physical models.

Overall, the nonlinear Mason model is an efficient physical model governed by piezoelectric constitutive wave equations. Even though it is a 1D equivalent circuit with some assumptions on acoustic wave propagation, the model is still justified by the achievement of good simulation measurement agreements for both SAW resonators and SAW duplexers. This is the first general nonlinear model for SAW devices using equivalent circuit approach and the nonlinear coefficient is independent of design parameters. It also confirms that the SAW's third order nonlinearity could be represented by only one coefficient in the elasticity of the propagation.

CHAPTER 3: NONLINEAR MASON MODEL THEORY

3.1 Overview

The main objective of this chapter is to discuss development of the nonlinear Mason model based on acoustic wave generation and propagation in piezoelectric solids, emphasizing the analogy between acoustic wave propagation by an electrical excitation and electrical transmission line by a current source. As known, the linear Mason circuit model is in the form of distributed transmission lines and it is generally used for understanding and analyzing the IDT structures on the piezoelectric substrates. Since the model governs piezoelectric constitutive equations, Newton's equation of motion and Gauss' Law, it is an accurate physical representation of acoustic wave propagation. Moreover, in this research, it is found that, higher order wave propagation can be modeled by extending the linear Mason model with the nonlinear piezoelectric material property.

After a brief review of wave constitutive equations and pointing out the analogy with transmission line in Section 3.2, the linear Mason model for piezoelectric substrate is inspected in Section 3.3. Then, in Section 3.4, development of the nonlinear Mason model is done by adding a third order coefficient in the elasticity into the propagation line. Section 3.5 introduces the simulation of the SAW resonators by this new nonlinear Mason circuit model without solving the nonlinear differential equations explicitly.

3.2 Review of Acoustic Wave Equations

In a piezoelectric medium, mechanical strain and electric field are coupled through piezoelectricity. Piezoelectric constitutive relations are formed to describe the acoustic wave propagation:

$$T = cS - eE \tag{3.1}$$

$$D = eS + \varepsilon E \tag{3.2}$$

In (3.1) and (3.2), T is the mechanical stress, c is the mechanical stiffness coefficient, S is the mechanical strain, e is the piezoelectricity, E is the electric field, D is the dielectric displacement and ε is the permittivity. It should be noted that T, S, D and E are all vectors with three components each; c, e and ε are tensors. Subscripts are dropped for clarity.

As known, the transmission line model is an ideal prototype to present one dimensional wave propagation phenomena, as long as the power flow can be described by two vectors that vary along one dimension. To apply the transmission line theory to the acoustic wave on piezoelectric substrate, one main concern is that surface acoustic waves have many field components and an exact reduction to the transmission line model is not rigorously possible. However, it was found by previous researches [20, 47] that the surface acoustic wave generated by an electric field can still be modeled properly by a transmission line excited by a current source. Two types of transmission line configurations with different electrical field excitations were developed to model approximately the longitudinal wave generation or shear wave generation [20].

In each case, assuming that the acoustic wave is generated by an electrical field and the wave is propagating along x direction, the strain S and the acoustic vibration velocity v are approximated as:

$$S = \frac{\partial u}{\partial x} \tag{3.3}$$

$$v = \frac{\partial u}{\partial t} \tag{3.4}$$

where u is the mechanical displacement. Subscripts are dropped in the equations for clarity.

Also, mechanical wave has to be subjected to Newton's second law of motion, which is:

$$\rho \frac{\partial^2 u}{\partial t^2} = \frac{\partial T}{\partial x} \tag{3.5}$$

where ρ is the mass density of the substrate.

From (3.4), (3.5) is then written as:

$$\rho \frac{\partial v}{\partial t} = \frac{\partial T}{\partial x} \tag{3.6}$$

Since T is function of the mechanical force F,

$$T = -\frac{F}{A} \tag{3.7}$$

In which A is the area perpendicular to the direction of F. Based on (3.7), (3.6) can be re-written as:

$$\rho \frac{\partial v}{\partial t} = -\frac{\partial F}{A \partial x} \tag{3.8}$$

Meanwhile, from (3.1) to (3.2), the electrical field E can be expressed in the form of D and$S$:

$$E = \frac{D}{\varepsilon} - \frac{e}{\varepsilon} S \tag{3.9}$$

Therefore

$$T = cS - e(\frac{D}{\varepsilon} - \frac{e}{\varepsilon})S$$

$$= (c + \frac{e^2}{\varepsilon})S - e\frac{D}{\varepsilon}$$

$$= c^D S - e\frac{D}{\varepsilon} \tag{3.10}$$

$$\frac{\partial S}{\partial t} = \frac{\partial v}{\partial x} = -\frac{1}{c^D}\frac{\partial}{\partial t}(-T - \frac{e}{\varepsilon} D) \tag{3.11}$$

$$\frac{\partial v}{\partial x} = -\frac{1}{Ac^D}\frac{\partial}{\partial t}(F - \frac{e}{\varepsilon} AD) \tag{3.12}$$

where

$$c^D = (c + \frac{e^2}{\varepsilon}) \tag{3.13}$$

Combining (3.8) and (3.12), the following differential equation system is obtained

$$\begin{cases} \rho \dfrac{\partial v}{\partial t} = -\dfrac{\partial F}{A \partial x} \\ \dfrac{\partial v}{\partial x} = -\dfrac{1}{A c^D} \dfrac{\partial}{\partial t}(F - \dfrac{e}{\varepsilon} AD) \end{cases} \tag{3.14}$$

As detailed in Section 3.3, the system (3.14) can be recognized as the pair of telegraph equations for acoustic wave propagations, with analogy between acoustic state variables (F, v) and standard electrical state variables (voltage U, current i) in transmission equations.

Also, combining the two equations of (3.14) yields a wave equation:

$$\begin{aligned} \rho \frac{\partial^2 u}{\partial t^2} &= \frac{\partial}{\partial x}(c^D S - e \frac{D}{\varepsilon}) \\ &= c^D \frac{\partial^2 u}{\partial x^2} - \frac{e}{\varepsilon} \frac{\partial D}{\partial x} \end{aligned} \tag{3.15}$$

Assuming that the D field is constant along x direction within a unit section, a standard wave equation is found:

$$(c^D \frac{\partial^2}{\partial x^2} - \rho \frac{\partial^2}{\partial t^2}) u = 0 \tag{3.16}$$

The general solution of displacement u from equation (3.16) is the sum of two time dependant plane waves propagating in the $\pm$ x directions at velocity $v = \sqrt{c^D / \rho}$. The wave equation in lossless medium is shown as below,

$$u = (a e^{-jkx} + b e^{jkx}) e^{j\omega t} \tag{3.17}$$

where ω is the angular frequency and wave factor $k = \omega / v$. Both a and b are amplitude constants.

3.3 Examination of the Linear Mason Model

3.3.1 Distributed LC-Circuit Transmission Line

Waves propagating in a transmission line are described by two field quantities, voltage V and current I. A unit length of a transmission line is commonly modeled by a distributed LC-circuit (Fig. 3-1). In this circuit, L is the inductance per unit length, C is the capacitance per unit length. $i(x)$, $i(x+dx)$, $U(x)$ and $U(x+dx)$ present the current and voltage over the unit length dx.

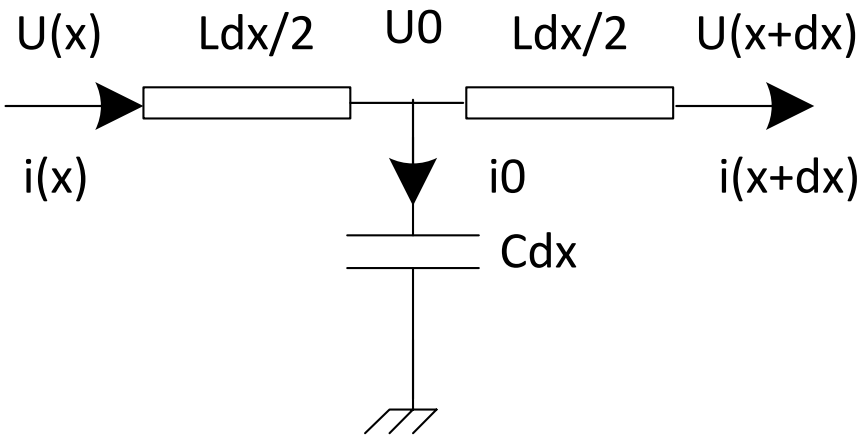

Figure 3-1 A lossless transmission line per unit length

By applying the Kirchhoff's laws to Fig. 3-1, the classical telegraph equations are found easily:

$$U0 = U(x) - \frac{Ldx}{2}\frac{\partial i(x)}{\partial t} \tag{3.18}$$

$$U0 = U(x+dx) + \frac{Ldx}{2}\frac{\partial i(x+dx)}{\partial t} \tag{3.19}$$

where U0 is the voltage at the middle point of the transmission line.

After subtracting (3.18) from (3.19)

$$\begin{aligned} & U(x+dx)-U(x) \\ & =-\frac{Ldx}{2}\frac{\partial}{\partial t}\{i(x+dx)+i(x)\} \\ & \equiv-\frac{Ldx}{1}\frac{\partial i(x)}{\partial t} \end{aligned} \tag{3.20}$$

Also, by applying the current conservation law at the central node of the circuit:

$$\begin{aligned} & i(x+dx)-i(x)=-i0 \\ & =-Cdx\frac{\partial U0}{\partial t}\equiv-Cdx\frac{\partial U(x)}{\partial t} \end{aligned} \tag{3.21}$$

Finally, the classical telegraph equations for the transmission line are found:

$$\frac{\partial i(x)}{\partial x}=-C\frac{\partial U(x)}{\partial t} \tag{3.22}$$

$$\frac{\partial U(x)}{\partial x}=-L\frac{\partial i(x)}{\partial t} \tag{3.23}$$

Combining (3.22) and (3.23) yields the wave equation:

$$\frac{\partial^2 U(x)}{\partial x^2}=LC\frac{\partial^2 U(x)}{\partial t^2} \tag{3.24}$$

Equation (3.24) can be assumed by a traveling voltage and current wave of the form $e^{j(\omega t-kx)}$, then $\frac{\partial}{\partial x}$ can be replace by $-jk$ and $\frac{\partial}{\partial t}$ can be replaced by $j\omega$, so

$$k^2=\omega^2 LC \tag{3.25}$$

where k is the wave number related to the wave length by $k = 2\pi/\lambda$; ω is the radian frequency related to frequency by $\omega = 2\pi f$.

Also, phase velocity is defined as:

$$v_0 = f\lambda = \frac{\omega}{k} = \frac{1}{\sqrt{LC}} \tag{3.26}$$

The characteristic impedance of the transmission line is defined as:

$$Z_0 = \frac{U}{i} = \sqrt{\frac{L}{C}} \tag{3.27}$$

The equation relating the inductance and capacitance to the characteristic impedance and the velocity are:

$$L = \frac{Z_0}{v_0} \tag{3.28}$$

$$C = \frac{1}{Z_0 v_0} \tag{3.29}$$

Examining the forms of the differential equations in (3.14) and (3.22, 3.23), there is a direct analogy that can be made for analysis of the acoustic wave equations with that of the transmission line. By making the following substitution of variables in the forms of the differential equations and derived parameters, the equations yield similar solutions where:

$$U \rightarrow F$$

$$i \rightarrow v$$

$$L \rightarrow \rho A$$

$$C \rightarrow \frac{1}{Ac^D}$$

$$v \rightarrow \sqrt{c^D/\rho}$$

$$Z_0 \rightarrow A\sqrt{\rho \cdot c^D}$$

Therefore, the Mason circuit using Kirchhoff's circuit laws confirms that acoustic wave differential equations are completely analogous to the Mason transmission line and analysis tools can be appropriately applied.

3.3.2 Mason Model per Unit Length

In Chapter 2, the Redwood version of the linear 'in-line' Mason model is introduced; similarly, the Mason model using an LC-circuit per unit length can be shown in Fig. 3-2.

Since the set of the acoustic wave quantities (F, v) shares many similarities with electrical quantities (U, i), it is convenient to assume $U_1 = F_1$, $i_1 = v_1$, $U_2 = F_2$ and $i_2 = v_2$, so validity of the linear Mason model could be examined by applying Kirchhoff's circuit laws (Fig. 3-3). For simplification purpose, the Mason equivalent model below assumes that the acoustic wave propagation loss is negligible.

The port 3 terminal voltage and current are found by:

$$U_3 = -\int_{x_1}^{x_2} E dx \tag{3.30}$$

$$i_3 = A\frac{\partial D}{\partial t} \tag{3.31}$$

Also, from [47], it is known that C_s is the static capacitance per unit length, which could be defined as

$$C_s = \varepsilon w = \frac{\varepsilon A}{dx} \tag{3.32}$$

where w is width of the electrode and A is the area by electrode width and unit length of the transmission line dx.

The ratio of the electromechanical transformer ϕ is defined as

$$\phi = \frac{eA}{dx} = e\frac{C_s}{\varepsilon} \tag{3.33}$$

So the voltage dropped on node c and d (shown in Fig. 3-3) is:

$$U_{cd} = -\frac{1}{(-C_s)}\int \frac{i_3}{2}dt + \frac{1}{C_s}\int \frac{i_3}{2}dt = \frac{AD}{C_s} \tag{3.34}$$

Based on the ratio of the transformer, then the voltage dropped on node a and b is:

$$U_{ab} = U_{cd} \cdot \phi = \frac{AD}{C_s} \cdot e\frac{C_s}{\varepsilon} = \frac{eD}{\varepsilon}A \tag{3.35}$$

Next, by applying the circuit laws on the circuit shown in Fig. 3-3, it is found that:

$$i_0 = i_1 - i_2 \tag{3.36}$$

$$U_0 = \frac{U_1 + U_2}{2} \tag{3.37}$$

$$i_0 = C\frac{\partial}{\partial t}(U_o - U_{ab}) = C\frac{\partial}{\partial t}(U_o - \frac{eD}{\varepsilon}A) \tag{3.38}$$

Since dx is small enough, $U_1 \approx U_2$ and $U = U_0 = (U_1 + U_2)/2$, then

$$\frac{\partial i}{\partial x} = i_2 - i_1 = -C\frac{\partial}{\partial t}(U - \frac{eD}{\varepsilon}A) \tag{3.39}$$

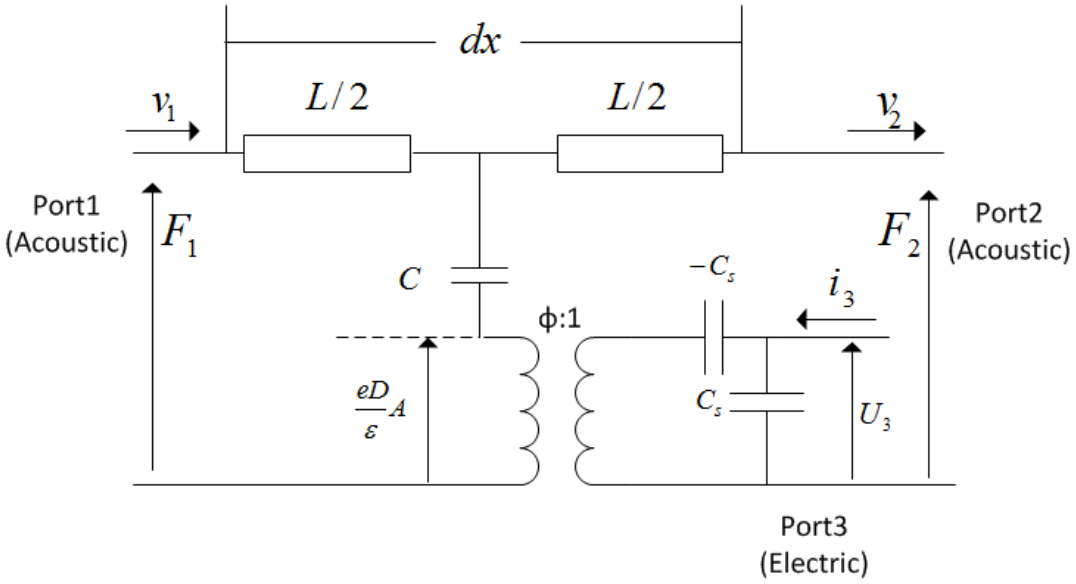

Figure 3-2 An LC-circuit based Mason model per unit length

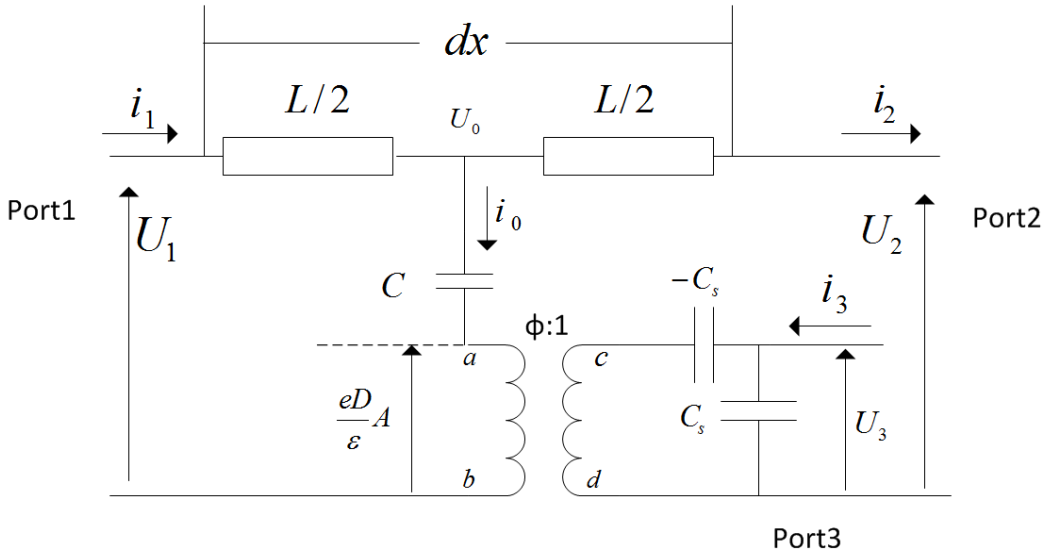

Figure 3-3 Examination of the Mason model by applying Kirchhoff's ciruit laws

3.3.3 Two Types of Mason Models for Interdigital Transducers

The Mason circuit was developed for piezoelectric solids by Mason in the 1940s [48] . Smith, et. al. [20] presented the Mason circuit analysis for SAW interdigital transducers in 1969. Since then, it has been widely used for simulating both SAW and BAW structures.

A unit section of length d of an interdigital transducer (one metalized strip and one gap of the substrate) can be represented by a Mason equivalent circuit (shown in Fig. 3-4) [20]. The length d is normally designed to be a half wavelength of the wave propagating on the substrate at its operation frequency. Therefore, each periodic section is considered to be of length of $2d$ with one pair of electrodes and gaps. To demonstrate, the side view of one periodic section is shown in Fig. 3-5(a) with the direction of actual electrical field indicated. As seen, within one periodic section of the transducer, electrical polarities of the adjacent electrodes inter-change by excitations; the electrical field of such structure can be approximated into two components: one is normal to the wave propagation at x direction, as shown in Fig. 3-5(b); the other one is parallel to the propagation, as shown in Fig. 3-5(c). Since the Mason model is only a one dimensional equivalent circuit approach, the assumption is made that one of the two electrical field components plays a dominant role. If it is assumed that the normal component plays a dominant role, it excites mainly longitudinal waves and the model is called 'crossed-field' model; in the other case, it is assumed that the parallel E field is dominant and it generates mainly shear waves, then the model is called 'in-line' model. The equivalent circuits of the two models differ only by a capacitor with negative capacitance connecting to port 3, shown in Fig. 3-6 (a) and 3-6 (b). In our research, the 'in-line' model provides better accuracy than the 'crossed-field' model to simulate the wave

generation on LiTaO3 substrate. Hence, the following modeling development and its sequential results are only based on 'in-line' Mason model.

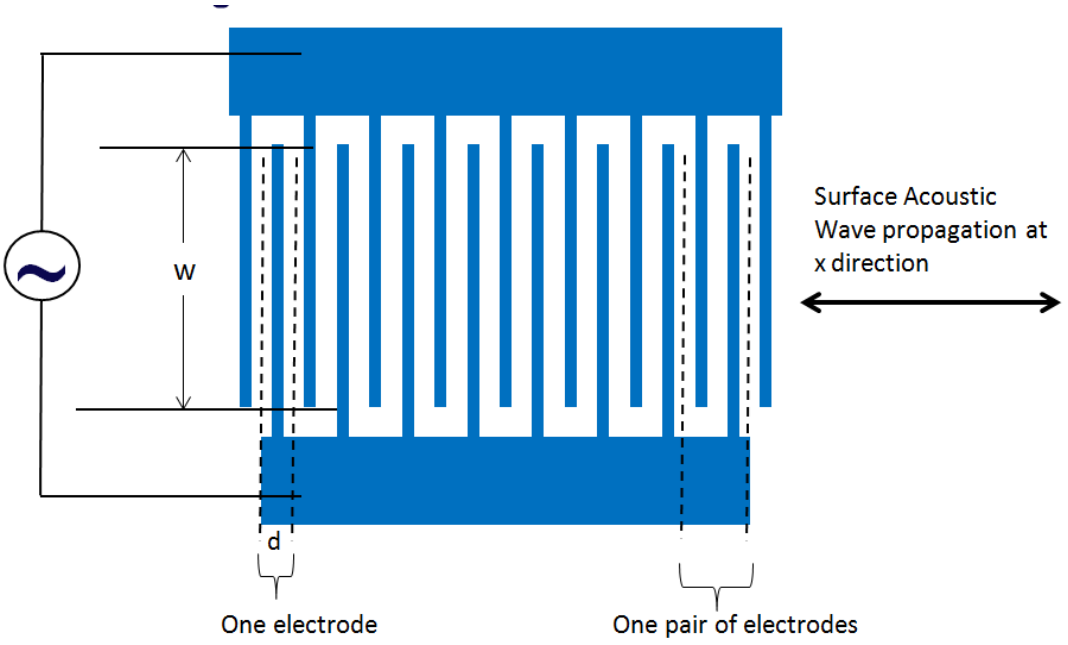

Figure 3-4 Topview of a SAW inter-digital transducer with multiple periodic sections

In previous section, examination of the Mason transmission line per unit length is done. To simulate the SAW interdigital transducer, each unit section is consider to be half wavelength (length of d) and it can be defined by a 3-port Mason circuit network. As shown in Fig. 3-6 (a), ports 1 and 2 are acoustic ports with acoustic wave quantities of (F_1, v_1) and (F_2, v_2), which are the mechanical forces and velocities at the left and right edges. Port 3 is the electrical port with an excitation voltage U_3 and current i_3. C_0 is the static capacitance of the unit section. L and C are the inductor and the capacitor to represent acoustic transmission line

impedance of length of d. As explained previously, (F, v) and completely analogous to (U, i) with the following relationship

$$U_i = \frac{F_i}{\phi} \tag{3.40}$$

$$i_i = \phi v_i \tag{3.41}$$

Therefore, the Mason model could be treated as the regular transmission line model and be simulated in the circuit simulation tool directly.

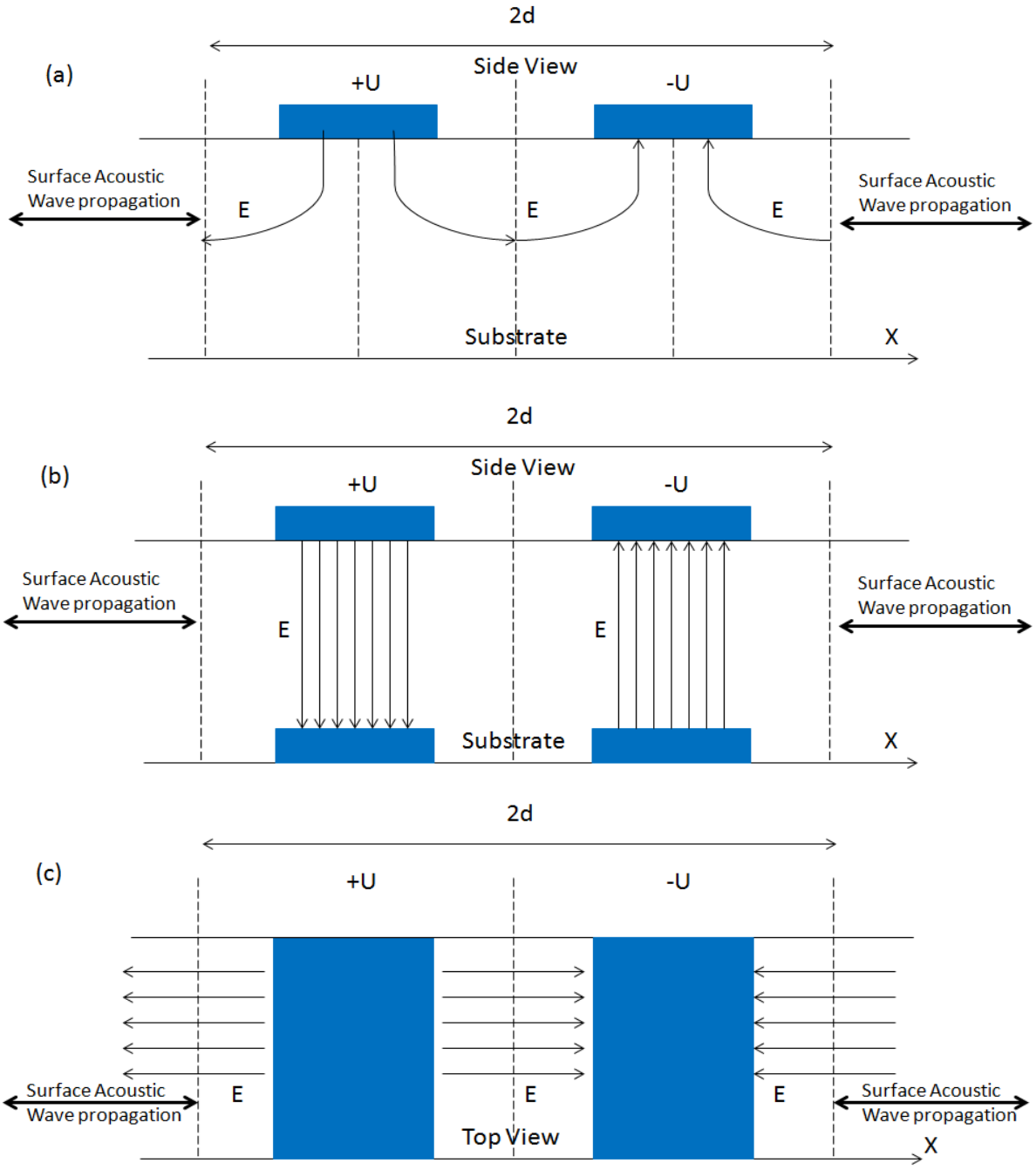

Figure 3-5 (a) Side view of one periodic section of the transducer with directions of electrical field indicated; (b) Side view of one periodic section with approximation that E field direction is normal to the wave propagation at x; (c) Top view of one periodic section with approximation that E field direction is parallel to the wave propagation at x.

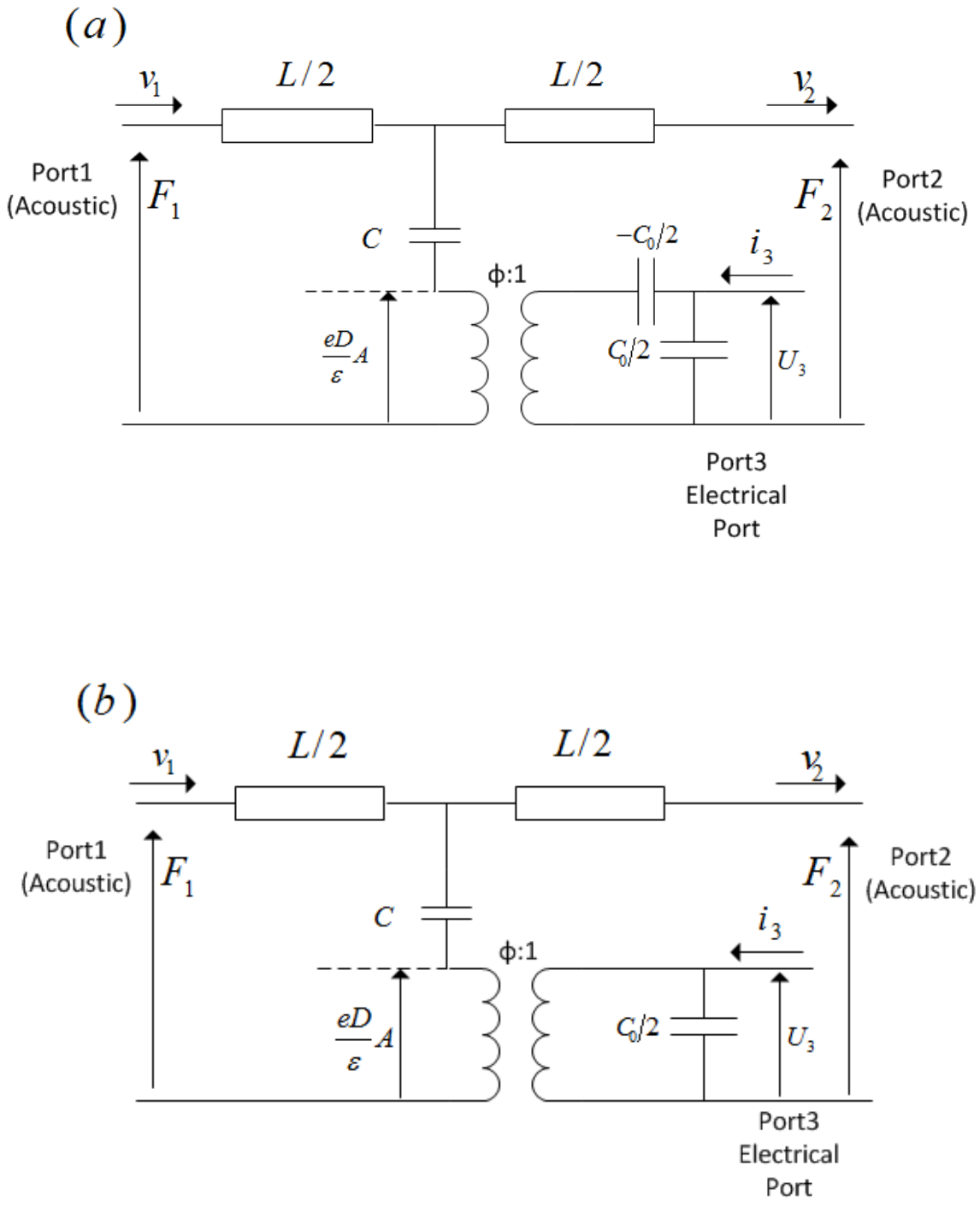

Figure 3-6 (a) 'In-line' Mason equvalent circuit model for one electrode section; (b) 'Cross-field' Mason equvalent circuit model for one periodic section

3.4 Derivation of the Nonlinear Mason Model

After examining the linear Mason equivalent circuit from wave equations, a novel third order nonlinear Mason model is derived in this section. The Redwood version of the Mason circuit [22] is used to build the nonlinear Mason model (Fig. 3-7).

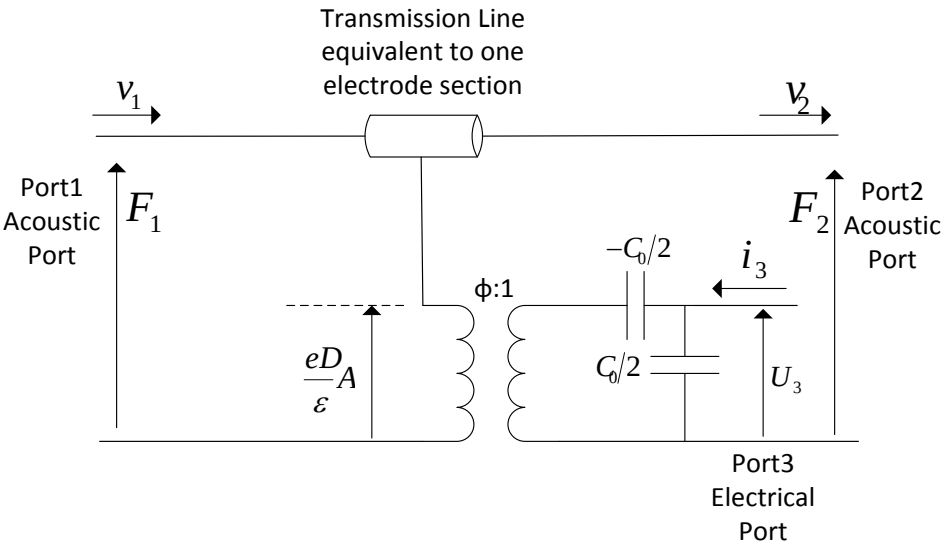

Figure 3-7 Redwood version of linear Mason model for one electrode section of a SAW transducer

Assuming that the nonlinearity of SAW resonators comes from the nonlinear elasticity of the piezoelectric substrate, the development of a nonlinear model can be done by extending the constitutive equations to higher orders. Following the conclusions from the previous researches [34, 43, 44] and the experiments done in this research, the third order nonlinear elasticity of SAW is suspected to be the dominant source. Thus, (3.1) can be extended to the nonlinear term as:

$$T = cS + c_3 S^3 - eE \tag{3.42}$$

At the right side of equation (3.42), the first term represents the linear elasticity and the second term represents the 3rd order nonlinear stiffness coefficient c_3.

From (3.2),

$$D = eS + \varepsilon E \Rightarrow E = \frac{D}{\varepsilon} - \frac{e}{\varepsilon} S \tag{3.43}$$

Combining (3.42) and (3.43)

$$\begin{aligned} T &= cS + c_3 S^3 - e(\frac{D}{\varepsilon} - \frac{e}{\varepsilon} S) \\ &= (c + \frac{e^2}{\varepsilon})S + c_3 S^3 - \frac{eD}{\varepsilon} \\ &= c^D S + c_3 S^3 - \frac{eD}{\varepsilon} \end{aligned} \tag{3.44}$$

In order to solve the nonlinear equation shown above, a perturbation approach is used, assuming:

$$T = T_L + \Delta T \tag{3.45}$$

$$S = S_L + \Delta S \tag{3.46}$$

$$v = v_L + \Delta v \tag{3.47}$$

$$u = u_L + \Delta u \tag{3.48}$$

$$D = D_L + \Delta D \tag{3.49}$$

$$F = F_L + \Delta F \tag{3.50}$$

where T_L, S_L, v_L, u_L, D_L and F_L are the linear terms of stress, strain, velocity, mechanical displacement, dielectric displacement and mechanical force; ΔT, ΔS, Δv, Δu, ΔD and ΔF are the extended nonlinear terms of stress, strain, velocity, mechanical displacement, dielectric displacement and mechanical force.

Then, by applying the equations (3.45), (3.46) and (3.49) to (3.44), the equation can be re-written as:

$$T_L + \Delta T = c^D (S_L + \Delta S) + c_3 S^3 - \frac{e(D_L + \Delta D)}{\varepsilon} \tag{3.51}$$

The linear part of (3.51) is:

$$T_L = c^D S_L - e\frac{D_L}{\varepsilon} \tag{3.52}$$

Substituting (3.3) for S into (3.52) yields,

$$T_L = c^D (\frac{\partial u_L}{\partial x}) - e\frac{D_L}{\varepsilon} \tag{3.53}$$

Taking a time derivative on (3.53) yields

$$\frac{\partial T_L}{\partial t} = c^D \frac{\partial v_L}{\partial x} - \frac{e}{\varepsilon}\frac{\partial D_L}{\partial t} \tag{3.54}$$

$$\frac{\partial \{-v_L\}}{\partial x} = -\frac{1}{c^D}(\frac{\partial T_L}{\partial t} + \frac{e}{\varepsilon}\frac{\partial D_L}{\partial t}) \tag{3.55}$$

On the other hand, the Newton's second law of motion can be written as:

$$-\rho\frac{\partial\{-v_L-\Delta v\}}{\partial t}=\frac{\partial\{T_L+\Delta T\}}{\partial x} \tag{3.56}$$

(3.56) can be separated into two parts:

$$-\rho\frac{\partial\{-v_L\}}{\partial t}=\frac{\partial\{T_L\}}{\partial x}=-\frac{\partial\{F_L\}}{A\partial x} \tag{3.57}$$

$$-\rho\frac{\partial\{-\Delta v\}}{\partial t}=\frac{\partial\{\Delta T\}}{\partial x}=-\frac{\partial\{\Delta F\}}{A\partial x} \tag{3.58}$$

Therefore, the linear equations (3.55) and (3.57) are recognized as a linear pair of telegraph equations with mechanical state variables (F_L, v_L).

Additionally, solving for the nonlinear part starts from the nonlinear part of (3.51):

$$\Delta T=c^D\Delta S+c_3S^3-e\frac{\Delta D}{\varepsilon} \tag{3.59}$$

Since

$$S=\frac{1}{c^D}(T+e\frac{D}{\varepsilon}) \tag{3.60}$$

Then,

$$\Delta T=c^D\Delta S+\frac{c_3}{(c^D)^3}\left\{T+e\frac{D}{\varepsilon}\right\}^3-e\frac{\Delta D}{\varepsilon} \tag{3.61}$$

Equation (3.61) could be also written as:

$$\frac{\partial\{-\Delta v\}}{\partial x} = -\frac{1}{c^D}\frac{\partial}{\partial t}\left\{\Delta T + e\frac{\Delta D}{\varepsilon}\right\} + \frac{c_3}{(c^D)^4}\frac{\partial}{\partial t}\left\{T + e\frac{D}{\varepsilon}\right\}^3 \tag{3.62}$$

By combining (3.55) and (3.62) together,

$$\frac{\partial\{-v_L\}}{\partial x} + \frac{\partial\{-\Delta v\}}{\partial x} = -\frac{1}{c^D}\frac{\partial}{\partial t}(T_L + e\frac{D_L}{\varepsilon}) - \frac{1}{c^D}\frac{\partial}{\partial t}\left\{\Delta T + e\frac{\Delta D}{\varepsilon}\right\} + \frac{c_3}{(c^D)^4}\frac{\partial}{\partial t}\left\{T + e\frac{D}{\varepsilon}\right\}^3 \tag{3.63}$$

Therefore,

$$\frac{\partial\{-v\}}{\partial x} = -\frac{1}{c^D}\frac{\partial}{\partial t}\left\{\left\{T + e\frac{D}{\varepsilon}\right\}\left\{1 - \frac{c_3}{(c^D)^3}\left\{T + e\frac{D}{\varepsilon}\right\}^2\right\}\right\} \tag{3.64}$$

Since $F = -AT$, then

$$\frac{\partial\{-v\}}{\partial x} = \frac{1}{Ac^D}\frac{\partial}{\partial t}\left\{\left\{F - e\frac{D}{\varepsilon}A\right\}\left\{1 - \frac{c_3}{A^2(c^D)^3}\left\{F - e\frac{D}{\varepsilon}A\right\}^2\right\}\right\} \tag{3.65}$$

Comparing (3.65) to (3.39), analogy between term $F - eDA/\varepsilon$ in (3.65) and term $U - eDA/\varepsilon$ is found. $U - eDA/\varepsilon$ is defined as the voltage drop on the capacitor of the transmission line.

Also, in a circuit simulator, a second and third order voltage dependant current source could be defined into a voltage dependant capacitor (Fig. 3-8):

$$C = C_0(1 + cc_1 V + cc_2 V^2) \tag{3.66}$$

where C_0 is the linear capacitance, cc_1 is the normalized second order coefficient with voltage dependence and cc_2 is the normalized third order coefficient with square voltage dependence.

The current flows through this capacitor can be defined as:

$$i = C\frac{dV}{dt} = C_0\frac{d}{dt}\{V(1 + cc_1 V + cc_2 V^2)\} \tag{3.67}$$

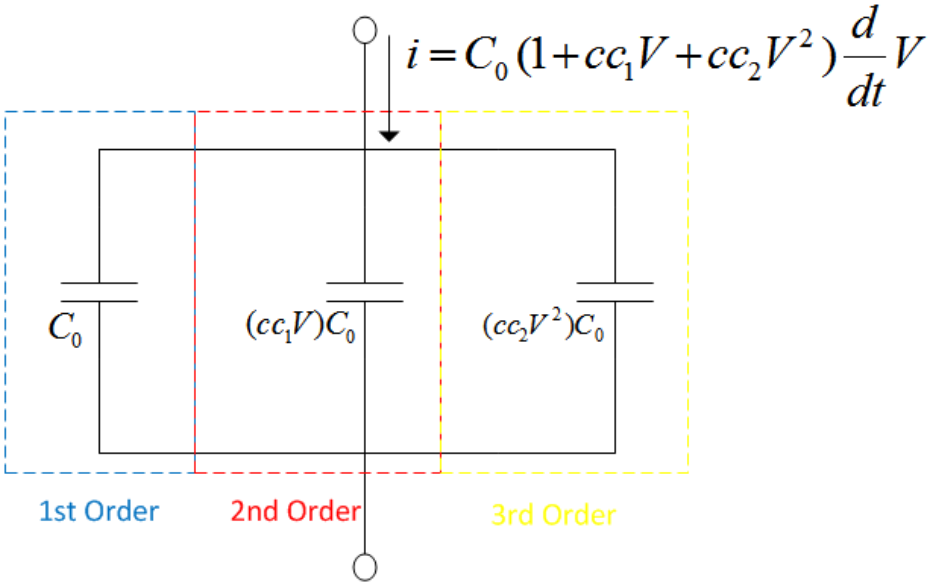

Figure 3-8 Demonstration of a nonlinear capacitance

Comparing (3.67) to (3.65), the follow analogy is noticed:

$$C_0 \rightarrow 1/Ac^D$$

$$cc_1 \rightarrow 0$$

$$V \rightarrow (F - \frac{eD}{\varepsilon} A)$$

$$C_{NL} = (cc_2 V^2) C_0 \rightarrow -\frac{c_3}{A^3 (c^D)^4} (F - \frac{eD}{\varepsilon} A)^2$$

where $C_{NL}$is the overall nonlinear capacitance for each transmission line section.

The implementation of the nonlinear term into the Mason circuit for one electrode section is shown in Fig. 3-9. The keys to model the third order nonlinearities correctly are: first of all, the equivalent transmission line of one electrode is separated into N sub-sections and an individual nonlinear capacitor is added to cross each sub-section of the transmission line; secondly, to insert the nonlinear terms based on the telegraph equations derived in (3.65), the first order capacitor is modeled inside the regular transmission line elements; the second order capacitor ($cc_1 V C_0$) is ignored; the third order capacitor is modeled by using a voltage dependant capacitor to cross the each sub-section of the transmission line with capacitance of C_{NL}. The meaning of this nonlinear capacitor is that it creates a nonlinear current source depending on the cubic term of $(F - e\frac{D}{\varepsilon} A)$. Further, it is found that the nonlinear Mason circuit in Fig. 3-9 can be simplified by setting N=1 (Fig. 3-10) with almost no impact on simulation results, with comparison to the simulation by setting N=10. In that case, each electrode section can be represented by a single nonlinear capacitor and a single section of transmission line. This results in a large reduction of the computation time. The nonlinear coefficient of the capacitor is later determined by fitting the simulation to the resonator intermodulation measurement results.

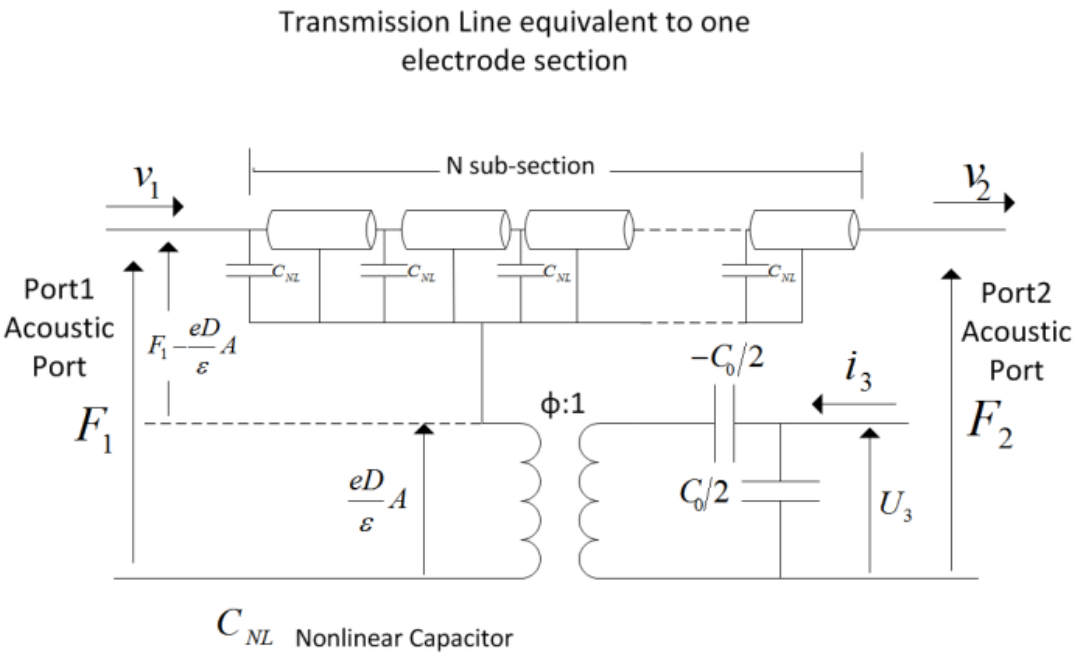

Figure 3-9 The nonlinear Mason model for one electrode section of a SAW transducer. The transmission line is splited into N sections.

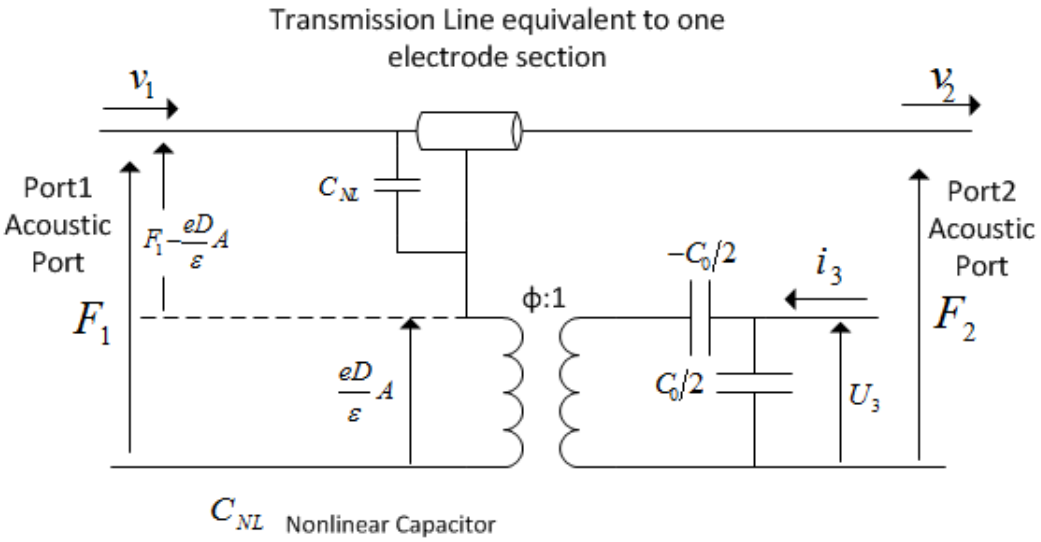

Figure 3-10 The simplified nonlinear Mason model for one electrode section of a SAW transducer by setting number of the sub-sections to N=1

3.5 Simulations of SAW Resonators

One electrode section of the nonlinear Mason circuit is demonstrated in section 3.4. In this section, simulation of a SAW resonator is shown.

In order to simulate a full resonator with a transducer (with N electrodes) in the middle and 2 gratings (with N_g electrodes each) at the sides (Fig. 3-11), simulations of the transducer and the gratings are done separately. The transducer section simulation is done by cascading multiple unit Mason circuits (of one electrode section) by their ports 1 and ports 2 and connecting their electrical ports 3 in parallel; electrical excitations between the adjacent electrodes are assigned with opposite polarities. A block diagram to simulate the transducer section of a SAW resonator with N electrodes is shown in Fig 3-12. A 3-port network is used to simulate the whole transducer. Similarly, simulations of the grating sections are done by cascading multiple unit Mason circuits (of one electrode section) by their ports 1 and ports 2; however, the electrical ports 3 are left open in the gratings (Fig. 3-13). The whole resonator simulation is then finished by combining the transducer and grating sections by their acoustic ports in series. Also, the acoustic characteristic impedance of the transmission line is used to terminate at the end of transmission lines at gratings. Simulations are done in ADS; setups and results are explained in Chapter 5.

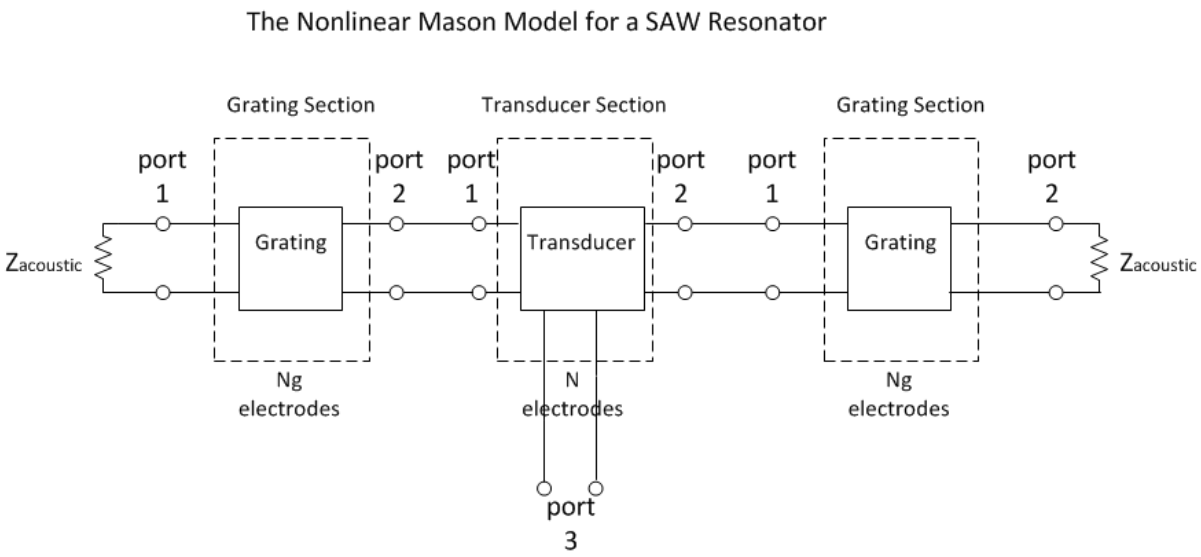

Figure 3-11 A simulation block diagram of a complete SAW resonator by the nonlinear Mason model

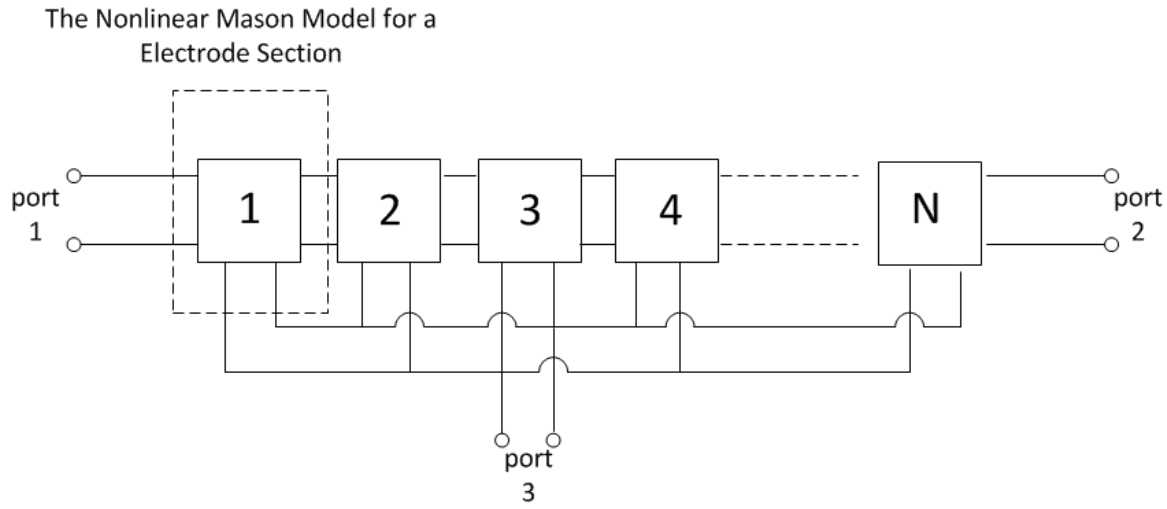

Figure 3-12 A simulation block diagram of a SAW tranducer section with N electrodes by the nonlinear Mason model

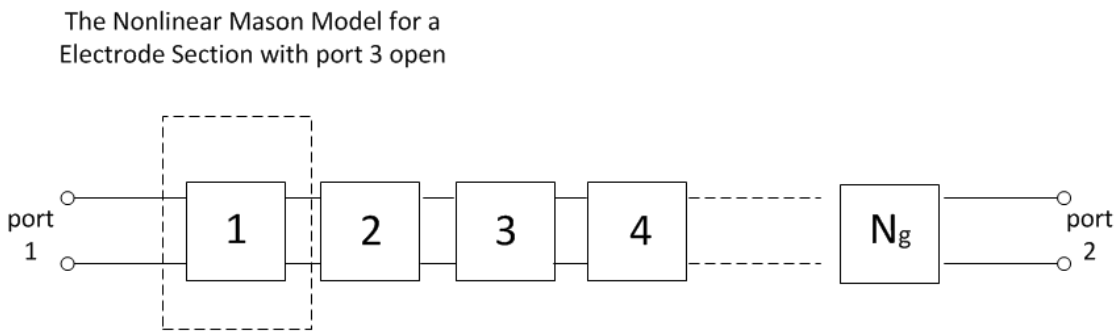

Figure 3-13 A simulation block diagram of a SAW grating section with N_g electrodes by the nonlinear Mason model

CHAPTER 4: NONLINEARITY MEASUREMENTS

4.1 Overview

In order to measure the nonlinear effects of SAW resonators and validate the nonlinear Mason model developed in Chapter 3, another contribution of this Ph.D. study is to successfully define a large signal nonlinearity measurement system to for the test of passive SAW devices. Reliable measurement results were demonstrated showing trends of nonlinear distortions with different resonator geometries. The influence of the test setup is also considered.

As known, although nonlinearity measurement for active devices is common, its methodology is not directly applicable to test RF duplexers due to: a), nonlinearity of SAW devices is relatively weak. Without precautions, the nonlinearities of test equipments and peripheral circuits can mask the SAW nonlinearities; b), power handling capability of SAW devices are limited; maximum input power to apply on SAW devices is around 33dBm; c), under large signal tests, it is found that self-heating effect impacts the frequency responses of SAW devices, so it is important to choose the test approaches by which the test results are insensitive to the self-heating impact. Overall, performing large signal nonlinearity measurements on SAW duplexers is difficult and no methodology was defined by previous publications.

In this research, the input signals are frequency swept and spectrum analysis is used to measure spurious emission levels of harmonic and intermodulation products, because: a), harmonic and intermodulation distortion of SAW duplexers are more significant than other nonlinear effects; b) they are not sensitive to self-heating effect; c) both harmonics and

intermodulation are specified by 3GPP standards so the measurement results are meaningful at system level.

In order to perform the measurements, various single-pole SAW resonators with length, aperture (width), pitch, duty factor and wafer cut variations were defined and simulated. The resonators were then laid out, fabricated, and tested by the test system developed. Measurement results of these 1-pole resonators are used to characterize the nonlinear properties, determine the nonlinear coefficients C_{NL} in the nonlinear model as well as to verify the simulation accuracy. Finally, the measurement system also successfully measures the harmonic and intermodulation distortions of a Band 5 duplexer.

This chapter is organized as follows: in Section 4.2, test resonators are defined and features on these resonators are explained; in Section 4.3, on-wafer large signal measurement setups are demonstrated. The challenges to test the resonators on wafer are discussed, influence of setup is considered; then, in Section 4.4, SAW test resonator measurement data are analyzed and plotted, characterization of SAW resonators' nonlinearity are done by analyzing the trends of both 2nd and 3rd harmonics with different design parameters; finally in Section 4.5, IMD2 and IMD3 measurements on a WCDMA Band 5 800MHz duplexer are discussed and results are shown.

4.2 On-wafer Test Resonators

Multiple 1-pole test resonators are designed based on a reference design. The reference resonator is a synchronous resonator on lithium tantalate YXl42°(LT42), with an electrode pitch of 2.4 μm, an acoustic aperture (width) of 20 wavelengths, a transducer length of 100

wavelengths (200 electrodes), a grating (reflector) length of 10 wavelengths and a duty factor (DF) of 50%. The layout of the reference resonator is shown in Fig. 4.1, in which definitions of aperture and length are indicated. In Fig. 4-2, the length of the metalized section of each electrode is defined as a, b is the gap between two adjacent electrodes and pitch is the total length of a and b; duty factor is defined as the metallization ratio of metal electrode length a over the pitch. Also, the layouts of all the test resonators have been designed to be capable of being wafer probed using either 1-port or 2-port measurements (Fig. 4-1). As simulated, the resonance frequency (f_s) of the reference resonator is about 800 MHz and its anti-resonance frequency (f_p) is around 825MHz. Once the reference resonator is defined, a large group of resonators with different lengths, aperture, metallization ratio and pitches are defined and drawn on the mask. All the test resonators are simulated by the linear COM model. These test devices are manufactured on both lithium tantalate YXl42° (LT42) and YXl48° (LT48) wafers with deposition of 4700Å thick aluminum.(YXl42° and YXl48° refer to two different crystal cut angles of the wafers.) Table 4-1 lists the matrix of all the geometric variation of the test devices.

Table 4-1 Matrix of geometry variation of the 1-pole test resonators

	Geometry Variation				
DF (%)	45	50	55	60	
Aperture (λ)	10	20	25	30	40
Pitch (μm)	2.4	2.35	2.30	2.2	2.0
Length (λ)	50	100	200		
Wafer Cut	LT 42	LT 48			

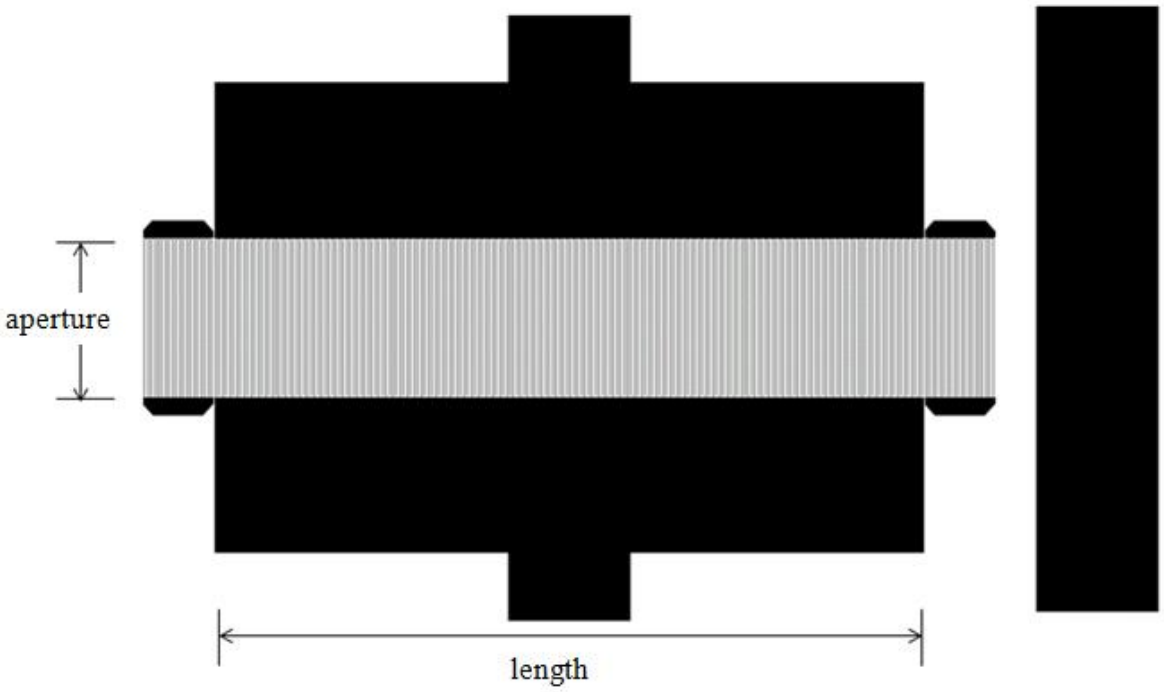

Figure 4-1 Layout view of the 1-pole reference resonator at 800MHz

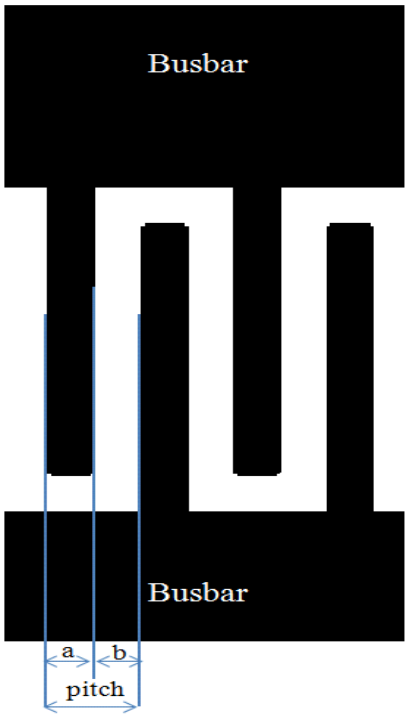

Figure 4-2 Zoom-in view of the 2 pair of eletrodes of the reference resonator

4.3 Resonator Measurements

Once the test resonators are fabricated, all the test resonators are measured by:

a) small signal S-parameter measurements;

b) 2^{nd} and 3^{rd} harmonic measurements;

c) IMD2 and IMD3 measurements.

A wafer prober is used for the resonator measurements. Wafer probing is an effective way to test integrated circuits (IC) on-wafer since measurements can be done quickly and easily without the post-fabrication processes such as wafer dicing, die assembly or PCB soldering. However, challenges of using wafer probing are:

First of all, wafer level probing test is a common die screening test in production. However, accuracy of manual probing measurements is sensitive to the contact resistance and the capacitance between the wafer and probe tips. Ideally, a 50 ohm signal is provided to the device under test (DUT) but the impedance could vary if probe tips do not make a good contact with the wafer; probe tips are damaged; or grounding condition is not sufficient. Therefore, probe calibration is important and repeated measurements are needed to check the reliability of the test.

Secondly, if probe tips are excited with large signals, shielding around the probe tips are important to decouple the parasitic capacitance in order to provide a clean noise floor to the test system. It is found that comparing to the measurement using SMA connectors with device mounting on the PCB, the noise floor is degraded when using wafer probing; certain probe tips could also create spurious signals stronger than the nonlinearity generated by SAW resonators. In such situation, nonlinearity of SAW devices is too weak to be tested.

Therefore, the test setup has to be carefully tuned to guarantee high dynamic range including using highly-linear probe tips.

Thanks to the support from TriQuint Semiconductor, all the measurements were done in the RF lab of TriQuint Semiconductor Inc in Apopka, FL. The following pictures were taken from the measurements: Fig. 4-3 shows a picture of the wafer probe station running a harmonic test on a wafer. Fig. 4-4 shows the large signal test system to test IMD of SAW resonators using wafer probes.

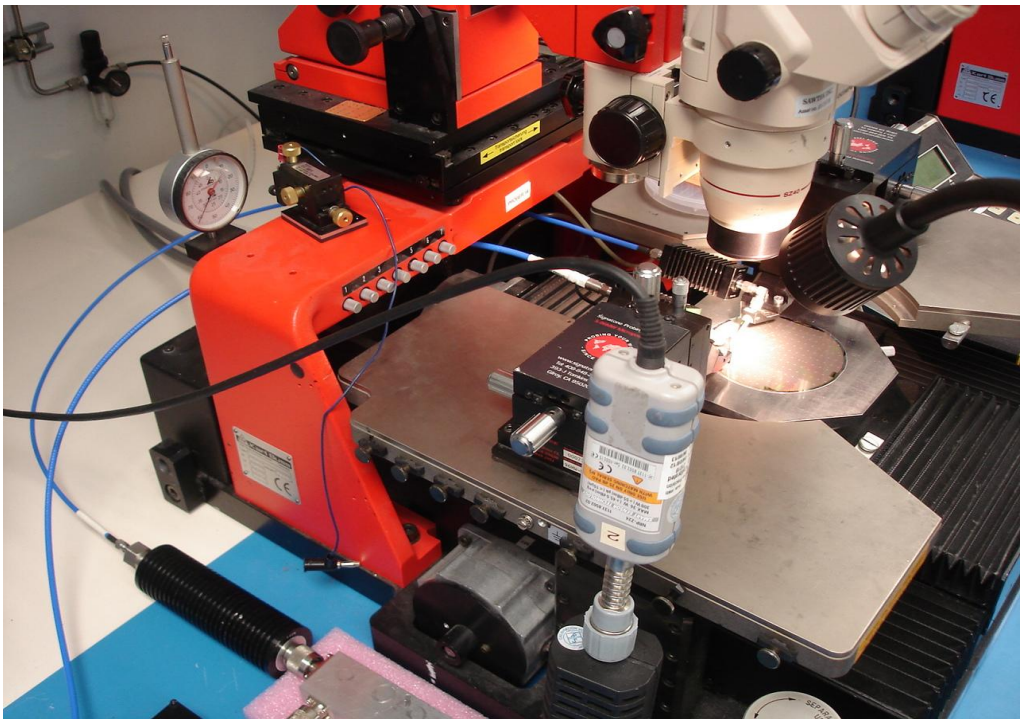

Figure 4-3 Photograph of wafer probe station in the lab of TriQuint Semiconductor Inc.

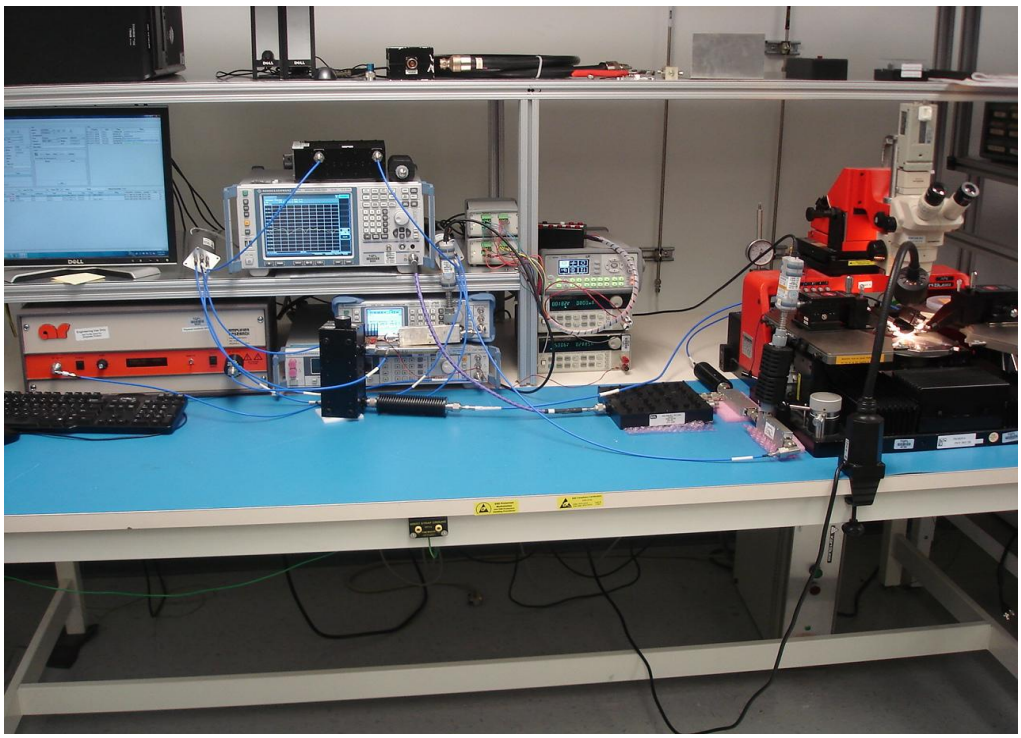

Figure 4-4 The large signal test system to test IMD of SAW resonators

4.3.1 S-parameter Measurement

S-parameter is the most efficient way to characterize resonators' impedances and quality factors. In our research, all the test resonators are measured by a network analyzer first to collect the S-parameters. Resonator frequency responses as well as impedances are benchmarked. Also, measurement results are compared with simulations to check whether expectations are met. For example, the frequency response of 1-port S-parameter measurement of the reference resonator is shown in Fig. 4-5. Impedance response Z_{11} is used for the plot. By calculation, Q factor of the resonance is around 1200 and Q factor of the anti-resonance is around 700. It is a uniform response of a 1-pole SAW resonator and it is

predicted by a COM model. Overall, good simulation and measurement correspondence is achieved, indicating the device is designed and fabricated properly.

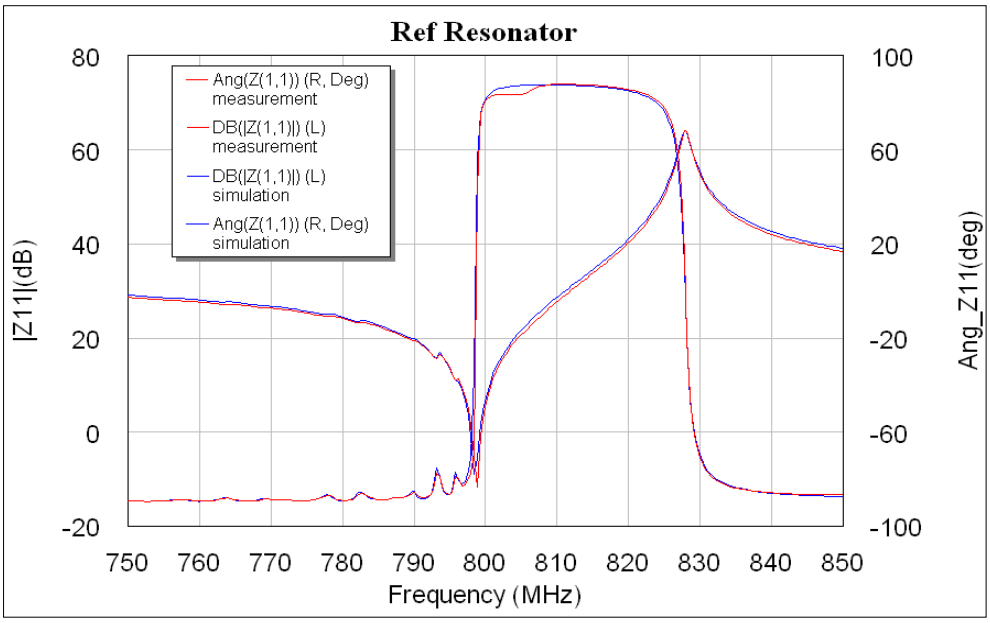

Figure 4-5 Small signal impedance response of the reference resonator; trace in blue is from COM model simualtion and trace in red is from probe measurement

4.3.2 Harmonic Measurements

After small signal S-parameter measurements, single-port single-tone harmonic measurements are done to measure the reflected spectrum of the test resonators under large CW signals. Signal outcoming from the power amplifier (PA) is connected via a cable to a probe tip on the wafer probe station and then fed on the resonator. Schematic diagram of the harmonic measurement is shown in Fig.4-6. In the setup, a CW signal coming out the PA excites the resonator at fundamental frequency (f_0) while the reflected energy is input into the spectrum analyzer. The input signal frequency f_0 sweeps from 750MHz to 950MHz by the signal generator (SG). The reflected power is collected at frequency spectrum of f_0 (first

harmonic, H1), $2f_0$ (second harmonic, H2) and $3f_0$ (third harmonic, H3). Both input and reflected power levels are calibrated and monitored to the end of probe tip. Also in the test system, a directional coupler and attenuators (ATT) are used to provide enough attenuation to protect the PA from the strong reflected power; a low pass filter (LPF) following the PA and a high pass filter (HPF) before the spectrum analyzer are used to suppress the spurious interference from PA and the spectrum analyzer and improve noise floor of the test system. To ensure that harmonics of the DUT can be clearly separated from the noise floor, a probe measurement of an open structure on the wafer is also done. Results are shown in the next section.

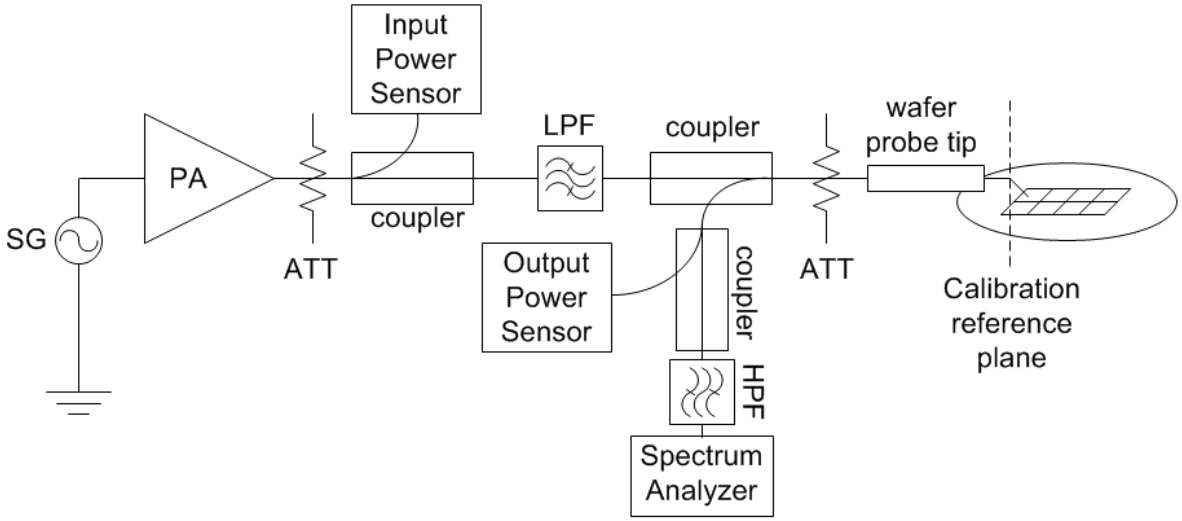

Figure 4-6 Schematic diagram of the harmonic measurement

4.3.3 Intermodulation Measurements

Besides the 1-tone harmonic measurements, 2-tone intermodulation measurements on test resonators are also taken with wafer probers. Both IMD2 and IMD3 tests are done under the same test setup. 2-tone intermodulation measurements of the test resonators are the keys to

validate the nonlinear model developed, even though single-tone harmonics results provide sufficient information for nonlinearity characterizations of different resonators. In the meantime, the on-wafer intermodulation measurement is also a more complicated test than the harmonic measurement since it is a 2-tone, 2-port test, comparing to the 1-tone, 1-port test for the harmonic measurement. Also, frequencies of tones are often set to be close to each other.

Fig. 4-7 and Fig. 4-8 show the schematic diagrams of a 2-tone, 2-port test bench to test IMD performance of the reference resonator. On Fig. 4-7, the resonator is connected in series to measure the transmit signals from port 1 to port 2; in Fig. 4-8, the resonator is connected in shunt to measure the reflected signals at port 1. Different resonator connections give different spurious level of intermodulations. Meanwhile, test setups are configured to be capable to take both IMD2 and IMD3 measurements with helps of two RF switches and band pass filters (BPF).

The setup of the intermodulation test on the reference resonator is explained as follows: at port 1 side, Tone 1 (at f_1 frequency) from SG1 is the main signal tone at 25dBm sweeping from the frequency from 790MHz to 835MHz. BPF1 is a tunable filter to pass the signal at f_1 frequency band while attenuating the off-band spur from PA; at port 2 side, SG2 of Tone 2 is capable of generating jammer signals (at f_2 frequency) at 0dBm for either IMD2 or IMD3 tests: In the case of IMD2 test, SG2 generates the signal at 55MHz and RF switch 1 and RF switch 2 are both turned on to the path of BPF2 to pass the signal at 55MHz; on the other hand, in the case of IMD3 test, SG2 generates the signal 55MHz lower than f_1 (from 735MHz to 780MHz) and RF switch 1 and RF switch 2 are then switched to the path of BPF3 so signals within 735 MHz and 780 MHz could be passed. Powers of both tones are

calibrated to the end of the probe tips; Tone 1 and Tone 2 mix at device under test (DUT) and IMD product is then generated by the reference resonator at sweeping frequencies of 845 MHz to 890 MHz; a spectrum analyzer at port 2 is used to measure the spectrum. BPF4 in front of the spectrum analyzer is responsible for only passing IMD signals while attenuating both Tone 1 and Tone 2 signals to prevent deterioration of the dynamic range by the spectrum analyzer linearity. Also, multiple directional couplers and attenuators are implemented in the setup to improve the test dynamic range. Validity of the test setup is done by measuring a 'through' structure to measure the noise floor the test system. In order to better demonstrate the test, the frequency spectrum of an IMD2 test is shown in Fig. 4-9 and the frequency spectrum of an IMD3 test is shown in Fig 4-10. Meanwhile, test frequencies and power configuration of IMD2 and IMD3 tests on the resonators are listed Table 4-2.

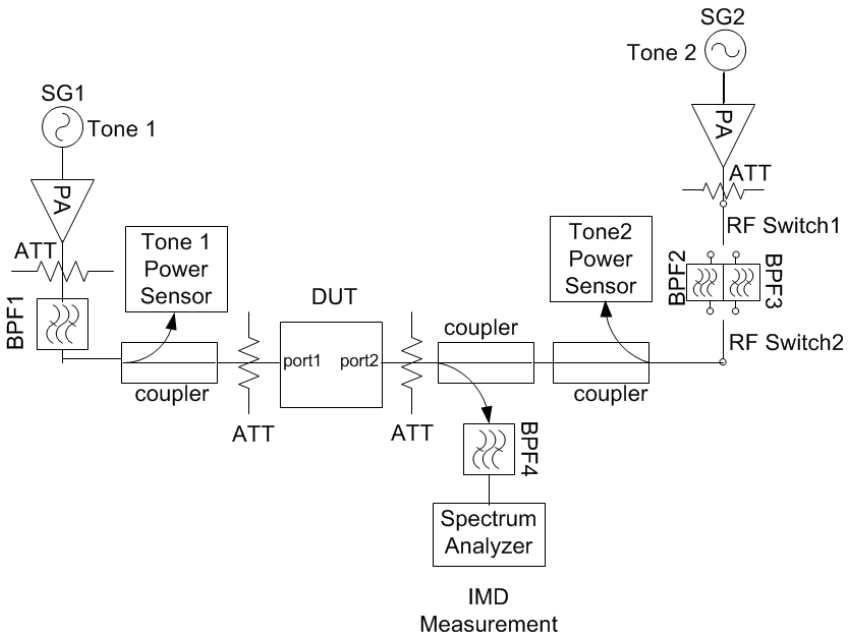

Figure 4-7 Schematic diagram of a typical 2-port IMD2/IMD3 measurement on a series resonator

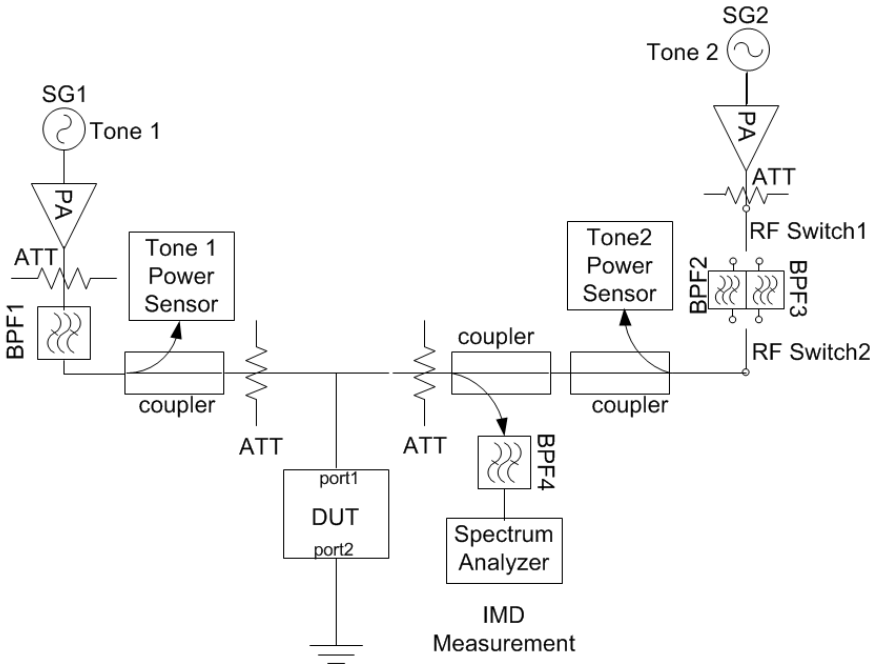

Figure 4-8 Schematic diagram of a typical 2-port IMD2/IMD3 measurement on a shunt resonator

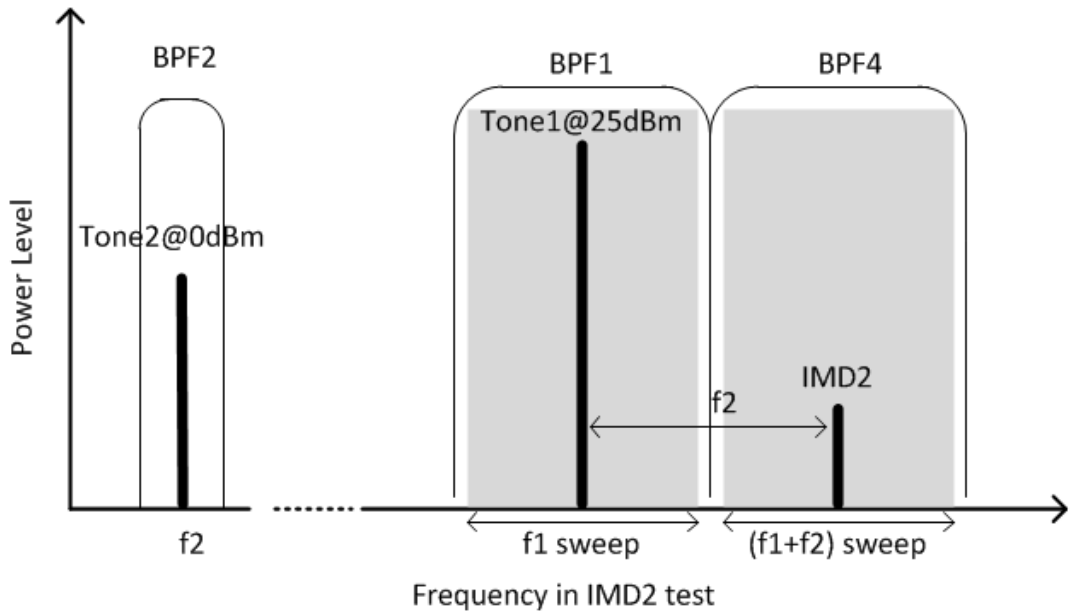

Figure 4-9 Specturm demonstration of the signals in an IMD2 test

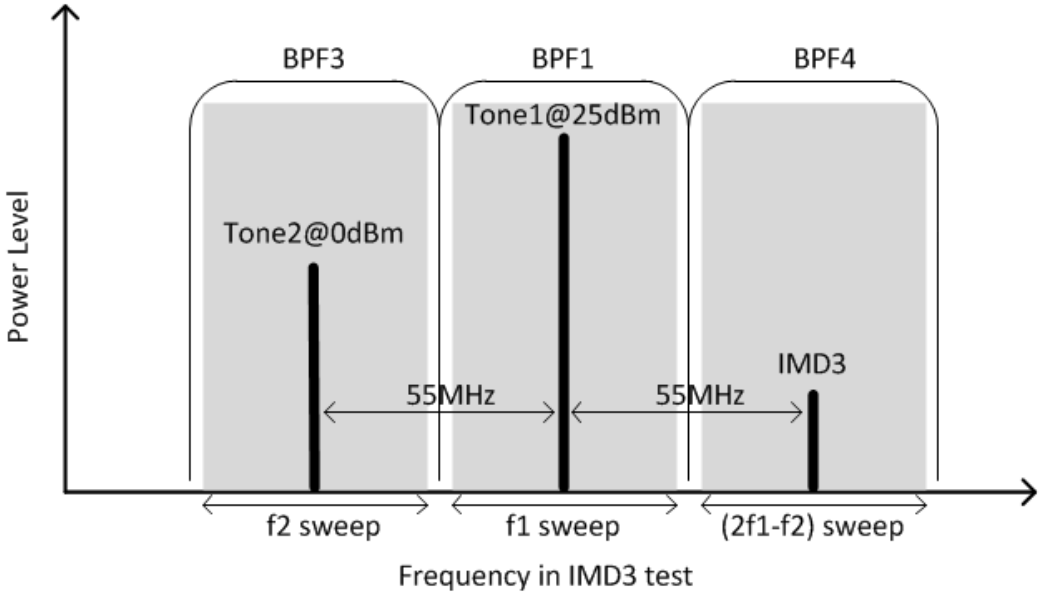

Figure 4-10 Specturm demonstration of the signals in an IMD3 test

Table 4-2 IMD test conditions for the reference resonator

		Sweep Freq (MHz)		Power (dBm)
IMD2 measurement	Tone1 (f1)	790	835	25
	Tone2 (f2)	55	55	0
	IMD2 (f1+f2)	845	890	To be measured
IMD3 measurement	Tone1 (f1)	790	835	25
	Tone2 (f2)	735	780	0
	IMD3 (2f1-f2)	845	890	To be measured

4.3.4 Considerations for Measurement Setup

Nonlinearity measurements on SAW devices are acknowledged as very complex measurements: the nonlinear effects of SAW are weak so it is difficult to test the nonlinearity created by the SAW devices from test system's noise floor. Therefore, influence of test setup

needs to be taken account before measurement reliability and reproducibility can be reached. Test setups normally end up being very complicated; calibration and validation of the test system are difficult.

In this research, numerous efforts are done to improve the system dynamic range and to optimize the test configurations in order to take reliable measurements on the SAW resonators. Measurement challenges and test bench optimizations are discussed here:

A. System dynamic range

In large-signal measurements, system noise floor is defined as spurious level generated at the spectrum outside of the frequency of the input signal. The test dynamic range is defined as the ratio of maximum input power and the power of the noise floor. System noise floor depends on: a) the quality of the test equipments; b) signal qualities; c) the operation power level in the system; d) spectrum separation between the main tone and the spur. In the test setups such as the one shown in Fig. 4-7 and Fig. 4-8, creation of the measurement floor could be contributed from different test equipments such as the power amplifier, probe tips and the spectrum analyzer.

On the other hand, the second order and third order nonlinearity products by the SAW resonators are typically weak and are around -70dBc to -120dBc below the main power (power level depending on the measurement frequencies and resonator sizes). Therefore, in order to detect and measure these nonlinearity signals, the test dynamic range has to be better than 120dBc. By running multiple experiments, it is found that the keys to improve the system noise floor are:

a), choosing the high-linearity PAs and high dynamic range spectrum analyzers are required. By testing different PA models and spectrum analyzers one by one and comparing the dynamic range, best PA and spectrum analyzers are picked. It is found Amplifier Research's model 25S1G4A power amplifier and Rohde & Schwarz FSU spectrum analyzer provide sufficient dynamic range.

b), besides the high-linearity PA and spectrum analyzer, it is determined that a low pass filter (LPF) or a band pass filter(BPF) is needed at output of the PA so the power can be delivered to the DUT while intermodulation caused by PA output leakage can be attenuated; meanwhile, a high pass filter (HPF) or a band pass filter (BPF) is needed before the input of the spectrum analyzer so the output power from DUT can be attenuated to improve the measurement floor of the spectrum analyzer while harmonics and intermodulations can be passed through.

c), additionally, attenuators (ATT) are connected to the ports of the DUT. In the wafer probing measurements, the attenuators are connected next to the probe tips. The advantages of doing it are: 1) it could reduce the power reflection from the DUT and prevent the nonlinearity signal generation caused by mixing of reflected signals from the DUT with the PA; 2) it helps impedance matching for the DUT to improve the test reliability. Fig. 4-11 indicates the influence of the system noise floor with different attenuators next to the probe tips by plotting the IMD3 power of the 'through' structure. As shown, with increase of the attenuation from 3dB to 12dB, system noise floor improves by around 7dB.

d), also, system noise floor is sensitive to the different connector types at DUT and if wafer probes are used, it is sensitive to the grounding condition and shielding condition of the probe tips. It is found that the system noise floor is around 10 to 20dB better by using SMA

connectors with DUT on the PCB than using prober to test DUT on the wafer. Also, it is noticed that by switching the probe tips with different pitches or switching the probe tips from different vendors, the system noise floor level varies with the different probe structures. In the worst case, certain probe tips create stronger IMD2 and IMD3 than the passive SAW resonators do so nonlinearity products generated by SAW resonators could not be detected. Fig. 4-12 and Fig. 4-13 plot the 'through' responses of the both IMD2 and IMD3 tests using different types of connectors and different types of probe tips. It is obvious that probe tips deteriorate the noise floor of both IMD2 and IMD3 by at least 15dB, comparing to the noise floor using SMA connectors. Deterioration of the noise floor in IMD3 test is more severe. It is treated as the major drawback to run the large signal tests using wafer prober. However, by carefully optimizing the test system and using the high-linearity probe structures available, the noise floors of on-wafer IMD2 and IMD3 tests are around -115dBm and -100dBm respectively with input power of 25dBm and they are sufficient for IMD tests for resonators.

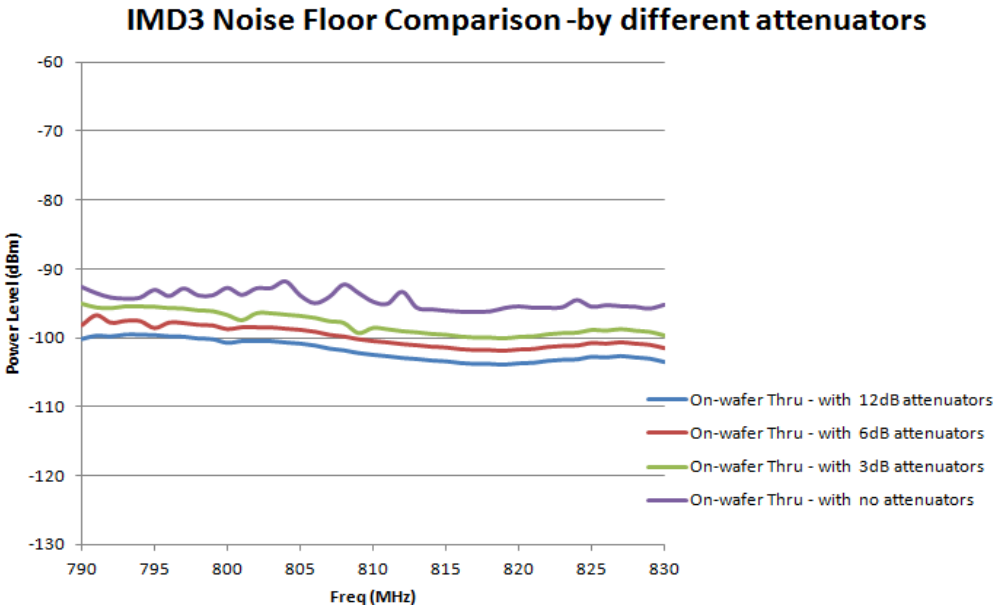

Figure 4-11 Noise floor comparison of an IMD3 test using different attenuators at the test ports. Tone 1 frequencies are used in the plot

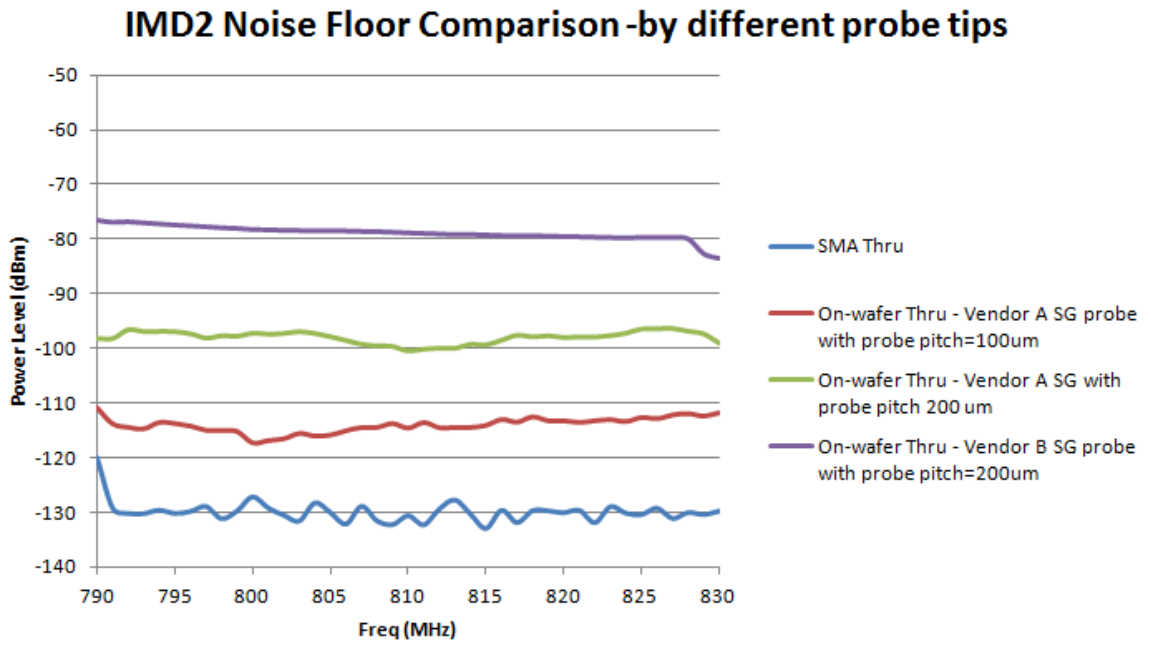

Figure 4-12 Noise floor comparison of an IMD2 test using different types of connectors and different types of probe tips; Tone 1 frequencies are used in the plot

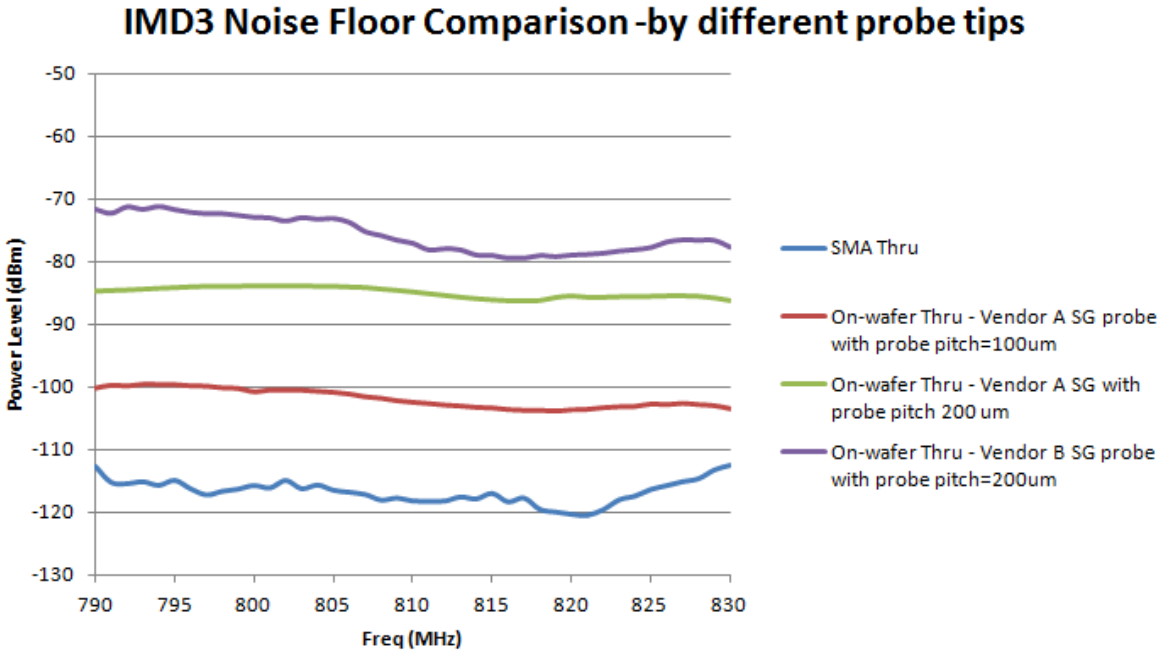

Figure 4-13 Noise floor comparison of an IMD3 test using different types of connectors and different types of probe tips; Tone 1 frequencies are used in the plot

B. Difficulties of 2-tone IMD measurements

Comparing IMD measurements to the harmonic measurements, system noise floors in IMD measurements are worse. In the case of harmonic measurements, the frequency separation between the second harmonic (H2)/ the third harmonic (H3) and the stimulus tone are large. Therefore, by properly using LPF and HPF in the system to provide suppression of large signal, the system dynamic range can be optimized to be as good as 150dBc; In the case of IMD measurements, frequency difference between input tone(s) and IMD product is designed to be only several MHz away. Although BPFs are used to separate the signals to improve the noise floor, attenuation provided by the BPFs is limited by the filter steepness. Therefore, the system noises floor is normally worse. Between IMD2 and IMD3 tests, system noise level of IMD2 is better than IMD3 due to the fact that jammer tone (Tone 2) frequency is far away from the main tone and IMD frequencies in the IMD2 test. Fig. 4-14 compares the system noise level in the harmonic and IMD measurements when the main tone (tone 1) powers are set to be 25dBm, tone 2 powers (in the IMD tests) are set to be 0dBm.

On the other hand, it is noticed that spurious power levels of IMD2 and IMD3 of SAW devices are weaker than their harmonic spurious signals. Therefore, with worse noise floor but weaker signals, detecting the IMD distortion is more difficult. Fig. 4-15 compares the power levels of H2, H3, IMD2 and IMD3 of the reference resonator when the main tone (tone 1) powers are set to be 25dBm, tone 2 powers (in the IMD tests) are set to be 0dBm.

There are a few ways to improve the IMD test bench: the test dynamic range can be improved by using the BPFs which have the steep pass-to-stop-band transition and excellent stopband rejection. The power level of IMD2/IMD3 of SAW resonators can be strengthened by testing the 2-port resonators in shunt (Fig. 4-8), instead of testing them in series (Fig. 4-7). As shown

in Fig. 4-16 and Fig 4-17, testing the shunt resonator creates stronger intermodulation products which helps the IMD signals to be detected. Especially in the case of IMD3 measurements, the power level of IMD3 is around -100dBm when the resonator is tested in series; the result is not reliable since it is below the system noise floor level.

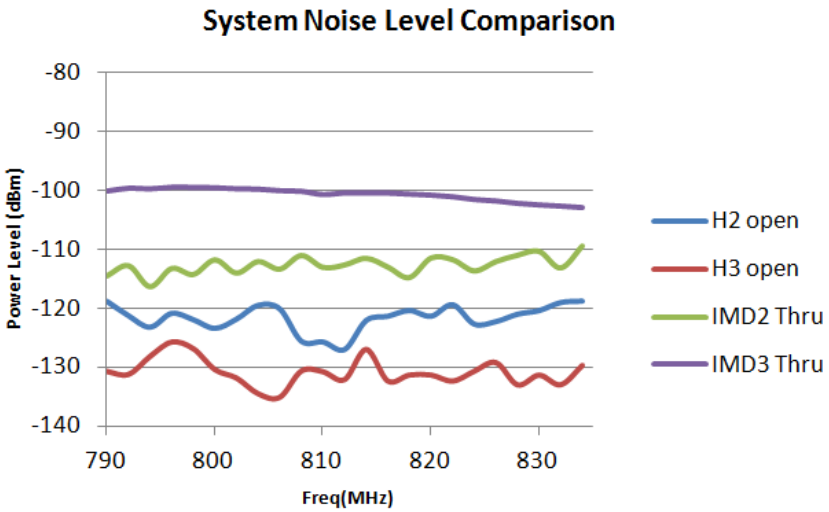

Figure 4-14 System noise level comparsion between harmonis measurements and intermodulation measurements; Tone 1 frequencies are used in the plot

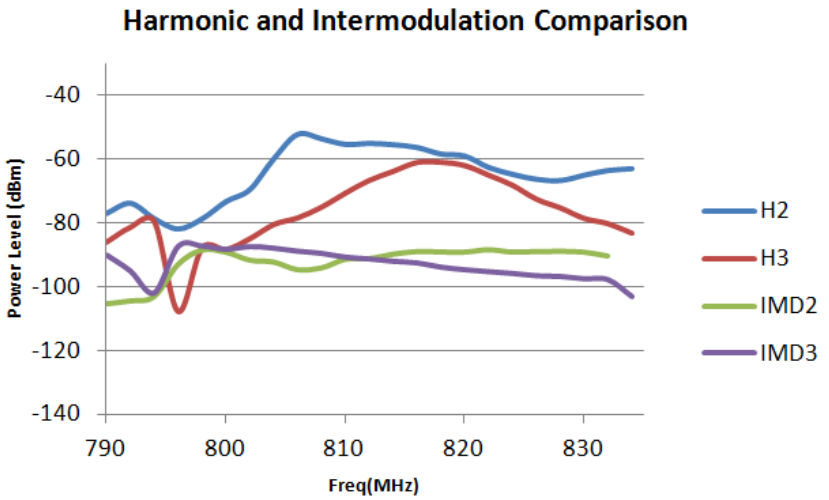

Figure 4-15 Harmonic and IMD power level comparsion of the reference resonator; Tone 1 frequencies are used in the plot

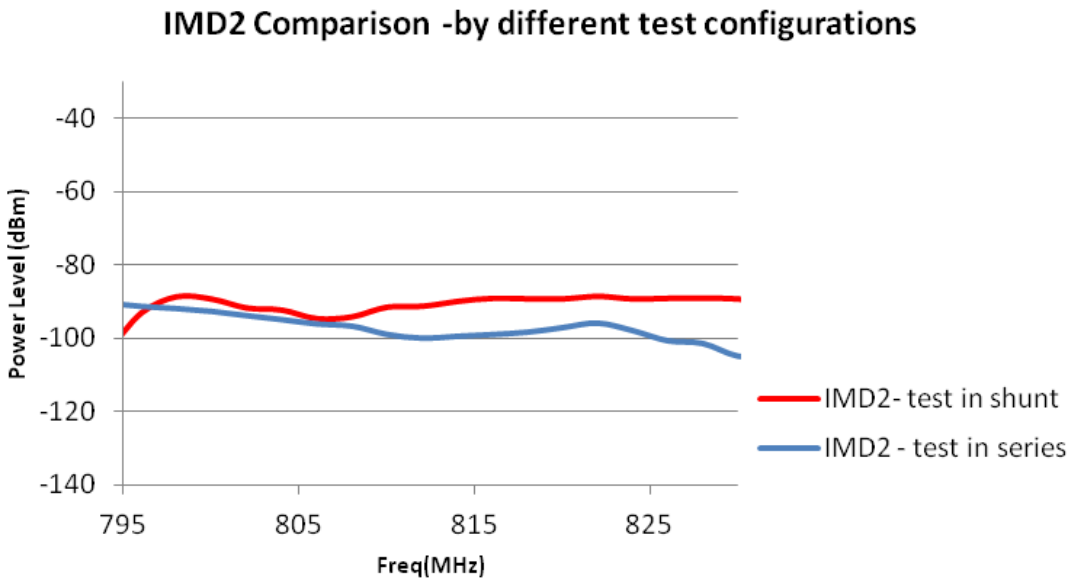

Figure 4-16 IMD2 measurement results of the reference resonator; the comparison is between testing the resonator in series and testing the resonator in shunt; Tone 1 frequencies are used in the plot

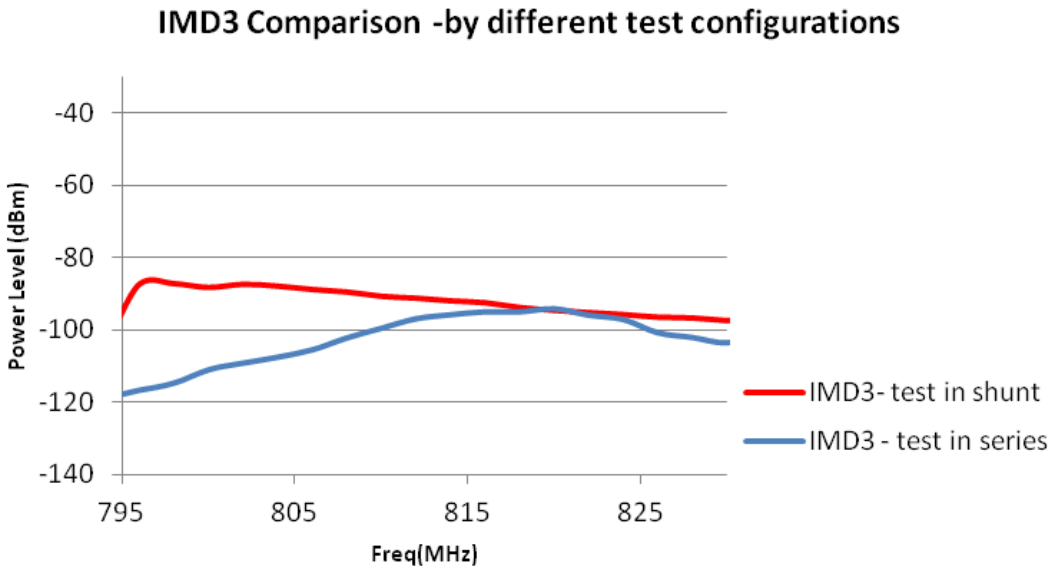

Figure 4-17 IMD3 measurement results of the reference resonator; the comparison is between testing the resonator in series and testing the resonator in shunt; Tone 1 frequencies are used in the plot

4.4 Nonlinearity Results of Test Resonators

After optimizing the test setups and measuring harmonics and IMDs of the reference resonator with success, the same test bench is used to test multiple resonators. Harmonic results are used to analyze the nonlinear characteristics of the different resonators with geometric, metal thickness and substrate orientation variations. Measurement results are plotted in this section.

4.4.1 Harmonic Measurement Results

Fig. 4-18 and Fig. 4-19 plot the 1-port H2 and H3 measurement results of the reference resonator; the reflected spectrum of harmonic power is plotted with input CW tone sweep from 750MHz to 850MHz at 25dBm; comparison with noise floor by ‘open’ structure is also shown. Since the system noise floors are well below the signals from the resonator, the results are counted as reliable.

4.4.2 IP2 and IP3

Second Order Interception Point (IP2) and Third Order Interception Point (IP3) [11] are the measures of linearity which qualify the distortion severity. IP2 is defined as the output power point at which the extrapolated first and second order output power lines intersect on a plot. IP3 is defined as the output power point at which the extrapolated first and third order output power lines intersect. IP2 and IP3 plots of harmonics of the reference resonator are shown in Fig. 4-20. In the tests, PA is set to amplify the input signal to 10dBm, 15dBm, 20dBm and 25dBm respectively to detect the change of harmonic power level; peak reflected power are

used to generate the IP2 and IP3 plots. As shown, H2 power increases twice faster and H3 power grows 3 times faster than the input power. IP2 is at 105 dBm and IP3 is at 70dBm.

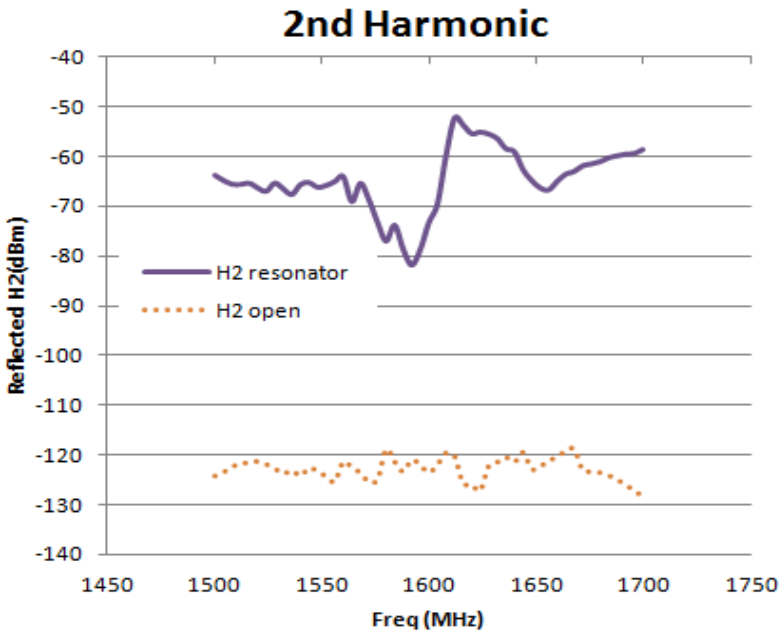

Figure 4-18 2nd order reflected spectrum of the reference resonator showinig harmonic power (H2) with comparison to noise floor at input power level of 25dBm; H2 frequencies are used in the plot.

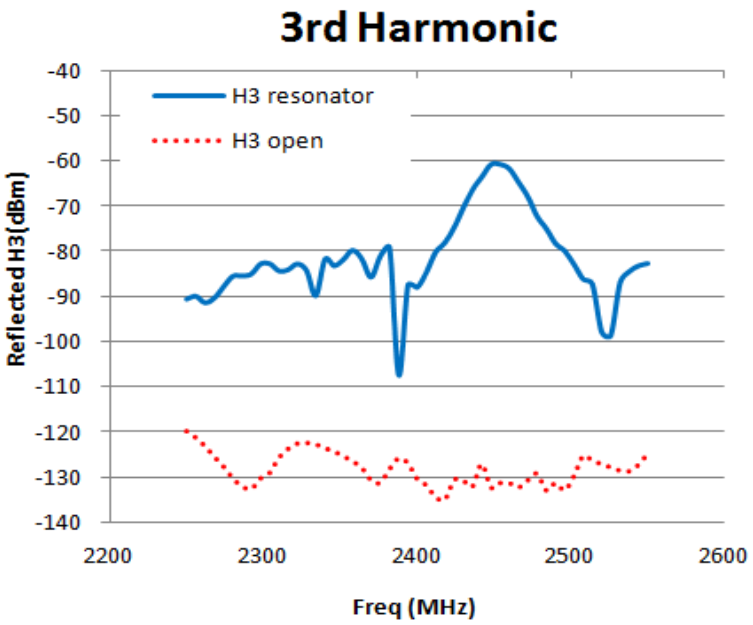

Figure 4-19 3rd order reflected spectrum of the reference resonator showing harmonic power (H3) with comparison to noise floor at input power level of 25dBm; H3 frequencies are used in the plot.

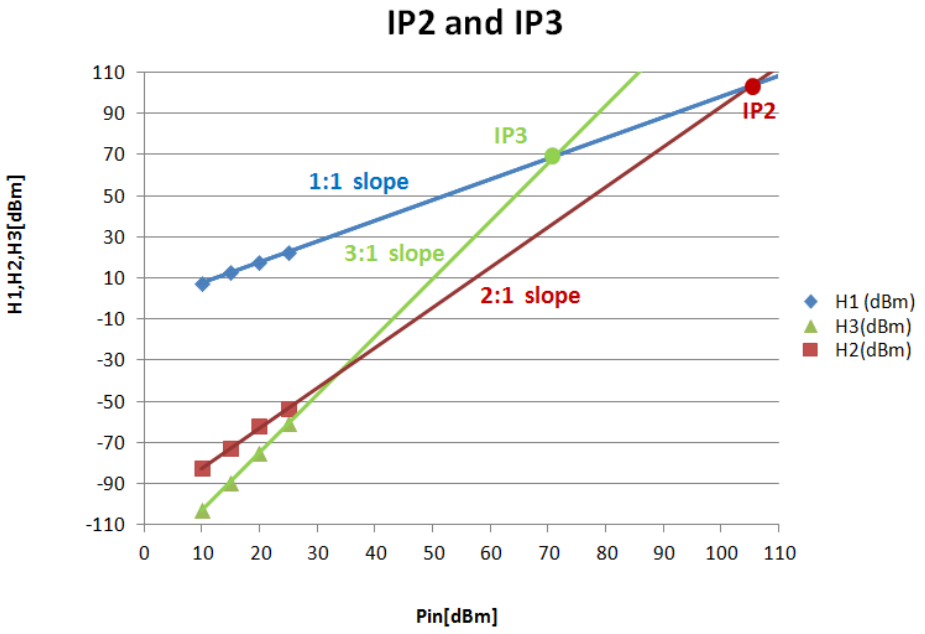

Figure 4-20 IP2 and IP3 plots of the reference resonator by peak reflected power of H1, H2 and H3 vs. input power

4.4.3 Harmonic Result Comparison among Different Resonators

After measuring H2 and H3 on different resonators, characterization of SAW nonlinear effects is done by analyzing the trends of both H2 and H3 with different design parameters. Input power is chosen to be at 25dBm for the following comparison. First of all, Fig. 4-21(a) and (b) show the peak reflected H2 and H3 by different resonator sizes (with variation of both resonator length and aperture). Duty factor of these resonators are 50%. As shown, harmonic power is lower when the resonator size goes bigger (with increase of either length or aperture) since power density on the resonator is lower; trend on H2 is more obvious than H3. Also on the same plots, it is shown that resonators fabricated on LT42 and LT48 wafers generate similar distortion level; therefore, nonlinearity of SAW device is not strongly dependant on the wafer cut angle of lithium tantalate substrate. Then, Fig. 4-22 (a) and (b) indicate the tendency of H2 and H3 peak power with variation of DF change (from 45% to 60%) on the reference resonator. It is noticed that H2 improves with increase of DF but H3 degrades with increase of DF on the electrodes. Further, Fig 4-23 (a) and (b) show the H2 and H3 plots with pitch variation of different resonators. Since pitch is defined by wavelength $p = \lambda/2$ and all the resonators are deposited with same metal thickness h, it is confirmed that nonlinear distortion of SAW device is not strongly dependant on h/λ change.

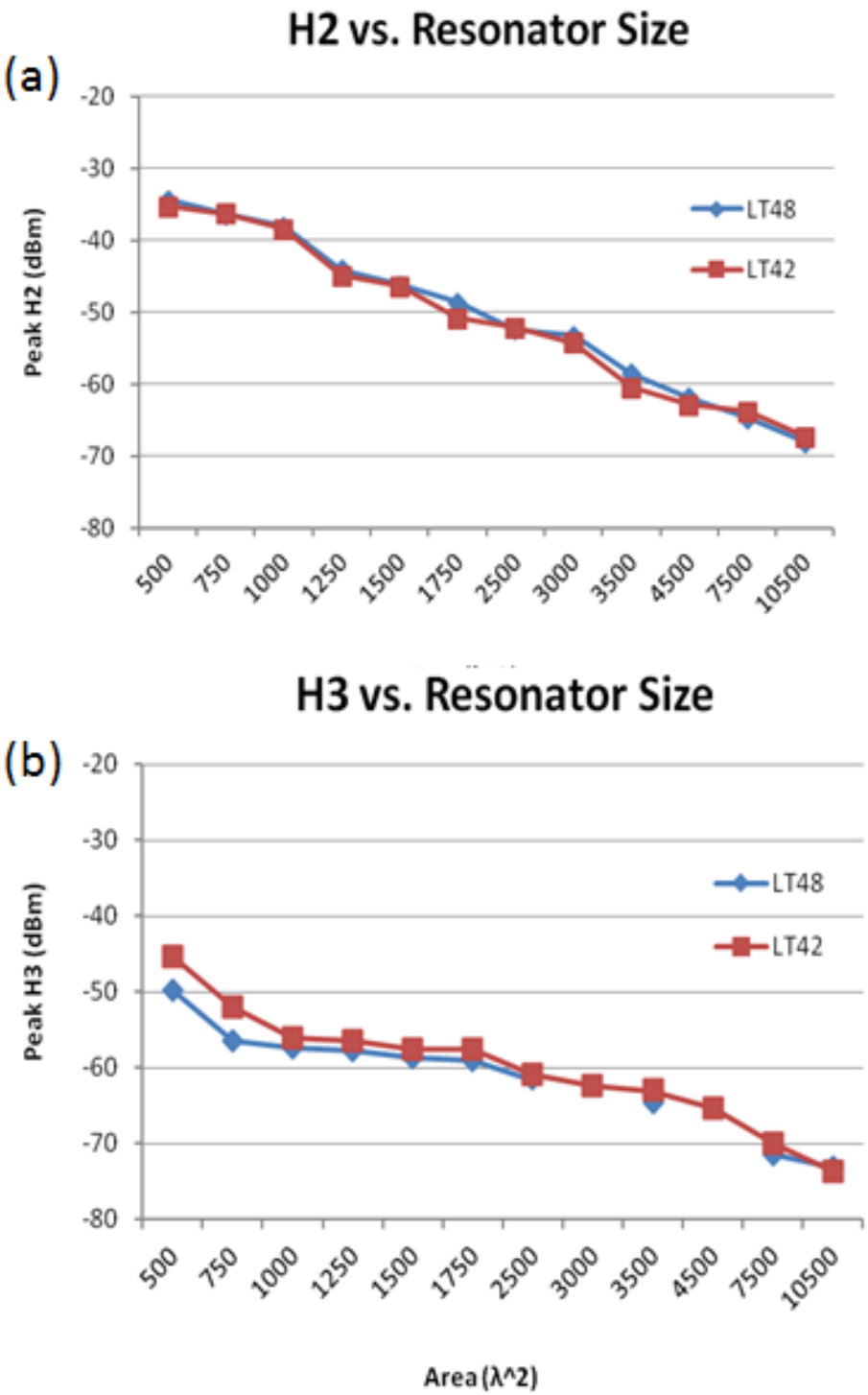

Figure 4-21 (a) Peak H2 vs. resonator size; (b) Peak H3 vs. resonator size

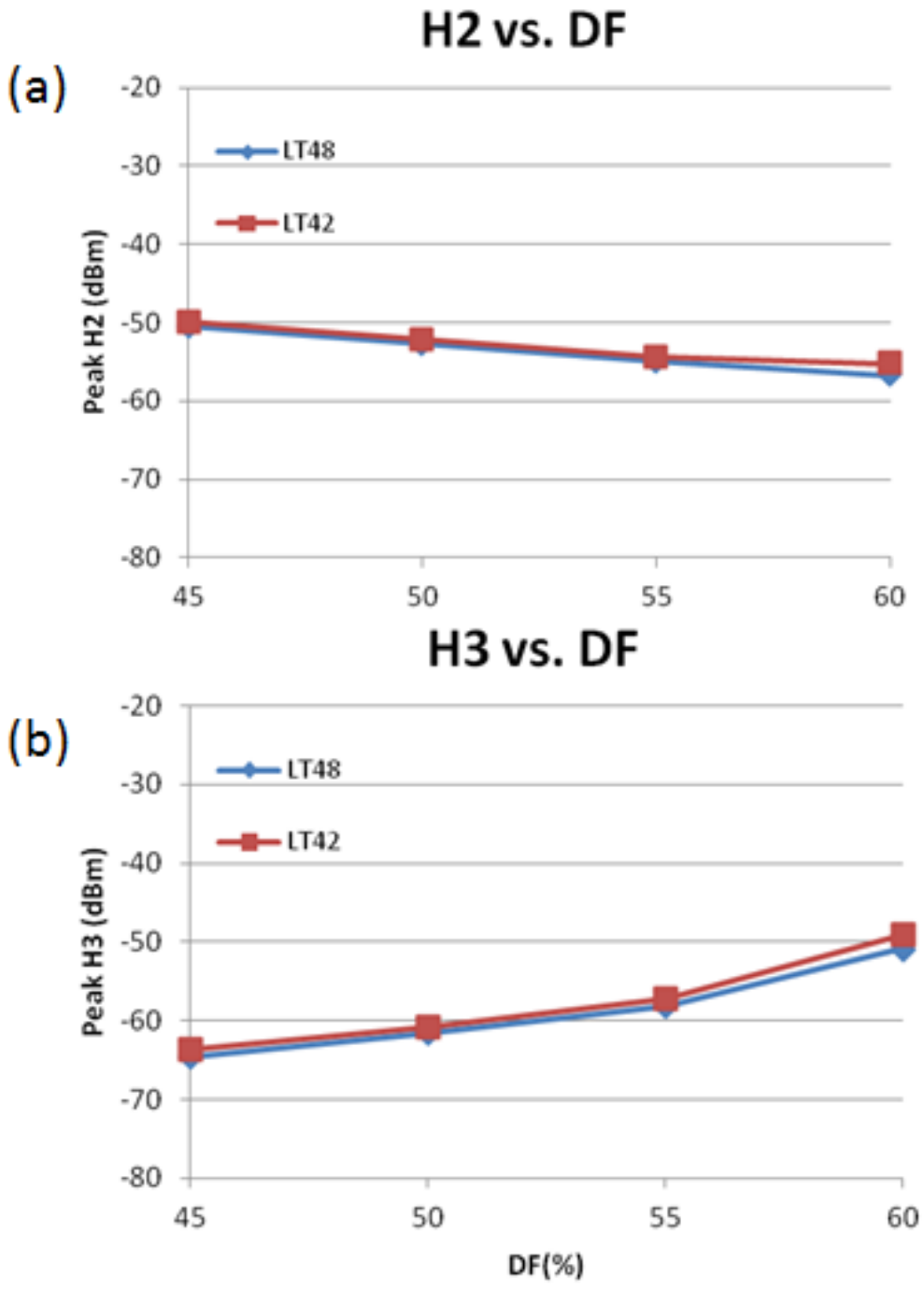

Figure 4-22 (a) Peak H2 vs. DF variation ; (b) Peak H3 vs. DF variation

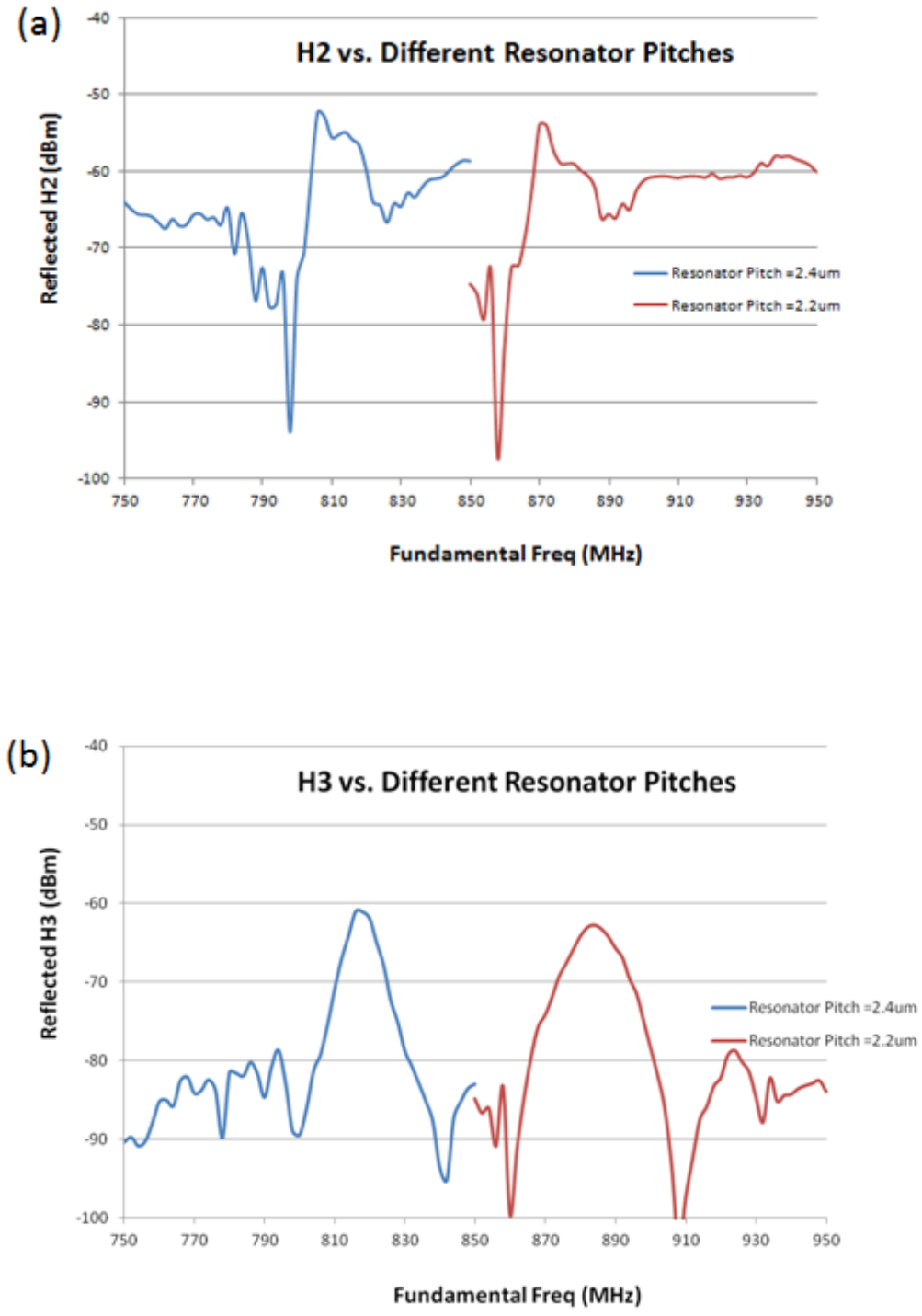

Figure 4-23 (a) Peak H2 vs.different resonator pitches; (b) Peak H3 vs. different resonator pitches; fundamental frequencies are used for the plots

4.4.4 Intermodulation Measurement Results

Intermodulation measurement setups have been explained in details in Section 4.3. Here, by using the test setup shown in Fig. 4.8, IMD2 and IMD3 results of the reference resonator are plotted in Fig. 4-24 and Fig. 4-25 with comparison to noise floor. Meanwhile, tone 1 power is swept from 10dBm to 25dBm so peak power of IMD2 and IMD3 products with tone 1 power sweep can be plotted in Fig 4-26. As indicated, IMD2 power grows at the same rate with Tone 1 power increase and IMD3 power grows twice faster than Tone 1 power.

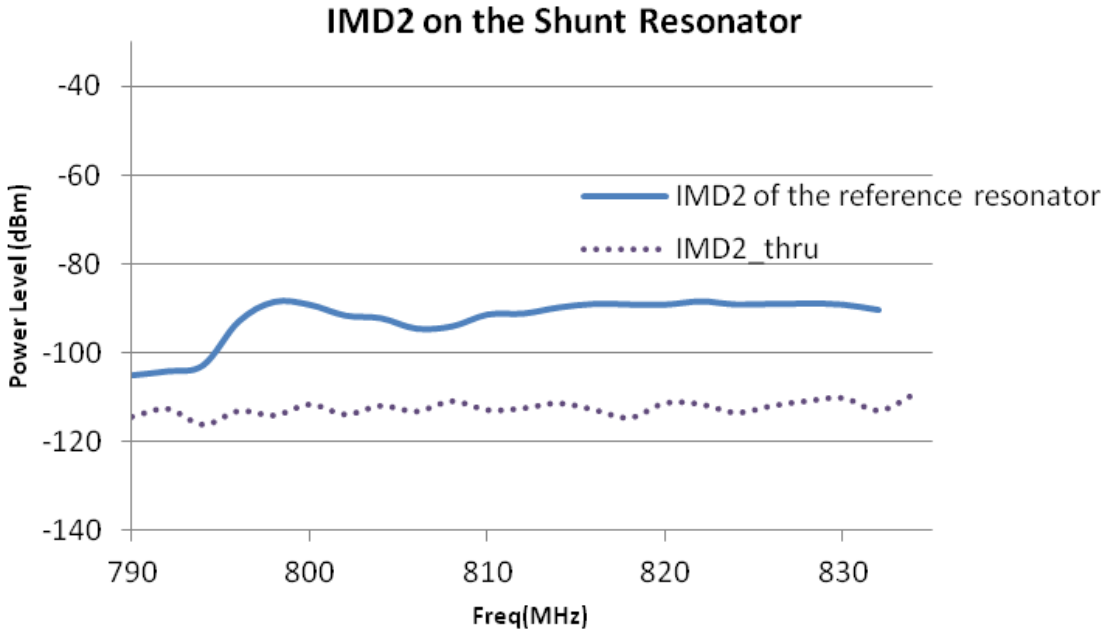

Figure 4-24 IMD2 intermodulation products of the reference resonator; Tone 1 frequencies are used in the plot

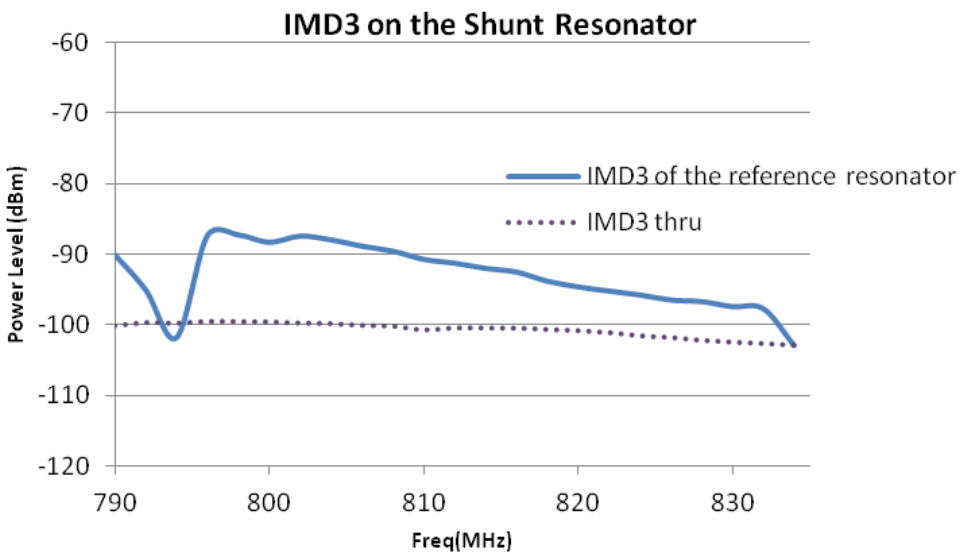

Figure 4-25 IMD3 intermodulation products of the reference resonator; Tone 1 frequencies are used in the plot

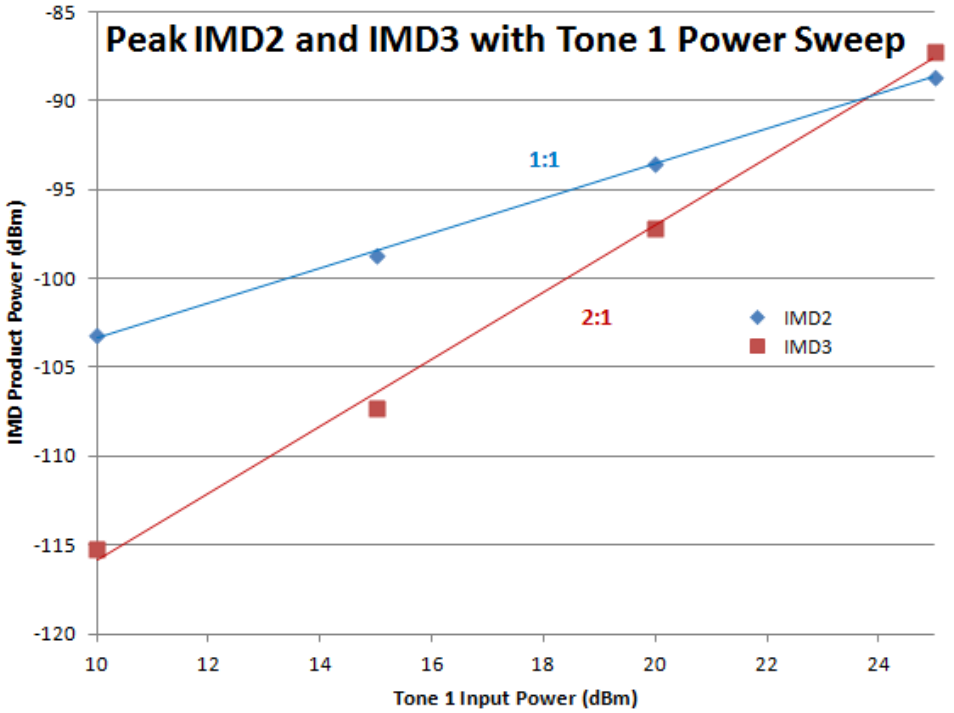

Figure 4-26 Peak IMD2 and IMD3 power vs. Tone 1 input power sweep of the reference resonator

4.5 Measurements of a Duplexer

Generally, in order to meet receiver sensitivity requirements, intermodulation distortion is specified for duplexers by 3GPP: IMD2, IMD3 measurements are among the most standard tests to measure the nonlinearity in Rx bands. In WCDMA/LTE systems, system specifications normally require IMD2 and IMD3 to be lower than -110 dBm in order not to desensitize the receiver.

In this Ph. D. research, a single/balanced WCDMA Band 5 duplexer (800MHz) is designed for analysis and model validation. Topology of the duplexer is plotted in Fig. 4-27. As explained, this typical duplexer is build with a network of resonators of different sizes and frequencies. The design of this Band 5 duplexer includes eight single-pole resonators (Tx1 to Tx8) for the Tx filter, three single-pole resonators (Rx1 to Rx3) and one 3-IDT coupled resonator filter for the Rx filter; 4 ports are used to terminate the duplexer impedance at antenna (ANT), Tx and balanced Rx ports (Rx and RxQ). Two inductors (L_ant and L_rx) are included for impedance matching for the ports. The duplexer is built into 2.0mm by 2.5mm package; S-parameter measurement is then taken and frequency response of the duplexer is plotted in Fig. 4-28.

For a WCDMA Band5 duplexer, list of IMD test conditions and specifications is summarized in Table 4-3. It should be noticed that in the IMD tests, the Tx (f1) power is calibrated at ANT port. In order to measure the intermodulation distortion according to the specifications, test benches for IMD2 and.IMD3 tests are developed. IMD2 and IMD3 test systems (Fig. 4-29) are similar to the ones used to test the resonators; except that the duplexers are packaged and mounted on the PCB so SMA connectors are used, instead of wafer probing. In the system, SG1 is the signal generator for Tx (f1) tone; SG2 of signal generator of the jammer

tone. The jammer tone level is set at -15dBm for both IMD2 and IMD3 tests: In the case of IMD2 test, SG2 generates a signal at 45MHz; RF switch 1 and RF switch 2 are both switched on for the IMD2 filter to pass the signal at 45MHz; in the case of IMD3 test, SG2 generates a signal from 779 MHz to 804 MHz (at 45MHz lower than f_1) and RF switch 1 and RF switch 2 are then switched on for the IMD3 filter so signals between 779 MHz and 804 MHz could be passed. This IMD test bench for duplexers performs successfully by providing test noise floor around -140dBm while IMD2 and IMD3 products from duplexers at around -125dBm to -110dBm. The measurement results are shown in Fig. 4-30.

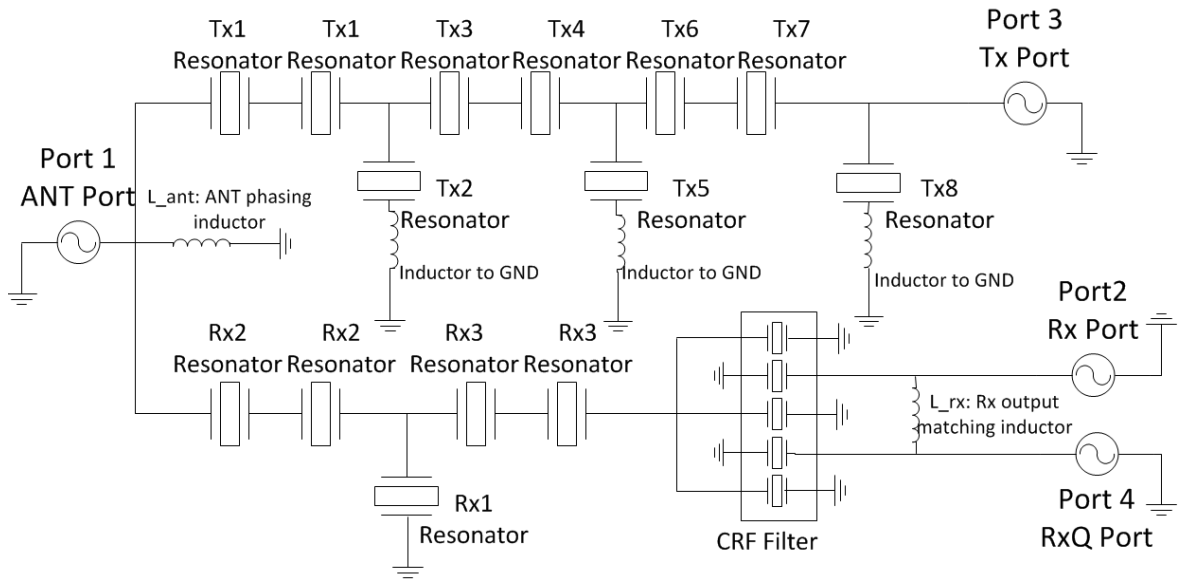

Figure 4-27 Topology of a single/balanced WCDMA Band 5 duplexer

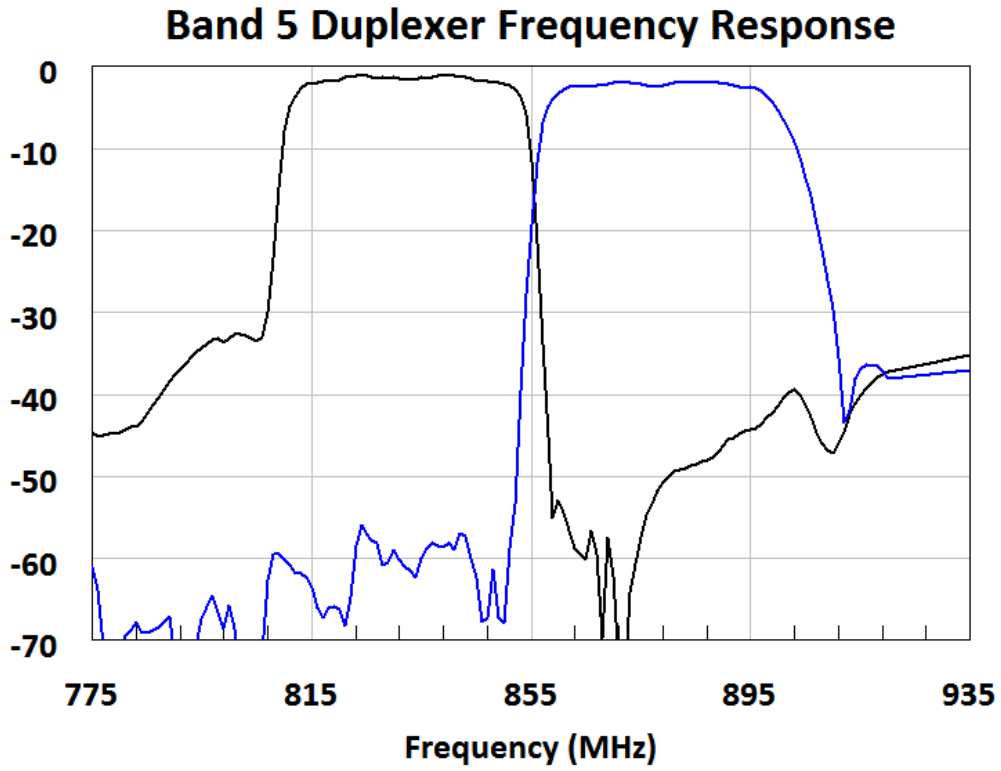

Figure 4-28 Measurement of a WCDMA Band 5 duplexer; response of the Rx filter (ANT to Rx port) is plotted in blue; reponse of the Tx filter (Tx to ANT port) is plotted in black

Table 4-3 IMD test configurations for a WCDMA Band 5 duplexer

		Sweep Freq (MHz)		Power (dBm)
IMD2 measurement	Tx (f1)	824	849	21.5
	Jammer (f2)	45	45	-15
	IMD2 (f1+f2)	849	894	To be measured
IMD3 measurement	Tx (f1)	824	849	21.5
	Tone2 (f2)	779	804	-15
	IMD3 (2f1-f2)	869	894	To be measured

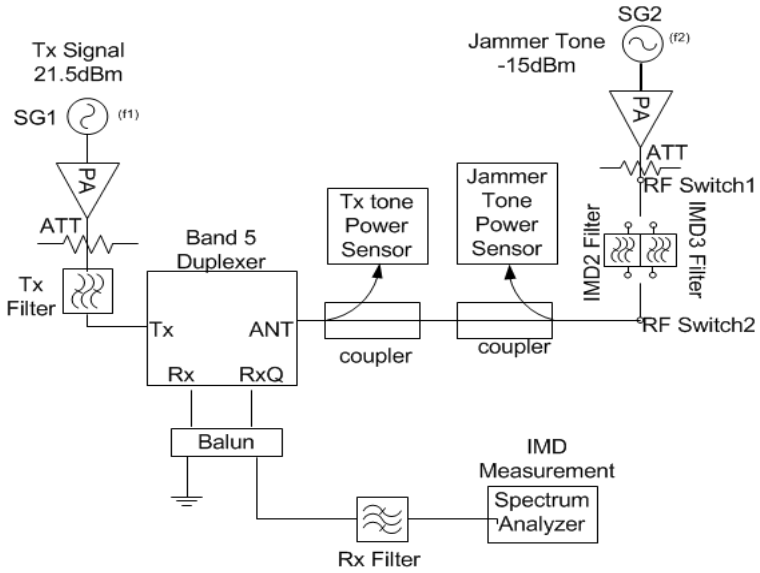

Figure 4-29 IMD3 measurement setup diagram of a Band 5 duplexer

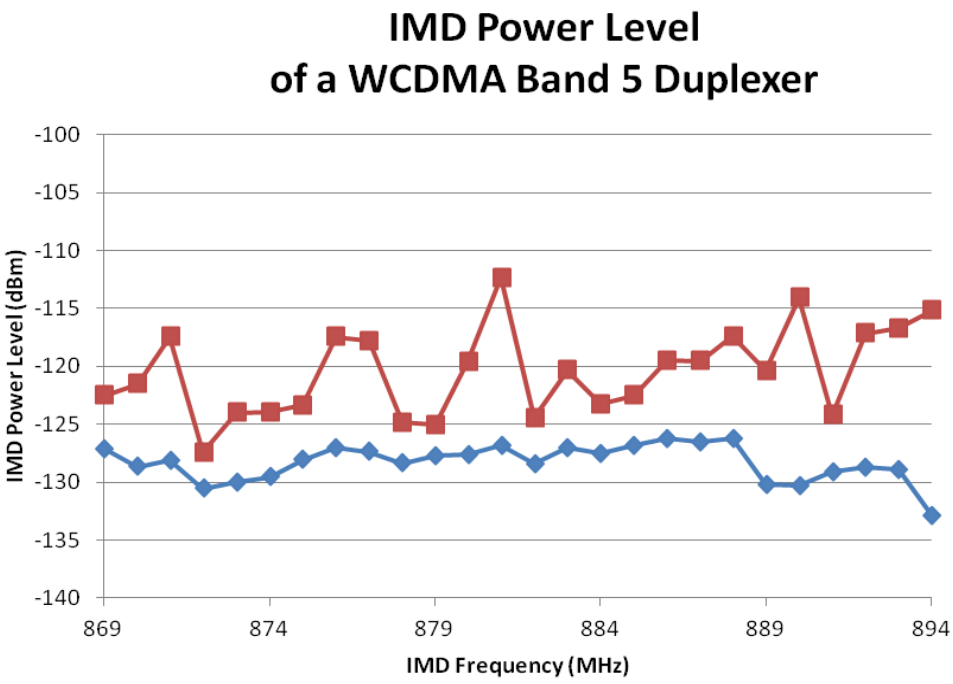

Figure 4-30 IMD measurement plot of a WCDMA Band 5 duplexer; IMD2 response is plotted in blue and IMD3 response is plotted in red

CHAPTER 5: VALIDATION OF THE MODEL

5.1 Simulation Overview

In this chapter, validation of the nonlinear Mason circuit model is done by simulating the harmonic and IMD distortions of SAW resonators and a Band 5 duplexer in a commercial circuit simulator and confirming the agreements between the simulation and measurement results. Agilent's Advanced Design System (ADS) is used for simulations. Inside ADS, harmonic balance (HB), a nonlinear current-voltage based simulator, is used to simulate the nonlinear responses of the circuit, while S-parameter based small signal simulations are done by the same circuit.

In order to describe the simulation work, this chapter is organized as follows: harmonic balance simulator is briefly discussed in Section 5.2; the ADS simulation flow is explained in Section 5.3; In Section 5.4, determination of the 3^{rd} order nonlinear coefficient in the Mason circuit is done by fitting the IMD3 simulation result to the measurements; simulation results of the resonator are also shown in the same section; then in Section 5.5, IMD3 simulation setup of a Band 5 duplexer is shown, simulation and measurement results are compared; finally, advantages of the nonlinear Mason model and future plans are discussed in Section 5.6.

5.2 Harmonic Balance Simulator

Harmonic balance is a highly accurate frequency-domain analysis method used to calculate the steady-state response of nonlinear circuit equations. The harmonic balance method assumes that the input stimulus includes a few steady-state sinusoids. Therefore, the solution

is a sum of steady state sinusoids, which consists of the input frequencies in additions to the harmonics and mixing terms. A detailed introduction of harmonic balance simulator in ADS can be found in [49].

To explain, a single input source in the circuit requires a single tone harmonic balance simulation with a solution waveform as follow:

$$v(t) = \mathrm{Re}\left\{\sum_{k=0}^{K} V_k e^{j2\pi kft}\right\} \tag{5.1}$$

where f is the fundamental frequency of the source, V_k is the complex Fourier coefficient which harmonic balance simulator computers, and K is the number of harmonics included in the simulation; similarly, a circuit with multiple input sources requires a multi-tone simulation. The steady state solution waveforms for the multi-tone signals are approximated as:

$$v(t) = \mathrm{Re}\left\{\sum_{k_1=0}^{K_1}\sum_{k_2=0}^{K_2}\cdots\sum_{k_n=0}^{K_n} V_{k_1,k_2,\ldots k_n} e^{j2\pi(k_1 f_1 + k_2 f_2 + \ldots + k_n f_n)t}\right\} \tag{5.2}$$

where n is the number of the tones, $f_{1\ldots n}$ are the fundamental frequencies of each sources, $K_{1\ldots n}$ are the numbers of harmonics. Then the truncated Fourier series representation of the equation transforms the N nonlinear differential equations into a system of $N \times M$ algebraic equations in the frequency domain; M is the total number of frequencies from each tone. The equations are governed by Kirchhoff's Current Law (KCL) in the frequency domain: at each node, the sum of current (linear and nonlinear) entering the node must equal to the sum of current leaving the node. Therefore, the solver of the harmonic balance simulator in ADS calculates the amount by which the Kirchhoff's Current Law is violated from an initial guess

of the coefficients and then uses multiple iterations successively to reduce the violation to a small value and finally reaches the convergence to find the values of the coefficients.

5.3 Simulation Flow in ADS

Simulation flow for SAW resonators and duplexers using nonlinear Mason circuits can be described by the following flow chart (Fig. 5-1). As shown, three simulation stages are defined to simulate the harmonic and intermodulation responses of a SAW resonator: in step 1, the schematic of an unit nonlinear Mason circuit of one electrode section is created in ADS, design parameters of the resonator are defined in the schematic; grating sections and transducer section are built up by cascading multiple unit circuits together. Then, the simulation schematic of a full resonator is created by assembling the simulation blocks of grating and transducer sections in series and the harmonic balance simulator is set up in the resonator circuit. In step 2, the 3^{rd} order nonlinear coefficient is determined by fitting the resonator intermodulation simulation to the measurement result. By running multiple intermodulation and harmonic simulations on different resonators, the nonlinear coefficient is confirmed to be only depended on types of piezoelectric materials. In step 3, the duplexer simulation is done by setting up different resonator schematics, running the EM simulation to include EM parasitic, defining electrical connections of the duplexers and setting up simulator configurations for the excitation tones. The single 3^{rd} order nonlinear coefficient extracted in step 2 is used to simulate accurately the nonlinear distortion of the duplexer.

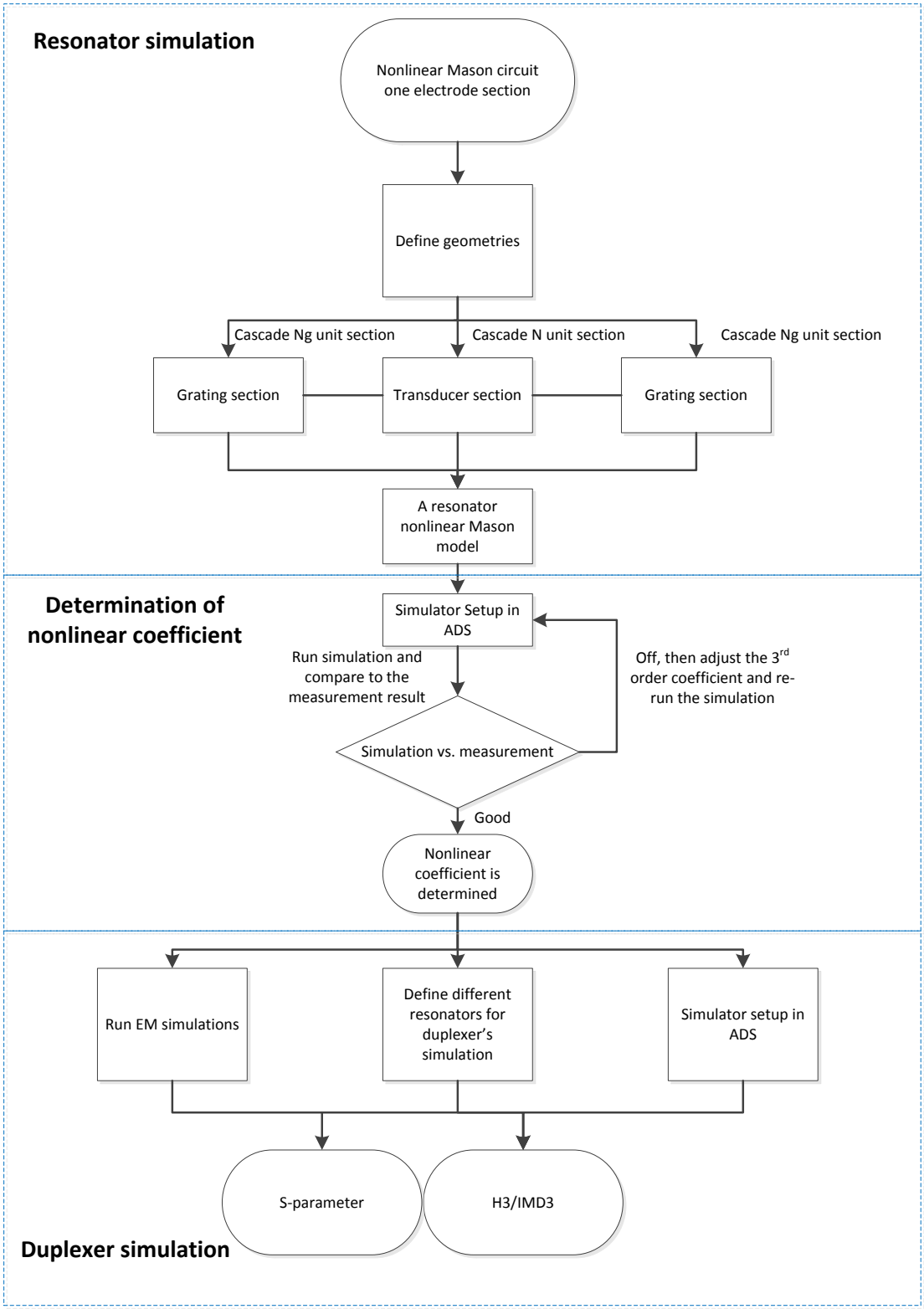

Figure 5-1 Duplexer simulation using the nonlinear Mason circuit in ADS

5.4 Determination of the Nonlinear Coefficient and Simulation Results

To simulate a resonator, the nonlinear unit Mason circuit of one electrode section (Fig. 3-10) is generated first in ADS (Fig. 5-2). As indicated, a transmission line for one electrode section is split into substrate-electrode-substrate sections to simulate metallization ratio (DF) of the electrodes, represented by TL1, TL2 and TL3 respectively in the circuit. Port 1 and port 2 are the acoustic ports assigned at the sides of the transmission line; port 3 and port 4 are defined as the electrical ports. In the circuit, the nonlinear term is modeled by C3, a nonlinear voltage dependant capacitor placed between the acoustic transmission section and the transformer; inside this nonlinear capacitor and a 3rd order coefficient is defined. Additionally, TF1 is the transformer and C1, C2 are the static capacitors. Inputs to TL1, TL2, TL3, C1, C2 and TF1 are calculated based on the substrate properties and the geometry of the resonator.

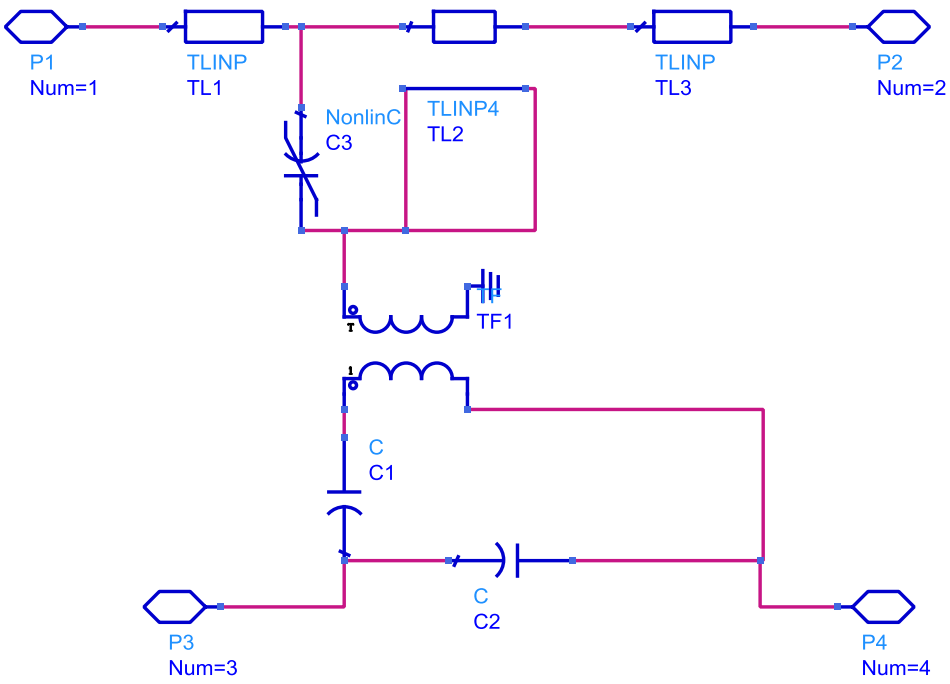

Figure. 5-2 The ADS schematic of a nonlinear unit Mason circuit of one electrode section

Furthermore, a transducer with N electrodes can be formed by cascading N unit circuits together by their port 1 and port 2 and connecting their electrical ports 3 in parallel. Adjacent electrodes are assigned with opposite electrical polarities. To demonstrate, the schematic of a 50-electrode transducer is shown in Fig. 5-3. Each block of the 4-port sub-circuit represents a unit Mason model of one electrode.

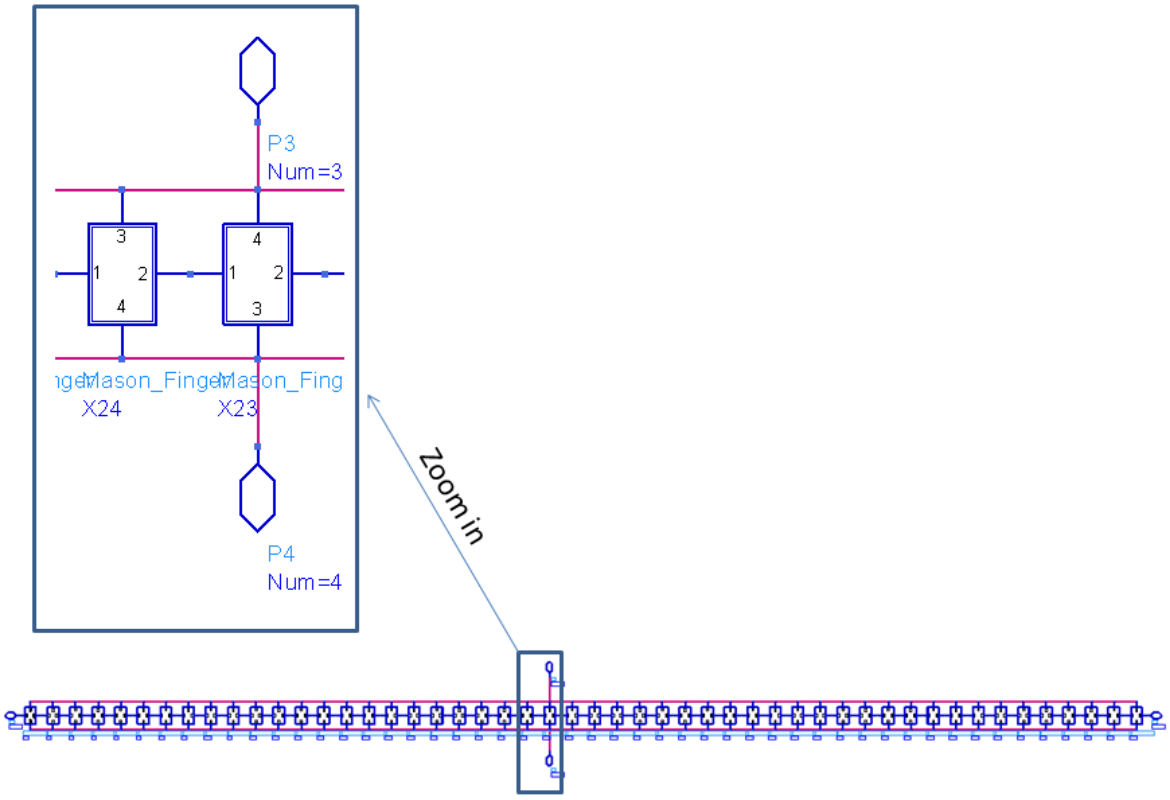

Figure 5-3 The ADS schematic of a transducer section with 50 electrodes. Each individual block is a 4-port sub-circuit of unit Mason model of one electrode. Zoom-in view of two electrodes is also shown. Two consecutive unit cells are connectted with opposite polarities to represent the alternate polarities of consecutive electrodes.

Similarly, a grating circuit with $N_g = 15$ electrodes is shown in Fig. 5-4. Comparing to the transducer circuit, port 3 and port 4 are left open in the grating circuit.

Finally, a resonator circuit is formed by connecting transducer and grating sections together. Fig. 5-5 shows the circuit of simulating a 2-port resonator. As shown, transducer and gratings are cascaded and gratings are terminated with two resistors with $R1$ and $R2$. The resistance of $R1$ and $R2$ is chosen to be the acoustic characteristic impedance to represent the free surface substrate outside of the gratings.

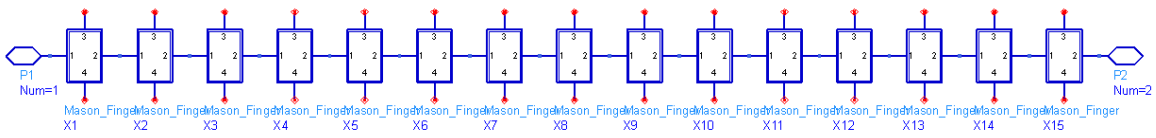

Figure 5-4 The ADS schematic of a grating section with 15 electrodes. Each individual block is a sub-circuit of unit Mason model of one electrode.

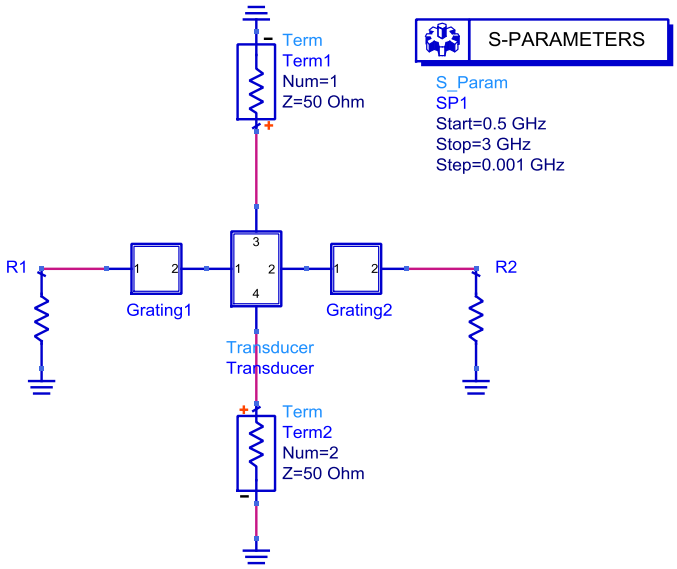

Figure 5-5 Schematic setup of the S-parameter simulation of a 2-port resonator in ADS

To demonstrate the simulation results, a test resonator with pitch of 2.35um, DF of 50%, length of 200 wavelengths (400 electrodes) and the aperture of 10 wavelengths is chosen. Fig. 5-6 shows the simulation and measurement results of the admittance response of the resonator. As shown, fs of the resonator is around 830MHz and fp is around 855MHz.

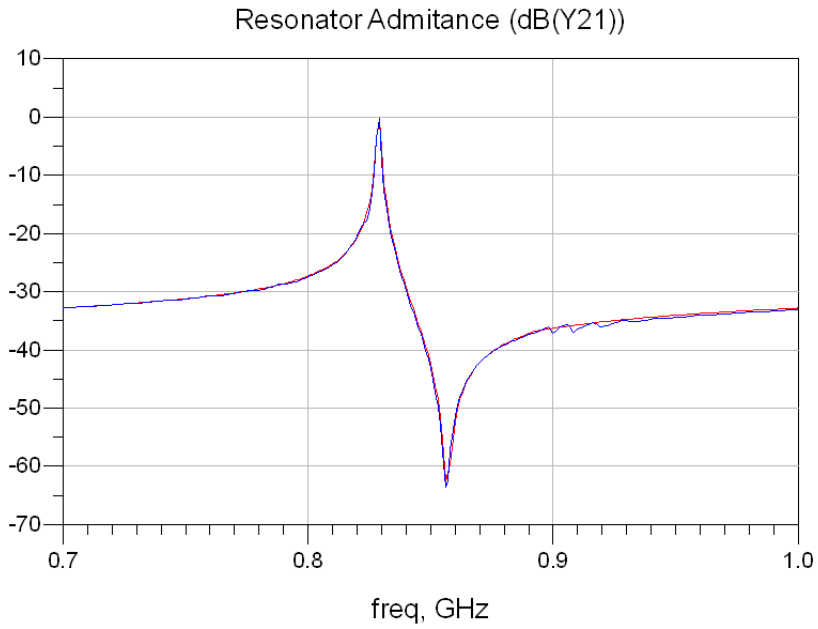

Figure 5-6 Mason model simulation (in blue) vs.measurement (in red) of admitance of the resonator with 200 λ length and 10 λ aperture

The nonlinearity simulation of this resonator is done by using power source ports to excite the resonator. The harmonic balance simulator is used. Fig. 5-7 shows the schematic setup used to simulate the 2-tone IMD3 on the shunt resonator with length of 200 wavelengths and the aperture of 10 wavelengths. In the simulations, value of the 3rd order nonlinear coefficient cc_2 in the nonlinear capacitor C_{NL} is tuned. By tuning cc_2 value, IMD3 power level raises with increased value of cc_2 and drops with decreased value of cc_2 (Fig. 5-8). Finally, by

fitting the simulation to the measurement, the normalized nonlinear coefficient cc_2 is determined to be 1.05e-9 for LT42 substrate. This parameter is unitless.

Fig. 5-9 shows the simulation and measurement results of the IMD3 of the test resonator. As shown, the simulation shows decent agreement with the measurement. By running more simulations on the different resonators, it is confirmed that the value of the 3rd order nonlinear coefficient is independent on resonator geometry parameters such as aperture, length or DF. Beside the 2-tone intermodulation simulation, the 3rd order harmonics of the resonator is also simulated by the setup shown in Fig. 5-10. Simulation and measurement results are plotted against each other in Fig. 5-11. By simulating the resonator, the nonlinear Mason model is proved to be capable of simulating resonator impedance and multi-tone nonlinear distortion such as harmonics and intermodulations accurately. Results also confirm that the 3rd order nonlinearity in the propagation, represented by a single coefficient, is a good assumption.

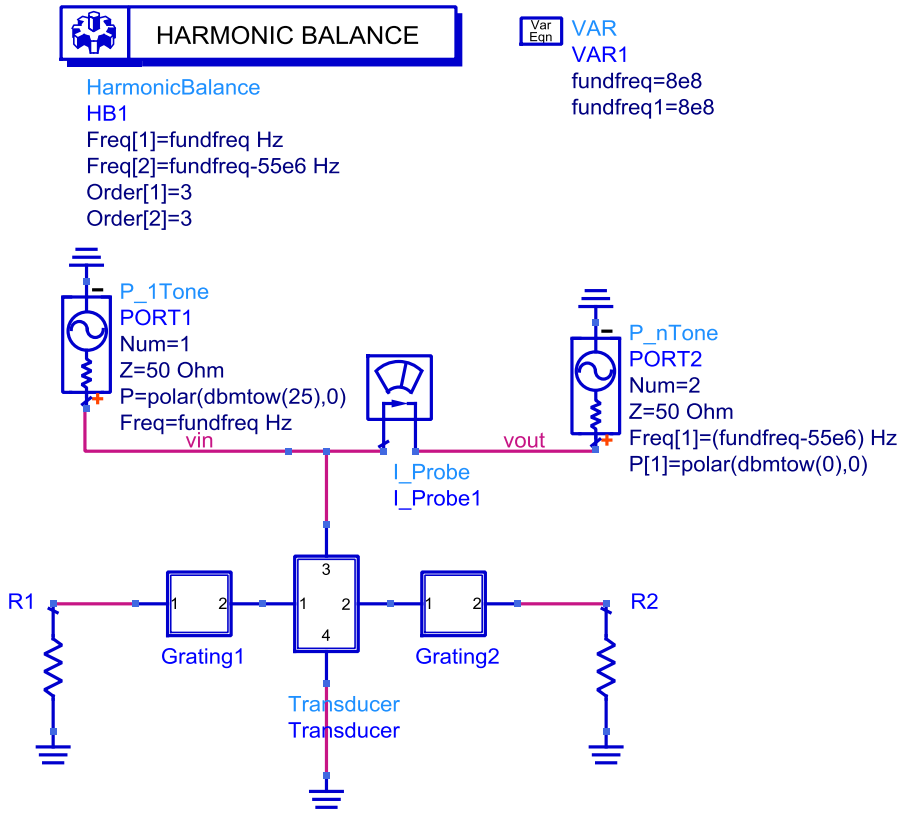

Figure 5-7 Schematic setup of IMD3 simulation on a shunt resonator in ADS

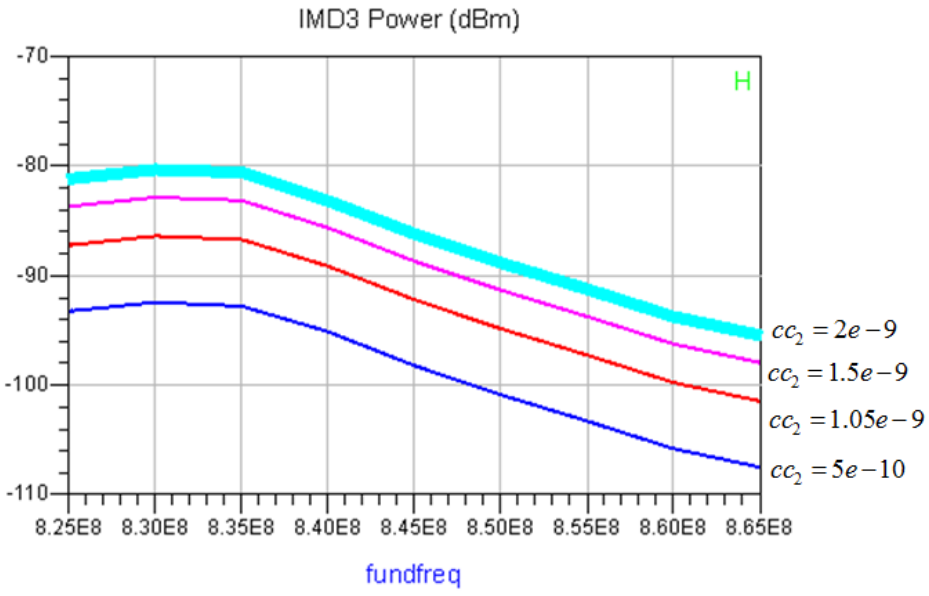

Figure 5-8 IMD3 power level with tunning value of cc_2

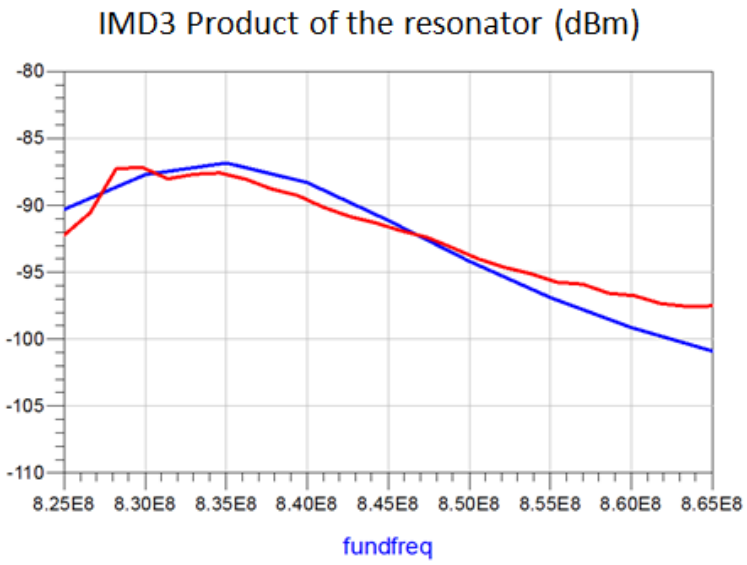

Figure 5-9 Simulation (Blue) and measurement (Red) results of the IMD3; tone 1 frequency is used in the plot

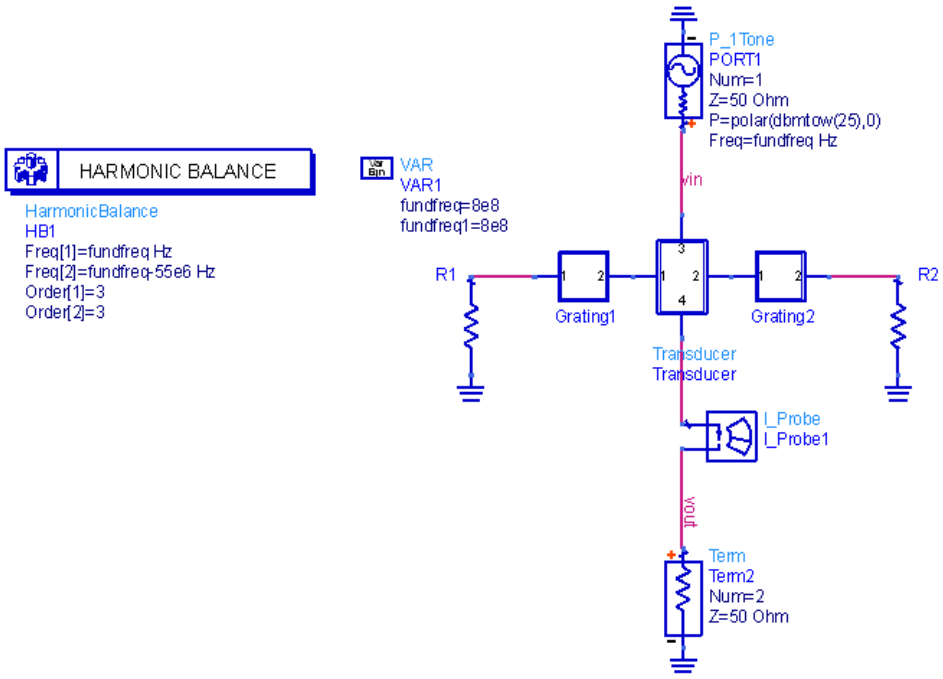

Figure 5-10 Schematic setup of 2-port harmonic simulation on a resonator

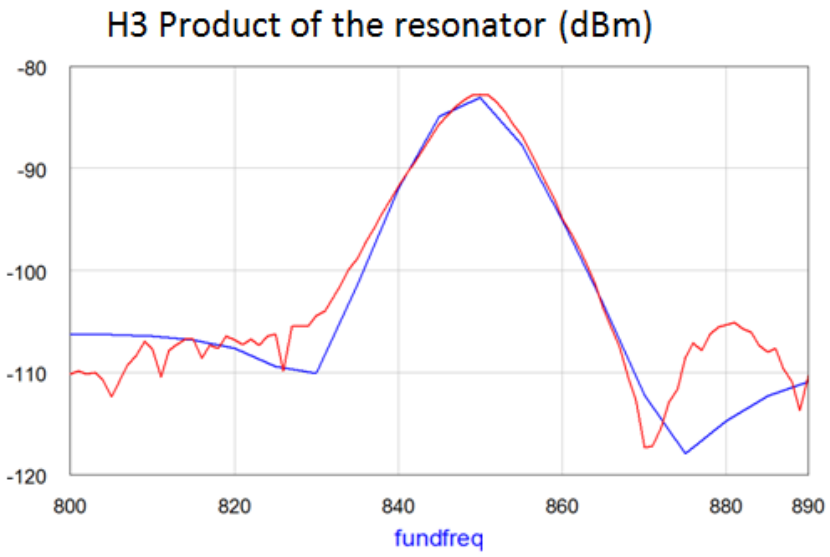

Figure 5-11 Simulation (Blue) and measurement (Red) results of the 3rd harmonic product; fundemental tone frequency is used in the plot

5.5 Nonlinear Simulations of a WCDMA Band 5 Duplexers

After demonstrating that the nonlinear Mason model is capable of simulating the nonlinear behavior of resonators and extracting the direct 3rd order nonlinear coefficient from the intermodulation results, the next step is to use the model to simulate the full duplexers. In this section, a single/balanced WCDMA Band 5 duplexer (850MHz) is demonstrated as an example. Both small signal S-parameter simulation and large signal IMD3 results are presented.

First of all, topology of this duplexer is plotted in Fig. 4-27. Based on the topology and design parameters, ADS schematic of the same duplexer is shown in Fig. 5-12. Besides the resonator simulations, die and package EM parasitic effects are taken account by including

the EM simulation done using the finite element done using the finite element electromagnetic simulator HFSS from Ansys [50]

Figure 5-12 Schematic of a WCDMA Band 5 duplexer simulation in ADS.

To confirm the validity of the nonlinear Mason model for simulating both S-parameter and nonlinearity responses, all the single-pole resonators in the duplexer are simulated individually before the complete duplexer simulation. Other SAW models help to benchmark the results: The COM model is used for small signal S-parameter simulation comparison and the nonlinear p-matrix model is used for large signal intermodulation simulation comparison. Mason model simulation results of admittance (Y11) and IMD3 of each resonator are plotted in Fig. 5-13. Outcome of the comparison with other modeling tools indicates that the new Mason model provides equivalent results as what the COM model and the nonlinear p-matrix model deliver.

Next, by using the circuit shown in Fig. 5-12, the duplexer's small signal frequency response can be simulated and the result is plotted against the measurement. Fig. 5-14 shows simulation versus measurement of duplexer's pass band response (by plotting S-parameter); further, by using the simulation schematic shown in Fig. 5-15, IMD3 simulation is completed and comparison to the measurement is shown in Fig. 5-16. Measurement was taken by using the test setup shown in Fig. 4-29 with Tx tone frequency sweeping from 824MHz to 849MHz and jammer tone frequency to be 45MHz below the Tx tone. Overall, good simulation correspondence with the measurement is obtained. The nonlinear Mason model is proven to be a useful tool for SAW design engineers to predict both the small signal and large signal behavior of the duplexers.

5.6 Discussion and Future Simulation Works

After simulating multiple resonators and duplexers using the nonlinear Mason model and comparing the simulation process with other tools, it is noticed that the nonlinear Mason model provides the following advantages over other simulation tools:

Computation speed –by using a main-stream personal computer, the computation time to accomplish a duplexer S-parameter simulation using the new Mason model is within seconds. A 2-tone IMD simulation could be finished within 5 minutes. Such speed provides duplexer designers the flexibility to use the model not only to predict the nonlinear behavior, but also to optimize the linearity performance of the duplexers.

Flexibility – the Mason model is capable to simulate both the S-parameters and nonlinear spurious products of duplexers using the same circuit, this is a big advantage over other

mathematically based models. Also, the new model is easy to be built and simulated by using the circuit simulator; the nonlinear coefficient is independent to resonators' geometries.

Based on these advantages, future efforts to extend the power of the nonlinear Mason model include: 1) to simulate the coupled resonator filter (CRF) using the nonlinear Mason model. The model of the electrode acoustic reflectivity needs to be improved to make simulation successful; 2) to integrate the nonlinear Mason model for SAW duplexers with other nonlinear transistor based models for active RF devices, such as power amplifiers, LNA and switches, for co-simulations. Simulation integration of the full RF front end with considerations of nonlinearity distortion could generate huge value to future RF system designs.

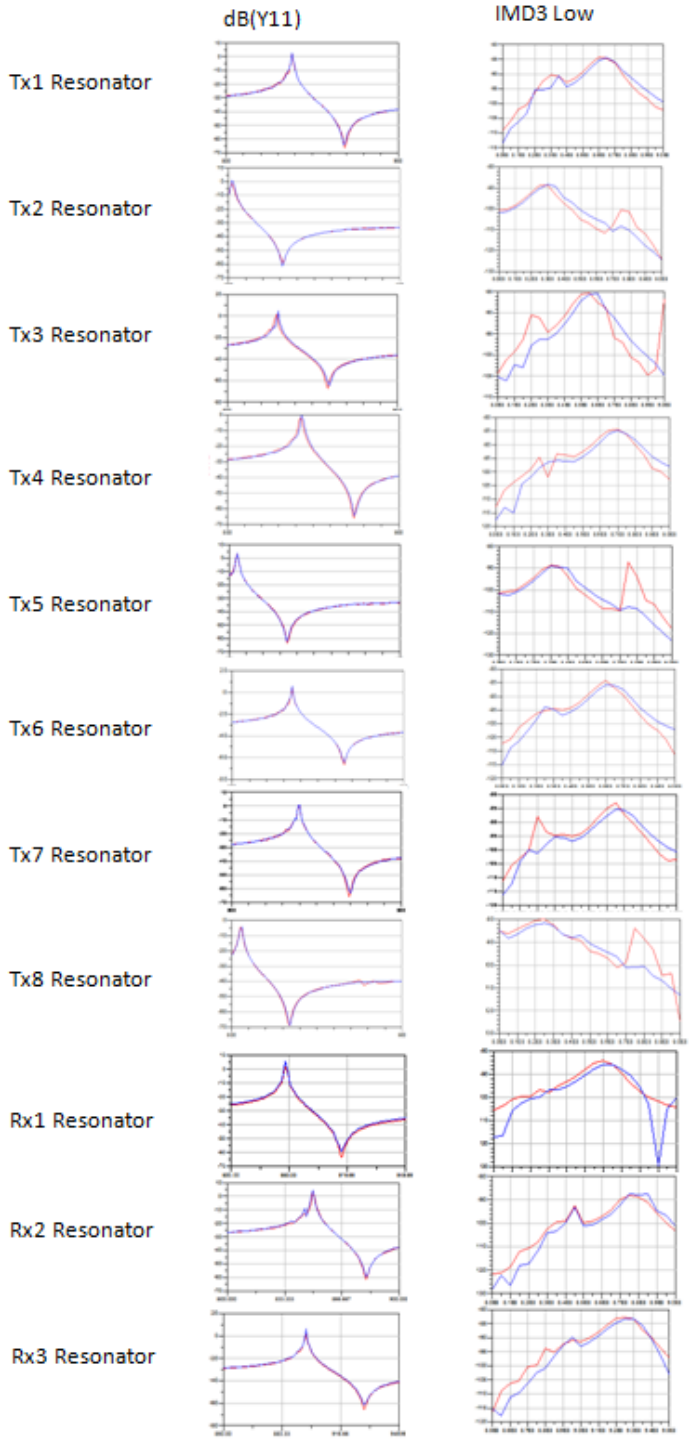

Figure 5-13 Mason model simulations of admittance and IMD3 of the different resonators (in blue) vs. COM model simulations of admittance (in red) of the same resonators and nonlnear p-matrix simulation of IMD3 (in red) of the same resonators

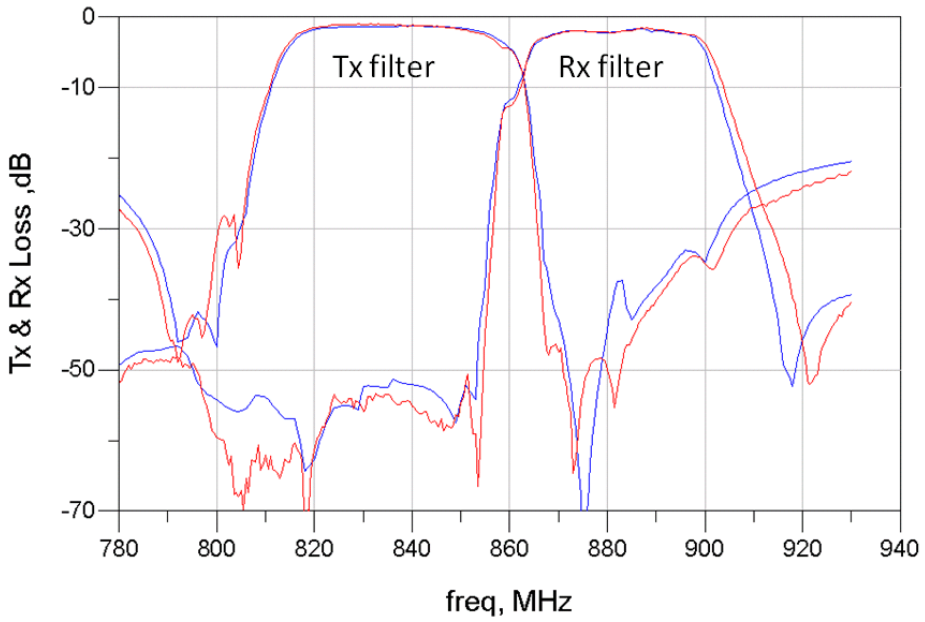

Figure 5-14 Mason model simulation (in blue) vs.measurement (in red) of the passband response of a Band 5 duplexer

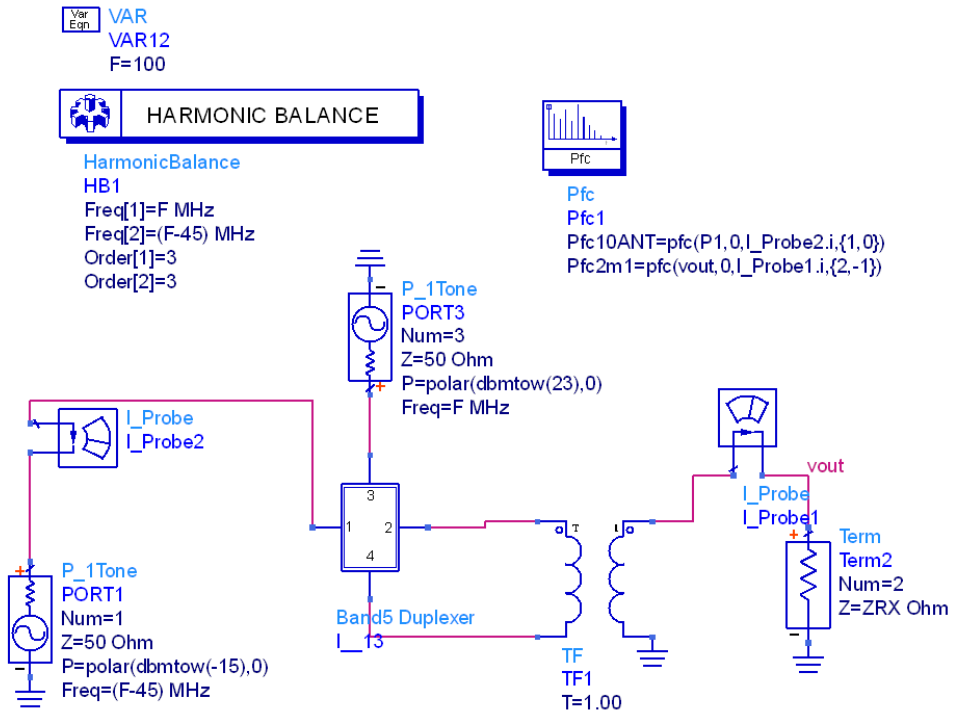

Figure 5-15 Schematic setup of the IMD3 simulation for a Band 5 duplexer in ADS

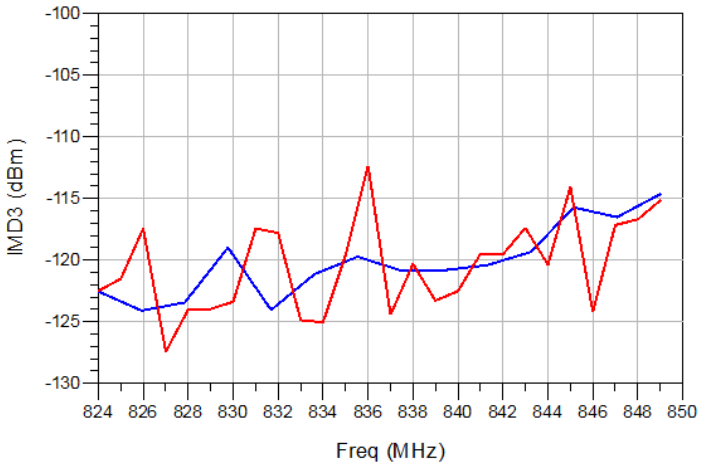

Figure 5-16 Mason model simulation (in blue) vs.measurement (in red) of a Band 5 duplxer's IMD3; Tx tone frequency is used in the plot

CHAPTER 6: CONCLUSION

In this Ph.D. research, nonlinear distortion of SAW resonators and duplexers has been investigated; a novel nonlinear Mason model to accurately simulate the harmonics and intermodulations of the SAW resonators and duplexers is proposed.

As the most important part of this thesis, this dissertation presents a new modeling approach to simulate the 3rd order spurious distortion of SAW resonators and duplexers. Starting from a one dimensional piezoelectric constitutive wave equations including a 3rd order nonlinear coefficient in the propagation, a nonlinear Mason equivalent circuit model for SAW is derived. The unit cell for the model is a one electrode section. Transducers and resonators are simulated by cascading several unit cells. The model is directly compatible with standard harmonic balance simulators inside the commercial circuit simulation softwares.

By comparing simulation and measurement results, validity of the model is demonstrated. The model has been proven to be an effective tool to predict the harmonic and intermodulation performance for duplexer products. Also, a single physical parameter is used as the nonlinear coefficient in this Mason model. It is independent of the geometry of the devices and was obtained by fitting the simulations to the measurements. In addition, it has been confirmed that a single physical parameter representing the 3rd order nonlinear elasticity is a good choice to simulate the overall 3rd order nonlinearity of SAW devices.

Besides the nonlinearity modeling, this research investigates the nonlinear distortion behaviors of the SAW devices by proposing large signal measurement methods to measure the harmonics and intermodulations over the spectrum. Influence of the measurement setup is considered. Characterization of the nonlinear distortion is demonstrated by both plotting the harmonic and intermodulation responses of resonators and duplexers over the frequencies and

comparing the trend of distortion with different properties of the resonators. The thorough analysis has provided useful design guidelines for designing high linear duplexers for WCDMA and LTE applications. Also, the test system developed is recognized as a ‘standard’ large signal measurement system to measure harmonics and intermodulations with reliability and reproducibility.

Overall, this research work developed several effective test approaches to measure the nonlinearities, provided the thorough analysis on nonlinear characteristics of SAW resonators and brought a novel nonlinear SAW model which provides fast and accurate simulations. The new model is also ideally suited for co-simulations of SAW duplexers with other RF active devices, due to its easy implementation in commercial circuit simulators.

REFERENCES

[1] R. M. White and F. W. Voltmer, "DIRECT PIEZOELECTRIC COUPLING TO SURFACE ELASTIC WAVES," *Applied Physics Letters,* vol. 7, pp. 314-316, 1965.

[2] P. S. Cross and R. V. Schmidt, "Coupled Surface-AcousticWave Resonators," *The Bell System Technical Journal,* vol. 56, p. 36, 1977.

[3] W. J. Tanski, "Multipole SAW Resonator Filters: Elements of Design and Fabrication," in *1981 Ultrasonics Symposium,* 1981, pp. 100-104.

[4] T. F. O'Shea and R. C. Rosenfeld, "SAW Resonator Filters with Optimized Transducer Rejection," in *1981 Ultrasonics Symposium,* 1981, pp. 105-110.

[5] T. Morita, Y. Watanabe, M. Tanaka, and Y. Nakazawa, "Wideband low loss double mode SAW filters," in *Ultrasonics Symposium, IEEE,* 1992, pp. 95-104 vol.1.

[6] J. Meltaus, "Loss Reduction in Coupled Resonance Surface Acoustic Wave Filters Operating at GHz Frequencies," Helsinki University, Department of Engineering Physics and Mathematics, Helsinki University of Technology, 2006.

[7] R. Ruby, P. Bradley, J. D. Larson, III, and Y. Oshmyansky, "PCS 1900 MHz duplexer using thin film bulk acoustic resonators (FBARs)," *Electronics Letters,* vol. 35, pp. 794-795, 1999.

[8] K.-y. Hashimoto, *RF bulk acoustic wave filters for communications*. Boston: Artech House, 2009.

[9] R. Aigner, "SAW and BAW technologies for RF filter applications: A review of the relative strengths and weaknesses," in *Ultrasonics Symposium, IEEE,* 2008, pp. 582-589.

[10] M. Ueda, M. Iwaki, T. Nishihara, Y. Satoh, and K. y. Hashimoto, "Investigation on nonlinear distortion of acoustic devices for radio-frequency applications and its supression," in *2009 IEEE Ultrasonics Symposium*, 2009, pp. 876-879.

[11] C. Liu and M. Damgaard, "IP2 and IP3 Nonlinearity Specifications for 3G/WCDMA Receivers," *High Frequency Electronics*, vol. June, p. 16, 2009.

[12] H. Pretl, L. Maurer, W. Schelmbauer, R. Weigel, B. Adler, and J. Fenk, "Linearity considerations of W-CDMA front-ends for UMTS," in *Microwave Symposium Digest. 2000 IEEE MTT-S International*, 2000, pp. 433-436 vol.1.

[13] T. Ranta, J. Ella, and H. Pohjonen, "Antenna switch linearity requirements for GSM/WCDMA mobile phone front-ends," in *Wireless Technology, 2005. The European Conference on*, 2005, pp. 23-26.

[14] N. Swanberg, J. Phelps, and M. Recouly, "WCDMA cross modulation effects and implications for receiver linearity requirements," in *Radio and Wireless Conference, 2002. RAWCON 2002. IEEE*, 2002, pp. 13-18.

[15] C. Campbell, *Surface Acoustic Wave Devices for Mobile and Wireless Communications*: Academic Press, 1998.

[16] K. Y. Hashimoto, *Surface Acoustic Wave Devices in Telecommunications: Modelling and Simulation*: Springer, 2000.

[17] D. Royer and E. Dieulesaint, *Elastic waves in solids II*. New York: Springer, 2000.

[18] R. H. Tancrell and M. G. Holland, "Acoustic surface wave filters," *Proceedings of the IEEE*, vol. 59, pp. 393-409, 1971.

[19] F. Z. Bi and B. P. Barber, "11E-0 Improve MBVD Model to Consider Frequency Dependent Loss for BAW Filter Design," in *Ultrasonics Symposium, 2007. IEEE*, 2007, pp. 1025-1028.

[20] W. R. Smith, H. M. Gerard, J. H. Collins, T. M. Reeder, and H. J. Shaw, "Analysis of Interdigital Surface Wave Transducers by Use of an Equivalent Circuit Model," *Microwave Theory and Techniques, IEEE Transactions on*, vol. 17, pp. 856-864, 1969.

[21] W. P. Mason and R. N. Thurston, *Physical acoustics: principles and methods*: Academic Press, 1981.

[22] M. Redwood, "Transient Performance of a Piezoelectric Transducer," *The Journal of the Acoustical Society of America*, vol. 33, pp. 527-536, 1961.

[23] G. Tobolka, "Mixed Matrix Representation of SAW Transducers," *Sonics and Ultrasonics, IEEE Transactions on*, vol. 26, pp. 426-427, 1979.

[24] P. Ventura, J. M. Hode, J. Desbois, and H. Solal, "Combined FEM and Green's function analysis of periodic SAW structure, application to the calculation of reflection and scattering parameters," *Ultrasonics, Ferroelectrics and Frequency Control, IEEE Transactions on*, vol. 48, pp. 1259-1274, 2001.

[25] B. A. Auld, *Acoustic fields and waves in solids*: R.E. Krieger, 1990.

[26] D. P. Morgan, "Reflective array modelling for SAW transducers," in *Ultrasonics Symposium, 1995. Proceedings., 1995 IEEE*, 1995, pp. 215-220 vol.1.

[27] J. R. Pierce, "Coupling of Modes of Propagation," *Journal of Applied Physics*, vol. 25, pp. 179-183, 1954.

[28] Y. Suzuki, H. Shimizu, M. Takeuchi, K. Nakamura, and A. Yamada, "Some Studies on SAW Resonators and Multiple-Mode Filters," in *1976 Ultrasonics Symposium*, 1976, pp. 297-302.

[29] H. A. Haus, "Modes in SAW grating resonators," *Journal of Applied Physics*, vol. 48, pp. 4955-4961, 1977.

[30] P. V. Wright, "A new generalized modeling of SAW transducers and gratings," in *Frequency Control, 1989., Proceedings of the 43rd Annual Symposium on*, 1989, pp. 596-605.

[31] B. P. Abbott, C. S. Hartmann, and D. C. Malocha, "A coupling-of-modes analysis of chirped transducers containing reflective electrode geometries," in *Ultrasonics Symposium, 1989. Proceedings., IEEE 1989*, 1989, pp. 129-134 vol.1.

[32] P. Ventura, J. M. Hode, M. Solal, J. Desbois, and J. Ribbe, "Numerical methods for SAW propagation characterization," in *Ultrasonics Symposium, 1998. Proceedings., 1998 IEEE*, 1998, pp. 175-186 vol.1.

[33] M. Solal, L. Chen, and J. Gratier, "Measurement and FEM/BEM simulation of transverse effects in SAW resonators in lithium tantalate," in *Ultrasonics Symposium (IUS), 2010 IEEE*, 2010, pp. 175-180.

[34] E. L. Adler, E. Bridoux, G. Coussot, and E. Dieulesaint, "Harmonic Generation of Acoustic Surface Waves in Bi 12 GeO 20 and LiNbO 3," *Sonics and Ultrasonics, IEEE Transactions on*, vol. 20, pp. 13-16, 1973.

[35] E. L. Adler and A. A. Nassar, "Effect of Dispersion on Harmonic Generation of Acoustic Surface Waves," in *1973 Ultrasonics Symposium*, 1973, pp. 268-270.

[36] D. A. Feld and D. S. Shim, "Determination of the nonlinear physical constants in a piezoelectric AlN film," in *2010 IEEE Ultrasonics Symposium (IUS)*, 2010, pp. 277-282.

[37] D. S. Shim and D. A. Feld, "A general nonlinear Mason model of arbitrary nonlinearities in a piezoelectric film," in *2010 IEEE Ultrasonics Symposium (IUS)*, 2010, pp. 295-300.

[38] C. Collado, E. Rocas, J. Mateu, A. Padilla, and J. M. O'Callaghan, "Nonlinear Distributed Model for Bulk Acoustic Wave Resonators," *Microwave Theory and Techniques, IEEE Transactions on*, vol. 57, pp. 3019-3029, 2009.

[39] R. Aigner, H. Ngoc-Hoa, M. Handtmann, and S. Marksteiner, "Behavior of BAW devices at high power levels," in *Microwave Symposium Digest, 2005 IEEE MTT-S International*, 2005, pp. 12-17.

[40] M. Nitescu, F. Constantinescu, and A. G. Gheorghe, "An A.C. linear parametric behavioral model of a nonlinear BAW resonator," in *Circuits and Systems for Communications, 2008. ECCSC 2008. 4th European Conference on*, 2008, pp. 176-179.

[41] E. Rocas, C. Collado, J. Mateu, H. Campanella, and J. M. O'Callaghan, "Third order intermodulation distortion in Film Bulk Acoustic Resonators at resonance and antiresonance," in *Microwave Symposium Digest, 2008 IEEE MTT-S International*, 2008, pp. 1259-1262.

[42] C. Li, J. Briot, P. Girard, C. Ledesma, M. Solal, K. Cheema, D. Malocha, and P. Wahid, "Third order nonlinear distortion of SAW duplexers in UMTS system," in *Ultrasonics Symposium (IUS), 2010 IEEE*, 2010, pp. 283-286.

[43] M. Solal, L. Chen, J. Gratier, and S. Hester, "A nonlinear P matrix model to simulate intermodulation products in SAW devices " in *2012 IEEE Ultrasonics Symposium (IUS)*, 2012.

[44] S. Inoue, M. Hara, M. Iwaki, J. Tsutsumi, H. Nakamura, M. Ueda, Y. Satoh, and S. Mitobe, "A nonlinear elastic model for predicting triple beat in SAW duplexers," in *Ultrasonics Symposium (IUS), 2011 IEEE International*, 2011, pp. 1837-1841.

[45] *Advanced Design System* Available: http://www.home.agilent.com/en/pc-1297113/advanced-design-system-ads?&cc=US&lc=eng

[46] *Microwave Office*. Available: http://www.awrcorp.com/products/microwave-office

[47] S. Datta, *Surface acoustic wave devices*: Prentice-Hall, 1986.

[48] W. P. Mason, *Electromechanical transducers and wave filters*: D. Van Nostrand Co., 1948.

[49] *Guide to Harmonic Balance Simulation in ADS*: Agilent Technologies, 2004.

[50] *HFSS*. Available: http://www.ansys.com/